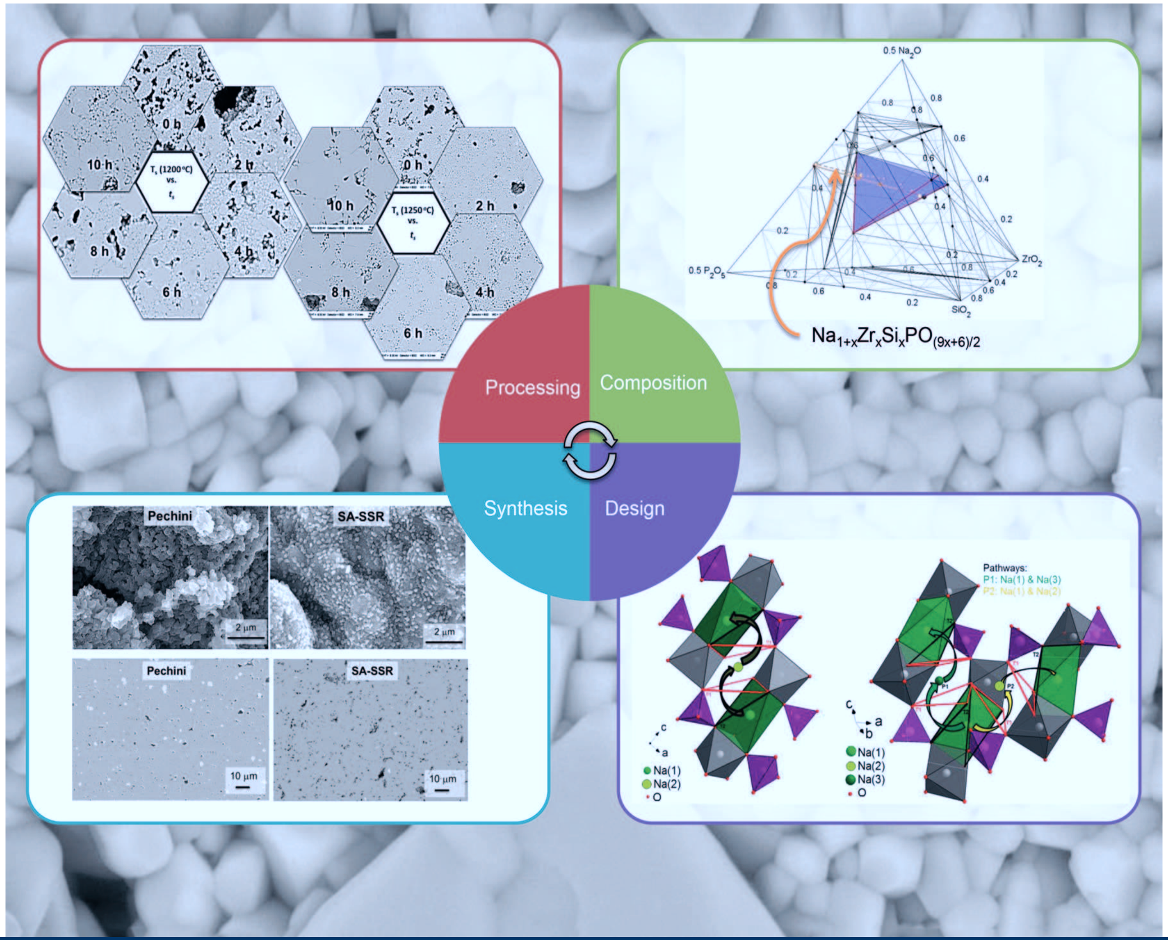

Sodium Ion Conducting Ceramics for Sodium Ion Batteries

Sahir Naqash

Energie & Umwelt / Energy & Environment
Band / Volume 451
ISBN 978-3-95806-382-2

Mitglied der Helmholtz-Gemeinschaft

JÜLICH
Forschungszentrum

Schriften des Forschungszentrums Jülich
Reihe Energie & Umwelt / Energy & Environment Band / Volume 451

Forschungszentrum Jülich GmbH
Institut für Energie- und Klimaforschung
Werkstoffsynthese und Herstellungsverfahren (IEK-1)

Sodium Ion Conducting Ceramics for Sodium Ion Batteries

Sahir Naqash

Schriften des Forschungszentrums Jülich
Reihe Energie & Umwelt / Energy & Environment Band / Volume 451

ISSN 1866-1793 ISBN 978-3-95806-382-2

Bibliografische Information der Deutschen Nationalbibliothek.
Die Deutsche Nationalbibliothek verzeichnet diese Publikation in der
Deutschen Nationalbibliografie; detaillierte Bibliografische Daten
sind im Internet über http://dnb.d-nb.de abrufbar.

Herausgeber und Vertrieb:	Forschungszentrum Jülich GmbH Zentralbibliothek, Verlag 52425 Jülich Tel.: +49 2461 61-5368 Fax: +49 2461 61-6103 zb-publikation@fz-juelich.de www.fz-juelich.de/zb
Umschlaggestaltung:	Grafische Medien, Forschungszentrum Jülich GmbH
Druck:	Grafische Medien, Forschungszentrum Jülich GmbH

Schriften des Forschungszentrums Jülich
Reihe Energie & Umwelt / Energy & Environment, Band / Volume 451

D 82 (Diss., RWTH Aachen University, 2018)

ISSN 1866-1793
ISBN 978-3-95806-382-2

Vollständig frei verfügbar über das Publikationsportal des Forschungszentrums Jülich (JuSER)
unter www.fz-juelich.de/zb/openaccess.

Abstract

The overwhelming demand of energy storage technologies has forced the scientific community to look beyond the commercially available options such as lithium ion batteries. As one of a potential alternative, sodium ion battery technology works in a similar way but provides the advantage of abundant and readily available raw materials at low cost. In addition, the lithium ion batteries, so far, are commercially available only with a liquid electrolyte. The electrolyte material in liquid state poses serious safety concerns, in case there is a leakage causing a short circuit and thermal runaway. Therefore an all-solid-state approach is one way to improve the safety issues of state-of-the-art batteries.

This work is performed to develop sodium ion-conducting ceramics that can be used in all-solid-state sodium ion batteries. Among several available options, the NASICON-type materials were selected because these types of materials are known to produce highly conductive ceramics and their conductivity in the best case has reached 4 mS cm^{-1}. Therefore, this work focuses on the materials and processing aspects of these sodium ion-conducting materials. It can be is divided into two sections: 1) synthesis & processing and 2) materials design and composition.

In the first part, main focus is on synthesis and processing of original NASICON material $Na_3Zr_2Si_2PO_{12}$. First, a solution-assisted solid state reaction synthesis route for producing $Na_3Zr_2Si_2PO_{12}$ is reported and compared with the so-called Pechini synthesis method. Secondly, $Na_3Zr_2Si_2PO_{12}$ is processed applying different sintering conditions to control its microstructure to better understand the microstructure-conductivity relationship of the material.

In the second part, the focus is on the materials design and composition by modifying the NASICON chemistry. This is achieved by substituting suitable cations into the NASICON structure. Furthermore, an attempt was made to reduce the processing temperature of NASICON materials by defining a series of compositions, so-called glass-NASICON composites, towards the low melting composition in the quaternary phase diagram of Na_2O–SiO_2–ZrO_2 and P_2O_5. The objective is to utilize the conduction properties of NASICON and low melting point of sodium-containing glasses to produce a material with sufficient Na^+ ion conductivity and reduced processing temperature (< 1000 °C). This would then be used as electrolyte material for fabricating an all-solid state Na^+ battery.

Kurzfassung

Der überwältigende Bedarf an Energiespeicher-Technologien zwingt die Wissenschaft dazu, andere Optionen als die kommerziell verfügbaren Lithium-Ionen Batterien zu erforschen. Eine vielversprechende Alternative stellt die Natrium-Ionen Technologie dar, welche auf einem ähnlichen Funktionsprinzip beruht, jedoch über ergiebigere und leicht verfügbare Rohstoffe zu günstigen Preisen verfügt. Außerdem sind Lithium-Ionen Batterien bislang nur mit flüssigem Elektrolyten kommerziell erhältlich. Dieser Flüssigelektrolyt stellt ein ernstzunehmendes Sicherheitsrisiko im Falle einer Leckage dar, bei der es zum Kurzschluss und einem Brand durch Überhitzung der Batterie kommen kann. Aus diesen Grund bietet ein Festkörperelektrolyt einen möglichen Ansatz, um die Sicherheitsanforderungen nach dem aktuellen Stand der Technik sicherzustellen.

Diese Arbeit wurde durchgeführt, um eine Natrium-ionenleitende Keramik zu entwickeln, die sich für den Einsatz in Na^+ Festkörperbatterien eignet. Unter verschiedenen anderen Optionen wurden NASICON-Materialien ausgewählt, da diese Keramiken dafür bekannt sind, dass sie im Idealfall hohe ionische Leitfähigkeiten von bis zu 4 $mS\,cm^{-1}$ zu erreichen. Daher konzentriert sich diese Arbeit auf die Werkstoff- und Herstellungseigenschaften dieser Materialien. Sie kann in zwei Abschnitte unterteilt werden: 1) Synthese und Herstellung und 2) Werkstoffentwicklung und Zusammensetzung.

Im ersten Teil liegt der Fokus auf der Synthese und Verarbeitung des reinen NASICON Materials mit der Zusammensetzung $Na_3Zr_2Si_2PO_{12}$. Zunächst wurde ein Syntheseansatz mit Hilfe einer lösungsunterstützten Festkörperreaktion durchgeführt und mit einem Ansatz nach der Pechini-Methode verglichen. Anschließend wurde das $Na_3Zr_2Si_2PO_{12}$ bei verschiedenen Sinterbedingungen prozessiert, um ein besseres Verständnis über die Zusammenhänge zwischen Mikrostruktur und Leitfähigkeit des Materials zu erlangen.

Der zweite Teil der Arbeit beschäftigt sich mit der Werkstoffentwicklung, wobei die chemische Zusammensetzung der NASICON-Materialien modifiziert wird. Dies wurde durch den Austausch geeigneter Kationen in der NASICON-Struktur erreicht. Weiterhin wurde ein Versuch unternommen, die Verarbeitungstemperatur der NASICON-Materialien zu reduzieren, indem eine Reihe von Zusammensetzungen definiert wurden – die sogenannten Glas-NASICON-Komposite – welche auf einen Bereich mit geringen Schmelzpunkten im quaternären Phasendiagramm Na_2O-SiO_2-ZrO_2-P_2O_5 ausgerichtet sind. Das Ziel ist, die Leitfähigkeit von NASICON zu erhalten und den geringen Schmelzpunkt von Na-haltigen Gläsern auszunutzen, um ein Material mit ausreichend hoher Na^+-Ionenleitfähigkeit und reduzierter Fertigungstemperatur (<1000 °C) zu erhalten. Dieses Material soll schließlich als Elektrolyt für die Herstellung einer Na^+ Festkörperbatterie Verwendung finden.

Table of Contents

List of Abbreviations

BSD	Back Scattering Detector
BSE	Back-Scattered Electrons
CTE	Coefficient of Thermal Expansion
DTA	Differential Thermal Analysis
DSC	Differential Scanning Calorimetry
EDX	Energy-dispersive X-ray spectroscopy
HSE	Hybrid Solid Electrolyte
ICP-OES	Inductively Coupled Plasma Optical Emission Spectrometry
MS	Mass Spectrometry
Na-S Battery	Sodium/Sulphur Battery
PCE	Plastic Crystal Electrolyte
SE	Secondary Electrons
SEM	Scanning Electron Microscopy
TG	Thermogravimetry
TOF	Time Of Flight
XRD	X-Ray Diffraction
ZEBRA Battery	Zero Emission Battery Research Activity
NAYZSP$_x$	$Na_{1+2x}Al_xY_xZr_{2-2x}(PO_4)_3$
NAYZSiP$_x$	$Na_{1+2x}Al_xY_xZr_{2-2x}(SiO_4)_2(PO_4)$
NZP	$NaZr_2(PO_4)_3$
NZSiP	$Na_3Zr_2(SiO_4)_2(PO_4)$
NZSiP$_x$	$Na_{3+x}Zr_2(SiO_4)_2(PO_4)$
PVdF-HFP	Poly(vinylidene fluoride-hexafluoropropylene
TEOS	Tetraethyl orthosilicate
NSSiP$_x$	$Na_{3+x}Sc_2Si_xP_{3-x}O_{12}$
NSZSiP$_x$	$Na_{3+x}Sc_xZr_{2-x}Si_2PO_{12}$
E_a	Activation Energy
$E_{a,\ Total}$, E_{gb}, $E_{a,\ bulk}$	Activation energy of total, gb and bulk conductivity respectively
R_{wp}	Weighing profile factor
σ_{Total}, σ_b, σ_{gb}	Total conductivity, bulk conductivity, grain boundary conductivity

Chapter 1: General background

It has been estimated that by 2050 the energy demands of ever-increasing global population will reach up to 28 TW, which is twice the energy demand today (14 TW). This equates to 130,000 TWh or equivalent to 10^{10} tons of burning oil yearly (Fig. 1.1) [1]. To meet such enormous energy demand, the corresponding energy production must be carried through sources that do not increase the CO_2 emission that rules out any reliance solely on fossil-fuels. These circumstances have made the development of alternative and advanced renewable energy technologies a global imperative.

There are several renewable energy sources, e.g. wind, solar, tidal, biomass and geothermal, but all these sources are nature-controlled and thus limited to geological locations and are inherently intermittent compared to the isolated large scale man-made facilities (e.g., dams, power plants etc.) that currently supply a vast majority of electrical energy. To make the best use of these energy sources, we need robust energy-storage systems that are versatile and durable. Unfortunately, to date only 1 % of the total energy consumed worldwide can be stored [1].

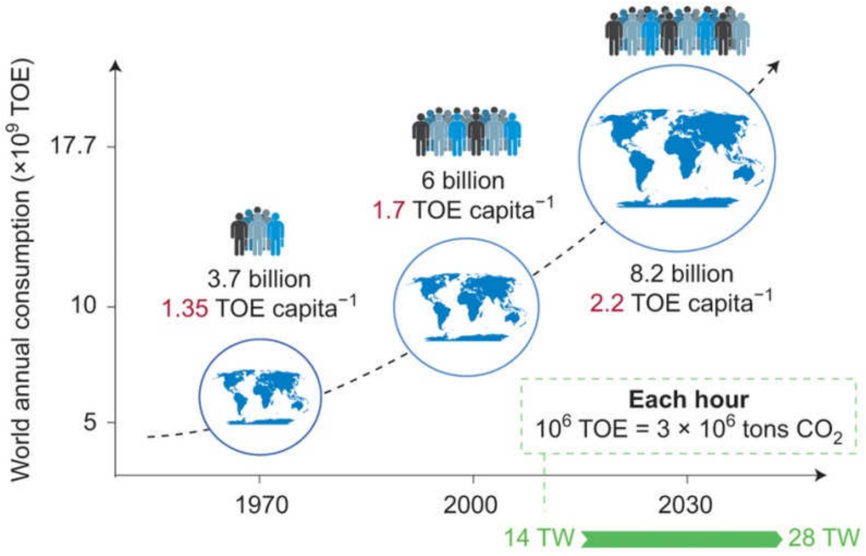

Fig. 1.1: Past, present and forecast of world's energy needs up to 2050. With the changing lifestyles of an increasing number of inhabitants, our energy rate demand will double from 14 TW (2010) to 28 TW (2050). TOE = ton of oil equivalent. Map: © Macmillan Mexico/Haide Ortiz Ortiz, Mario Enrique Ramírez Ruiz (Reprinted with permission) [1].

Batteries are the most attractive energy storage technology option available and have attracted the focus of scientific community in the past two decades. Unlike wind, solar, hydro etc. energy storage options battery is versatile, portable and capable of remote use. Despite its potential, the share of energy stored worldwide in batteries is only 0.02 % [1], however it is increasing with the increase usage of portable electronic devices and booming electrical vehicle industry.

Since the inception of battery technology, only few have achieved the relevant market share. Lead acid battery technology is the oldest one and still dominates the market share in terms of energy storage capacity. This system is more than 150 years old, cost-effective, and dominantly used in automotive applications (starting battery) and auxiliary power supply systems. The major drawback of lead acid batteries is its low energy density of 30 – 40 watts hours per kilogram (Wh kg^{-1}) and low energy conversion efficiency. Lately, several other systems were also introduced where electrode materials were substituted with metal hydroxides (Ni, Fe, Zn, Cd) but their application was hindered due to limited energy densities. Most preferable metal hydride battery is NiMH battery that has comparatively highest energy density of 100 Wh kg^{-1} [2].

Lithium-ion batteries (LIBs) offer the highest energy density of about 250 Wh kg^{-1} and these were first commercialized in early 1990s and since then their share in the market has been rapidly increasing. Due to high demand, the cost of such cells has reduced massively from 1000 € kWh^{-1} (in 1990s) to 200 € kWh^{-1} and is expected to reduce further in future [3, 4]. To date, LIBs available to consumers generates ~37% of the total revenue from batteries [1]. However, concerns have been raised regarding the environmental and economic sustainability of LIBs. Life cycle analysis (LCA) studies have revealed that, for storing 1 kW h of energy, LIB technology produces about 75 times more CO_2 as compared to coal energy, this accounts for whole life cycles from resource extraction over production, use phase until the end-of-life handling and recycling/deposition of waste [5]. The cost of energy stored in LIBs is several hundred times more than hydro-electricity, implying that battery processing and production is a big concern [6]. In addition, with increasing supply, the global resources of Li are continuously depleting and those which are currently available are located in sensitive geopolitical areas. Later concern has been minimized by a recent discovery of Li reserves of 1.3 million tons in Czech Republic [7]. Lastly, it has been proposed that in some years, the LIB technology will reach its maximum energy density value 300 W h kg^{-1}, therefore alternative cell chemistries will have to be invented in order to surpass this energy density [8].

These concerns about LIB technology make the exploration of the alternatives an imperative [9, 10]. The most appealing alternative in terms of economic and environmental sustainability is sodium. It is about 1000 times more abundant than lithium in the earth crust, and this does not include seawater sodium. High abundance leads to low material cost, for example the cost of Na_2CO_3 is 50 times lower than Li_2CO_3 and the gap is widening with time. In terms of performance, sodium is three times heavier than lithium (23 g mol^{-1} compared with 6.9 g mol^{-1}), and 0.3 V less electropositive, which means that gravimetric and volumetric penalties (~ 15 %) are unavoidable (Table 1.1). This elucidates why sodium batteries are anticipated for stationary applications. Nonetheless, if Na-ion technology is successful, early estimations forecast a cost reduction of 30 % as compared to Li-ion technology [1].

Table 1.1: The comparison of the main features of lithium and sodium metals [9].

Category	**Li**	**Na**
Atomic radius (Å)	1.52 Å	1.86 Å
Atomic weight	6.94 g mol^{-1}	22.99 g mol^{-1}
E^{o} (vs. Li/Li^{+})	- 3.00 V	- 2.70 V
Price (carbonates)	4.11 – 4.49 € kg^{-1} (Purity: battery grade 99.9 %)	0.07 – 0.37 € kg^{-1} (Purity: 98.8 – 99.2 %)
Capacity	3.83 Ah·g^{-1}	1.17 Ah·g^{-1}
Coordination preference	Octahedral & Tetrahedral	Octahedral & Prismatic
Melting point	180.50 °C	97.79 °C

Chapter 2: Introduction

A rechargeable Li^+ or Na^+ ion cell consists of two materials capable of Li^+/Na^+ ion insertion that are called positive (anode) and negative (cathode) electrodes. These electrodes are electronically separated by an electrolyte material (as a pure ionic conductor). The cell converts stored chemical energy into electrical energy and the performance of the whole assembly varies with varying the composition, shape, alignment, or state of these components.

A schematic representation of operating principle is shown in Fig. 2.1. Cell operates in two electrochemical modes; charging and discharging mode. During discharging, the anode is electrochemically oxidized causing a release of Li^+/Na^+ ions into the electrolyte. These ions subsequently migrate towards the cathode. During oxidation process, electrons travel through an electrical circuit from anode to cathode and combine with Na^+. These electrons complete an electrical circuit and this external flow of electrons can be utilized as energy source to drive appliances (discharging mode) as well as to charge battery (charging mode). Charging mode operates exactly opposite, and it is also possible that both charging and discharging processes occur simultaneously.

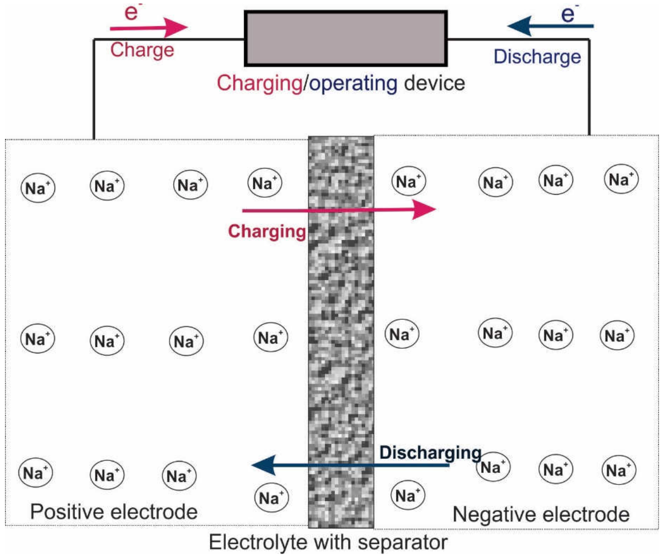

Fig. 2.1: Schematic illustration of Li^+/Na^+ ion battery operation.

The battery components require some specific characteristics due to the operation process. The electrodes (cathode and anode) should;

- be able to collect and release a large amount of Li^+/Na^+ ions in a large number of cycles,

- have ionic as well as electronic conductivity, and
- be chemically compatible with the electrolyte.

The electrolyte should:

- have high ionic and zero electronic conductivity to avoid short-circuiting of the electrons,
- have high thermodynamic stability in a wide temperature and voltage range, and
- have high physical and chemical compatibility with cathode and anode.

2.1. State-of-the art Na batteries

Even though work on lithium and sodium batteries started together, the progress in lithium battery has overwhelmingly left the sodium battery behind. In recent past, sodium batteries have again emerged by gaining attention. This can be clearly seen by noticing an exponential increase in the number of publications over the past few years in Fig. **2.2**.

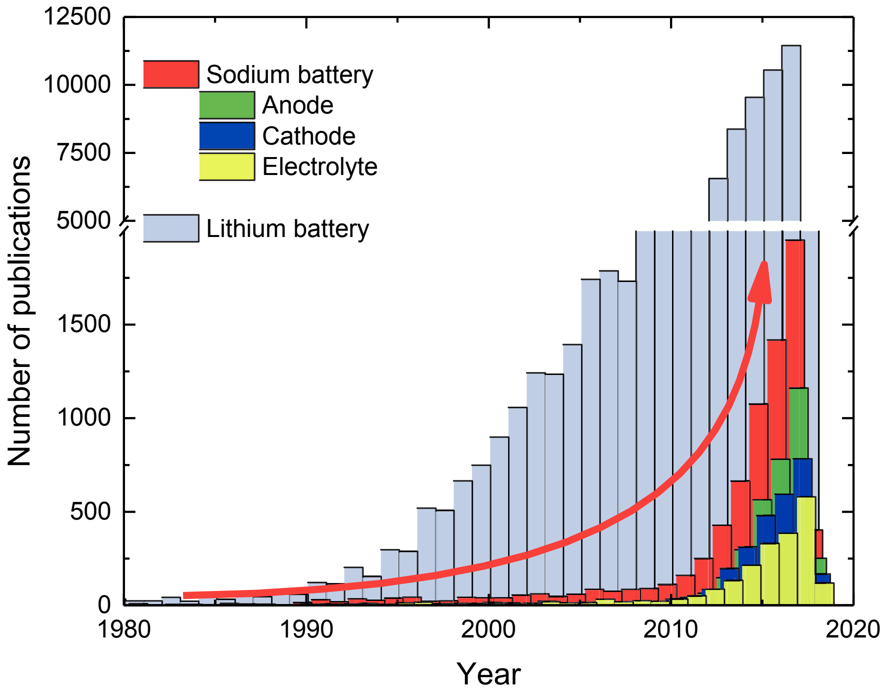

Fig. 2.2: Number of publications in the field of "Lithium battery" as compared to "Sodium battery" from 1970 to 2017. The keywords are given in legends. (Source: web of knowledge)

Sodium-sulphur (Na-S) [11] and Sodium-Nickel chloride (Na-$NiCl_2$) [12] are the only Na based batteries that are commercially manufactured by NGK Insulators and FZ Sonick respectively. Both are operated at high temperature ~300 ºC and contains β”-alumina as Na^+ ion conducting electrolyte.

In Na-S batteries, the anode material is molten Na which is filled in a tube of solid β”-alumina electrolyte. The tube is surrounded by cathode material which is molten sulphur in this case. During the cell discharge, Na^+ ions are transported through the β”-alumina electrolyte towards cathode where they react with sulphur to form polysulphides. Electrons are discharged as a consequence to an external circuit. Reversible reaction occurs during charging [13].

The molten electrodes are highly corrosive towards the cell container and sealant materials at the operating temperature (300 ºC) causing safety concerns. A lot of work has been devoted to reduce the operating temperature down to 100 ºC or to manufacture corrosion resistant container and sealant materials [10]. In case of leakage, the electrodes become in contact with each other leading to cell failure, which may be dangerous. It was reported in one incident on September 2011 when a NGK-manufactured Na-S batteries caught fire forcing the company to stop its manufacturing and asked customers not to use Na-S batteries [14].

The Na-$NiCl_2$ batteries [12] exhibit advantage over the Na-S because it does not contain highly corrosive molten sulphur cathode. It is replaced by a porous metal chloride usually $NiCl_2$ impregnated with a liquid electrolyte ($NaAlCl_4$) for better interfacial contact and less corrosion [15]. During the discharge, molten sodium is oxidized into Na^+ ions that are conducted through β”-alumina and $NaAlCl_4$ towards $NiCl_2$ (cathode) to form NaCl and Ni. Reversible reaction occurs during charging. These batteries are safer because in case of leakage, the molten Na reacts with the $NaAlCl_4$ to form NaCl and aluminum. These batteries can be assembled in a discharged state and it offers higher voltage than Na-S battery. In addition, it is also possible to further increase the battery power by incorporating iron in the anode [16-18].

In both cells, the elevated operating temperature is the biggest concern which is also linked to the safety of the batteries, particularly Na-S battery. In addition, it also escalates the operating cost therefore reduction of operating temperature has been the focus of the research, and so far, it has been reduced to 100 – 170 ºC by an American company Ceramatec [19].

In Na^+ ion battery technology, William Advanced Engineering offers a pack design of 3 Ah consisting of 48 cells. Their materials were purchased from Faradion Limited. The batteries are made of hard carbon anode and polyanion cathodes [20] separated by a liquid electrolyte. The corporate website claims that the cell performance is similar to the Li^+ ion batteries with the advantage of higher safety [21].

Na^+ ion solid state batteries are restricted to lab scale testing so far as reported by F. Lalère *et. al* [22]. This Na^+ battery was based on $Na_3V_2(PO_4)_3$ and $Na_3Zr_2Si_2PO_{12}$ as electrode and electrolyte materials, respectively. The conductivity of these materials at 200 ºC are $1.9 \cdot 10^{-4}$ S cm^{-1} and $1.5 \cdot 10^{-3}$ S cm^{-1}, respectively, and is the reason why its operating temperature is restricted to 200 ºC. The electrode material along with the electrolyte was spark plasma sintered (SPS) at 900 ºC to obtain a dense cell. The battery operated at 1.8 V with 85 % of theoretical capacity attained. Upon comparison, $Na_3V_2(PO_4)_3$ produced a better power density as compared to its lithium counterpart $Li_3V_2(PO4)_3$ at 80 ºC [23], but at higher temperature.

Table 2.1: Summary of the state-of-the art high temperature sodium batteries, the data is taken from [22, 24].

<table>
<tr><th>Battery</th><th>NaS</th><th>ZEBRA</th><th>All-solid-state Na battery</th></tr>
<tr><td>Manufacturer</td><td>NGK insulators/TEPCO</td><td>FZ Sonick</td><td>F. Lalère et al. (2014)</td></tr>
<tr><td>Cell configuration</td><td>Na|β"-alumina|S</td><td>Na|β"-alumina|MCl_2 (M = Fe, Ni)</td><td>$Na_3V_2(PO_4)_3|Na_3Zr_2Si_2PO_{12}|Na_3V_2(PO4)_3$</td></tr>
<tr><td>Open circuit voltage</td><td>2.08 – 1.78 V</td><td>2.58 V</td><td>1.7 V</td></tr>
<tr><td>Operating temperature</td><td>300-350 ºC</td><td>270-350 ºC</td><td>200 ºC</td></tr>
<tr><td>Theoretical capacity (per grams of +ve electrode)</td><td>377 mAh g^{-1}</td><td>305 mAh g^{-1}</td><td>5.1 mA h g^{-1} (cell level)</td></tr>
<tr><td>Energy density</td><td>760 (140-240) Wh·kg^{-1}</td><td>788 Wh·kg^{-1}</td><td>10.75 W h kg^{-1} (lab test)</td></tr>
<tr><td>Power density</td><td>90-245 W·kg^{-1}</td><td>130-160 W·kg^{-1}</td><td>4.23 W kg^{-1}</td></tr>
<tr><td>Life cycle</td><td>3500-5000 cycles
@ 80 % DoD</td><td>3500-5000 cycles
@ 80 % DoD</td><td>26 cycles
@ 75 % DoD (C/10)</td></tr>
<tr><td>Efficiency</td><td>80-90 %</td><td>80-90 %</td><td>5 - 10 %</td></tr>
<tr><td>Application</td><td>Stationary energy storage</td><td>Battery electric vehicles Stationary energy storage</td><td>Still Lab based experiments</td></tr>
<tr><td rowspan="2">Advantages</td><td>High power
High energy density
High efficiency of charge/discharge
Temperature stability</td><td>High voltage
Better tolerance against overcharging, safe
Easy assembly
Safe</td><td>All NASICON
Safe</td></tr>
<tr><td colspan="3">Low cost of raw materials</td></tr>
<tr><td rowspan="5">Shortcomings</td><td>Unsafe → fracture of beta-alumina
Expensive processing</td><td>Preheating to operating temperature</td><td>Expensive processing
(i.e., spark plasma sintering)</td></tr>
<tr><td>Violent reaction</td><td></td><td></td></tr>
<tr><td colspan="3">High operating temperature</td></tr>
<tr><td colspan="2">Molten sodium electrode</td><td rowspan="2">Still lab based prototype</td></tr>
<tr><td colspan="2">Off use: consumes 10-14 % of its own capacity per day to maintain temperature</td></tr>
<tr><td rowspan="2">Environmental Impact</td><td>Only Na hazardous material</td><td>Recovery of Ni</td><td>Na based materials</td></tr>
<tr><td colspan="2">No emission during operation</td><td>No Emission</td></tr>
</table>

2.2. Na^+ ion conducting materials

Several types of materials have been reported as Na^+ ion conductors, such as beta-alumina, **s**odium **s**uper **i**on **con**ductors (NASICON: $Na_3Zr_2Si_2PO_{12}$), glass and glass-ceramic electrolytes and polymer electrolytes [24, 25]. Fig. 2.3 compares the conductivity of some attractive inorganic Na-ion conducting materials as a function of temperature [26-32]. The details on each material-type are further discussed in coming subsections.

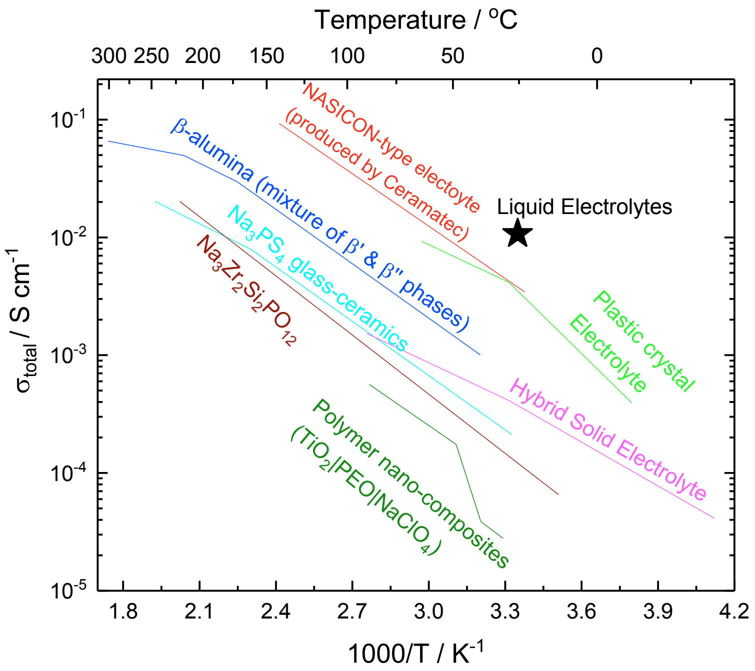

Fig. 2.3: Arrhenius plot of the total conductivity of sintered polycrystalline β"-alumina [28], sintered polycrystalline NASICON material from the company Ceramatec [33], sintered polycrystalline NASICON [34], Na_3PS_4 glass-ceramic [35], polymer nano-composite electrolyte [36], plastic crystal electrolytes [37] and NASICON-based hybrid solid electrolyte [38].

2.2.1. Beta-alumina

The beta-alumina solid electrolyte (BASE) is the only fast ion conductor used as electrolyte material in both Na-S and Na-$NiCl_2$ batteries. It exists in two distinct crystal structures: β-alumina with hexagonal structure ($P6_3/mmc$: a_o = 0.557, c_o = 2.261 mm) and β”-alumina with a rhombohedral structure ($R3m$: a_o = 0.560, c_o = 3.395 mm). They differ in chemical stoichiometry and stacking sequence of oxygen ions across the conduction layer [39]. Among them, β”-alumina has higher Na^+ ion conductivity as compared to β-alumina. The conductivity of single crystals of β”-alumina in the plane direction is as high as 0.1 S cm^{-1} at 25 °C and increases up to 1 S cm^{-1} at 300 °C [40], which is five times more than that of polycrystalline β”-alumina. The typical ionic conductivity of a polycrystalline β”-alumina at 300 °C is 0.22 – 0.35 S cm^{-1} [41].

Stoichiometric β-alumina has a formula $(Na_2O)_{1+x}Al_2O_3$ where $x = 0$, however it is unanimously agreed that it is never prepared with accurate stoichiometry [42]. The x can be as high as 0.57 for β-alumina. The depletion of aluminum or enrichment of sodium in β-alumina leads to higher Na^+ ion conductivity as compared to stoichiometric β-alumina. β"-alumina is prepared to further improve the Na^+ conductivity by substituting aluminum ions with mono- or divalent ions e.g., Li^+, Mg^{+2} [42, 43]. The substitution allows departure from the β-alumina stoichiometry, resulting in a higher sodium content and conductive β”-alumina. The monovalent Li^+ and divalent Mg^{+2} also helps to stabilize the structure that tends to decompose at temperatures > 1600 °C. The two ideal β”-alumina stoichiometries are $Na_{1.67}Al_{10.33}Mg_{0.67}O_{17}$ and $Na_{1.67}Al_{10.67}Li_{0.33}O_{17}$ [42].

β”-alumina can be synthesized through various synthesis methods such as, solid state reaction [44-47], sol-gel technique [48-55], co-precipitation [56, 57], spray-freeze-drying method [54], flame spray pyrolysis [58] and mechanical method [59]. β”-alumina has also been synthesized through microwave heating of solution-derived precipitates [60].

Table 2.2: The composition, conductivities and synthesis techniques of single and polycrystalline β and β-alumina.

Name	**Conductivity (S cm^{-1})**			**Ref.**
	25 °C	**300 °C**	**E_a (eV)**	
Single crystal β-alumina	0.036			[61]
	0.024		0.16	[62]
	0.035		0.13	[28]
	0.03	0.21	0.16	[63]
	0.014		0.16	[64]
	0.03		0.17	[43]
	0.025		0.15	[40]
	0.03	0.27	0.14	[65]
Polycrystalline β- Al_2O_3	0.0012	0.065	0.27 (25 – 200 °C) 0.15 (>200 °C)	[28]
Single crystal β”-alumina	0.04		0.22 (25 – 250 °C) 0.17 (200 - 650 °C)	[43]
	0.1		0.20 (-80 ~ 150 °C) 0.12 (150 - 500 °C)	[40]
	0.014	1	0.31 (-80 – 150 °C) 0.09 (150 - 650 °C)	[40]
			0.33 (25 – 150 °C) -0.1 (> 150 °C)	[66]
	0.01	1	(<200 °C)	[67]
Polycrystalline β”-alumina		0.22-0.35	0.15-0.26	[41]
		0.21	0.24 (285 – 330 °C) 0.22 (330 – 375 °C)	[44]
		0.36	0.18 (285 – 330 °C) 0.16 (330 – 375 °C)	[44]
		0.2		[68]

Despite better ionic conductivity of β”-alumina, its application in modern battery systems is restricted due to its challenging processing conditions. β”-alumina powders prepared by different methods produces different electrical properties, as listed in Table **2.2**. It is challenging to obtain pure obtained pure β”-alumina through conventional solid state reaction and solution-based chemical because the synthesized β”-alumina is often epitaxial mixed with β-alumina and form $NaAlO_2$ along the grain boundaries. This not only changes its composition but also reduces the conductivity due to presence of low conductivity β-alumina. Its further processing involves multiple ball milling and calcination steps before it can be sintering at 1600-1700 °C to achieve high density. The high sintering temperature is not only expensive but it also affects the microstructure because at such high temperatures sodium oxide is evaporating, and there if further demands careful and costly experimental setup (e.g., encapsulation in Pt or magnesia or using vapor phase reaction) [69, 70]. In addition, when used as thin layers in Na-S battery operating at elevated temperatures, their mechanical strength also becomes crucial to avoid potential accidents due to electrolyte cracks. Despite the fact that mechanical strength can be enhanced by 50 percent by adding ZrO_2 [71-74], its complicated and expensive processing parameters restricts is use in modern applications and make pursuit of alternative Na^+ ion conducting materials that exhibit better mechanical stability and conductivity at reduced temperatures [75].

2.2.2. Polymeric and hybrid solid electrolytes

Several strategies have been used to implement low cost polymers as electrolyte materials in sodium batteries. These include polyethylene oxide (PEO) [76] or polyvinyl alcohol (PVA) [77] immersed in plasticizer with high dielectric constant or solvents (or its solution) with different salts. The solvent or salt solution is retained in the mechanically stable polymeric matrix and improves its ionic conductivity.

Another interesting strategy has recently been used where a hybrid electrolyte was prepared from polymeric binders, e.g. ethylene carbonate (EC), polypropylene carbonate (PC) mixed with ceramic powder capable of sodium conduction to form a flexible solid body. This already conductive sheet is then immersed in liquid sodium electrolyte to further enhance the conductivity. For example, a hybrid solid electrolyte (HSE) with 75 wt. % NZSiP ceramic powder and 15 wt. % PVdF-HFP polymer and ether-based liquid electrolyte, respectively. This HSE has a high ionic conductivity of 0.36 mS cm^{-1} at room temperature as well as high thermal stability against shrinkage [78]. The conductivity of dry NASICON/polymer composite is only $1.1 \cdot 10^{-8}$ S cm^{-1}, therefore immersion in liquid based electrolyte is essential to obtain high conductive hybrid electrolyte. Even though HSEs are safer as compared to liquid electrolyte, the presence of even small amount of liquid electrolyte is still a safety concern.

2.2.3. Glass and glass-ceramics

Glass and glass-ceramic materials have also shown sodium conduction properties [79-82]. Conventionally, glasses are made by heating raw materials above the melting point followed by rapid cooling below their glass transition temperature (T_g), this method is also referred as melt quenching [83]. Alternatively, glasses can also be prepared through vigorous mechanical deformation of crystalline materials [84] or mechano-chemical synthesis methods [85]. Several glasses with NASICON composition have been reported with formula $Na_xB_y(PO_4)_3$, as reported by [75, 83]. Best conductivity values are obtained for glasses with small amount of crystalline phase i.e., glass-ceramic with cubic Na_3PS_4 is ~ 0.2 mS cm^{-1}, but which is lower than NASICONs [85]. The Na_3PS_4 glass-ceramics are also used as electrolyte material to measure the charge-discharge curves of an all-solid-state rechargeable cell yielding a current density 0.013 mAcm^{-2} at room temperature [85]. Several glass and glass-ceramics, their composition and their respective conductivities are listed in the Table 2.3.

Table 2.3: Classification, composition, synthesis techniques and conductivity (at room and elevated temperature) of selected glass and glass ceramic compositions.

Name	**Composition**	**Conductivity [S cm^{-1}]**		**Ref.**
		25 °C	**Elevated T [°C]**	
Alkali-sulfide: glass & glass ceramics	Na_3PS_4	$6 \cdot 10^{-4}$		[85]
	Na_3PS_4 + Tetragonal Na_3PS_4	$1 \cdot 10^{-6}$	-	
	Na_3PS_4 + Cubic Na_3PS_4	$2 \cdot 10^{-4}$	-	
	Na_2S-GeS_2	$\sim 10^{-5}$	-	
	Na_2S-SiS_2	$\sim 10^{-4}$	-	
	$xNa_2S+(1-x)P_2S_5$	$3.2 \cdot 10^{-4}$	-	
Phosphate glasses (Nasiglas)	$Na_3Ga_2P_3O_{12}$ [83]	$10^{-9} – 10^{-7}$	$4.1 \cdot 10^{-9}$ (65 °C)	[83]
	$Na_5GeP_3O_{12}$[83]		$8.0 \cdot 10^{-9}$ (165 °C)	
	$Na_5TiP_3O_{12}$[83]		$5.35 \cdot 10^{-5}$ (165 °C)	

2.2.4. Na$^+$ Super Ionic Conductors (NASICONs)

NASICON (Na$^+$ Super Ionic Conductor) is a broad class of materials firstly reported in 1976 by Hong and Goodenough [86, 87]. The original NASICONs were solid solutions derived from $NaZr_2(PO_4)_3$ by partial substitution of P by Si balanced by Na in order to maintain charge neutrality, yielding the general formula $Na_{1+x}Zr_2Si_xP_{3-x}O_{12}$ ($0 \leq x \leq 3$). The crystal structure of firstly reported $Na_{1+x}Zr_2Si_xP_{3-x}O_{12}$ ($0 \leq x \leq 3$) is rhombohedral ($R\bar{3}c$), except for $1.8 \leq x \leq 2.2$ which undergoes monoclinic distortion (C2/c). The crystal structure can also be monoclinic for $LiZr_2(PO_4)_3$ [88, 89] or triclinic for $LiSn_2(PO_4)_3$ [90].

NASICON structure is not only confined to sodium, it is rather a huge family of materials having a particular structure. The general formula of NASICON type structure is $AM(PO_4)_3$ [75], where A-sites are charge carriers and M sites belong to central transition metal cations. A-site can be occupied by

- monovalent cations: Li^+, Na^+, K^+, Rb^+, Cs^+, H^+, H_3O^+, NH_4^+, Cu^+, Ag^+,
- divalent cations: Mg^{2+}, Ca^{2+}, Sr^{2+}, Ba^{2+}, Cu^{2+}, Pb^{2+}, Cd^{2+}, Mn^{2+}, Co^{2+}, Ni^{2+}, Zn^{2+},
- trivalent cations: Al^{3+}, Y^{3+}, La^{3+}, Lu^{3+}
- tetravalent cations: Zr^{4+}, Hf^{4+}, Ge^{4+}

The A-site can also be vacant if the M site is occupied by a pentavalent cation. The M sites can either be

- divalent cations: Cd^{2+}, Ni^{2+}, Mn^{2+}, Co^{2+}, Zn^{2+}, Mn^{2+},
- trivalent cations: Fe^{3+}, Sc^{3+}, Ti^{3+}, V^{3+}, Cr^{3+}, Al^{3+}, ln^{3+}, Ga^{3+}, Y^{3+}, Lu^{3+}
- tetravalent cations: Ti^{4+}, Zr^{4+}, Hf^{4+}, Sn^{4+}, Si^{4+}, Ge^{4+},
- pentavalent cations: V^{5+}, Nb^{5+}, Ta^{5+}, Sb^{5+}, As^{5+}

In some cases, the M site can be occupied by more than one cations, leading to the general formula $AM^1M^2(PO_3)_{12}$. With a general formula $AM^1M^2(PO_4)_3$, the crystal structure is stable for a wide range of substitutions; from a basic $NaZr_2(PO_4)_3$ (NZP) developed by [86, 87] to complex $Na_{1+2w+x-y+z}\,M^{+2}{}_w\,M^{+3}{}_x\,M^{+5}{}_y\,M^{+4}{}_{z-w-x-y}\,(SiO_4)_z\,(PO_4)_{3-z}$ systems reviewed by [91].

In sodium conductors, only sodium A-sited compositions are of interest. NASICON-type Na^+ conducting materials have better stability as compared to the β-alumina [92] and the highest room temperature conductivity achieved for these materials is in the order of 10^{-3} S cm^{-1} [93] which is similar to commercially produced β-alumina by Ionotec [94]. These type of materials have been synthesized through a range of synthesis methods such as, solid state reaction [95-97], sol-gel technique [98, 99], pechini method [100, 101], co-precipitation [95, 102], wet-chemical synthesis [103] and mechanical method [104]. Their processing involves free sintering of a pressed body in air as well as some unconventional routes such as microwave heating [105] and spark plasma sintering [106].

Table 2.4 represents the conductivities of well-known NASICON compositions. The NASICON compound produced by Ceramatec has been proposed for its use as a solid electrolyte in solid-state electrochemical devices such as Na-S batteries [107], gas sensor devices [108-110] and ion sensors [111].

Table 2.4: The composition, synthesis techniques and the conductivity of some NASICON materials

Composition	**Conductivity [S cm^{-1}]**		**Ref.**
	RT	**300 °C**	
$NaZr_2(PO4)_3$	$4.5 \cdot 10^{-6}$	$4.89 \cdot 10^{-5}$	[86, 112, 113]
$NaGe_2(PO_4)_3$	$1.1 \cdot 10^{-12}$	$2.56 \cdot 10^{-6}$	[114]
$NaTi_2(PO_4)_3$	$4.4 \cdot 10^{-10}$	$2.98 \cdot 10^{-5}$	[112, 114, 115]
$NaHf_2(PO_4)_3$	$8.8 \cdot 10^{-10}$	$1.03 \cdot 10^{-4}$	[115-117]
$NaSn_2(PO_4)_3$	$4.7 \cdot 10^{-9}$	$1.50 \cdot 10^{-5}$	[113, 118]

2.2.5. Structure

NASICONs consist of a three-dimensional framework of corner-shared ZrO_6 octahedra and (Si, P)O_4 tetrahedra, containing interconnected channels in which Na^+ are encapsulated at A-sites (Fig. 2.4a). Interstitial spaces of these channels provide a conduction pathway for the

Na^+ between two positions Na(1) and Na(2) (Fig. 2.4). Na(1) positions are six-fold coordinated to oxygen ions of three (Si, P)O_4 tetrahedra above and below (coordinate (0, 0, 0)). Na(2) positions are also sixfold coordinated to oxygen ions of three coplanar (Si, P)O_4 tetrahedra (coordinate (x, y, 0.25)). This site occupancy was also confirmed for its lithium counterpart $Li_{1+x}Al_xTi_{2-x}P_3O_{12}$ [119]. In case of the monoclinic distortion, another position is generated, Na(3) which is threefold coordinated to oxygen ions of three ZrO_6 octahedra and conduction occurs by jumping from Na(1) to the Na(2) or Na(3) sites.

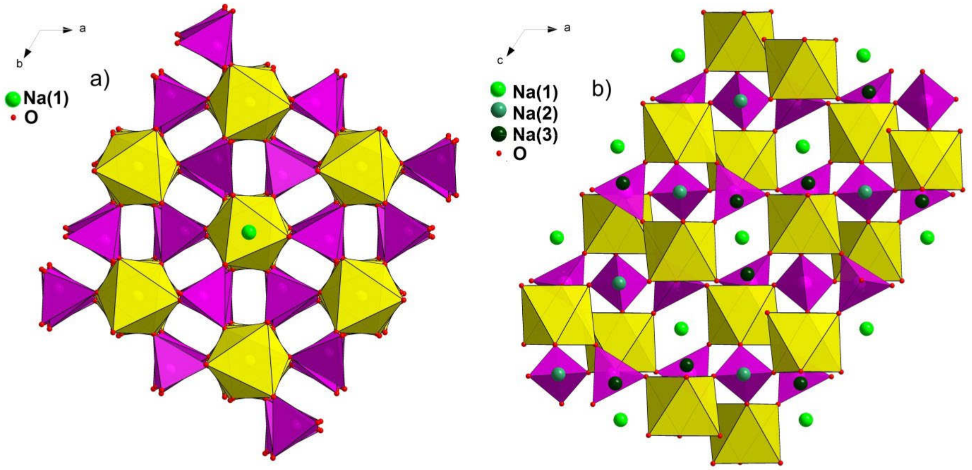

Fig. 2.4: Two dimensional a-b projection of (a) rhombohedral R$\bar{3}$c type NZP and (b) monoclinic C2/c type NZSiP illustrating Na(1), Na(2) and Na(3) sites, respectively. The yellow octahedra and pink tetrahedra are representing ZrO_6 and PO_4, respectively. The crystallographic data were taken from [120].

2.2.6. Conduction pathways

Conduction of Na^+ ion takes place by its consecutive jumps among sodium positions; Na(1) to Na(2) or Na(3) sites, as shown in Fig. 2.5. The length of jump is approximately 3 Å and depends on the composition of material [91]. Movement of Na^+ between two sodium positions occurs through oxygen triangles T1 and T2 (Fig. 2.5) and the size of these triangles determines the ease of Na^+ ion transport. In Fig. 2.5, the passage of Na^+ through T1 (smaller triangle) is more difficult as compared to T2 (bigger triangle).

The increase of the area of T1 in composition NZP where Area T1 = 4.968 Å^2, E_a = 0.47 & $\sigma_{300\,^oC}$ = 4.89 x 10^{-5} S cm^{-1}) by partial substitution of P with Si in NZSiP shows a remarkable increase in conductivity where area T1= 5.223 Å^2, Ea = 0.33 & $\sigma_{300\,^oC}$ = 0.2 S cm^{-1} [121]. It is further confirmed for several NASICON compositions through a correlative study of area of

T1 and activation energy for ionic conductivity by [91]. Therefore, size variation of T1 and T2 hindering ionic movement is referred as the bottleneck for sodium conduction in the system.

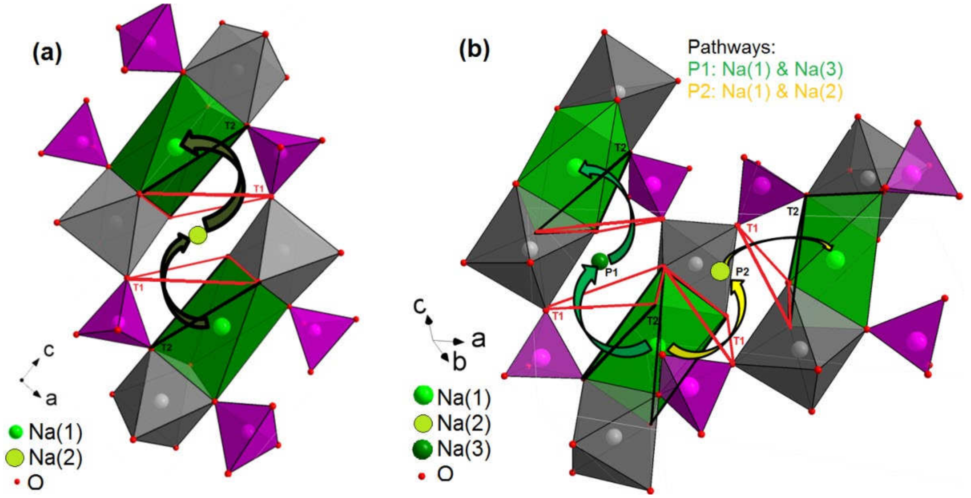

Fig. 2.5: Schematic representation of triangles T1 (red) and T2 (black) along a-c plane, and conduction of sodium (a) between Na(1) and Na(2) in NZP, (b) two pathways P1 and P2 between Na(1) and Na(2) & Na(3) in NZSiP, respectively. The pink tetrahedra, green octahedra and grey octahedra represent PO_4, NaO_6 and ZrO_6 respectively. Crystallographic data taken from [120].

2.2.7. Material design and selection

Several parameters can be considered while selecting a NASICON composition in order to obtain high conductivity. These parameters are shortlisted by a structure-composition-property correlation of more than 150 NASICON compositions by Guin and Tietz [91]. A strong influence of these parameters on the conductivity has been found. These parameters are

(i) Size of metal cations,

The size of transition metal cations is defined in terms of an effective mean radii i.e. $r_{eff} = r_{M^{+2}} \; w + r_{M^{+3}} \; x + r_{M^{+5}} \; y + r_{M^{+4}} \; (2 \quad w \quad y)/2$. When r_{eff} of the materials is close to 0.72 Å, their conductivity is among the highest known.

(ii) Na content in the formula unit

Conductivity is also influenced by the concentration of charge carriers (i.e. Na^+ ions). However after a certain Na^+ ion concentration is reached to a point where the ratio of charge carriers and vacancies is optimal, any further increasing Na content in the formula unit blocks/hinders Na mobility. In general, compositions with ≥2.5 mol sodium per formula unit show a high ionic conductivity between $2 \cdot 10^{-5}$ and $2 \cdot 10^{-3}$ S cm^{-1} [91].

(iii) Crystal structure distortions

As already discussed in section 2.2.6, crystal structures significantly changes the area of T1, which has a direct effect on the movement of Na in the lattice. NASICON compositions with monoclinic distortion have larger T1 and therefore higher conductivity. Monoclinic distortion can be induced by partial substation of P with Si [121]. The crystallographic distortion not only enlarges T1, but also creates additional Na sites which are also a reason for higher conductivity.

A quantified investigation of the effect caused by these parameters has not been established yet, however it is agreed that they have a synergic impact on the performance of NASICON materials. To establish a quantified connection of each parameter, more data are required from materials fulfilling aforementioned guidelines.

In one of our studies (section 5.1), we have attempted to design a material based on the guidelines given in [91] to validate the hypothesis that if r_{eff} is close to 0.72 Å, the material will show optimal structural and electrochemical properties. In this framework, a novel $Na_{1+2x}Al_xY_xZr_{2-2x}(PO_4)_3$ solid solution, where Zr^{+4} (r = 0.72) is substituted with equimolar amounts of Al^{+3} (r = 0.53) and Y^{+3} (r = 0.90) are prepared. In this system, the r_{eff} of the system lies within 0.720-0.718 Å. Validation will be based on the structural and electrochemical properties in comparison to the data in [91].

2.3. Scope of this thesis

The thesis, as clear from the title “sodium conducting ceramics for sodium ion batteries” focuses on the materials and processing aspects of the sodium-conducting materials, especially NASICON ceramics. A schematic illustration of the work is shown in Fig. 2.6

where the work is divided into two sections: 1) synthesis & processing and 2) design and composition.

In the first part, main focus is on synthesis and processing of original NASICON material $Na_3Zr_2Si_2PO_{12}$. First, a unique solution-assisted solid state reaction synthesis route for producing NZSiP is reported and compared with Pechini synthesis method [122]. Secondly, NZSiP is processed applying different sintering conditions to control its microstructure to better understand the microstructure-conductivity relationship of the material.

In the second part, the focus is on the design and composition by modifying the NASICON chemistry. This is achieved by substituting suitable cations into the NASICON based on [91]. Furthermore, an attempt was made to reduce the processing temperature of NASICON materials by defining a series of compositions, so called glass-NASICON composites, towards the low melting composition in the quaternary phase diagram of Na_2O–SiO_2–ZrO_2 and P_2O_5. The objective is to utilize the conduction properties of NASICON and low melting point of sodium-containing glasses to produce a material with sufficient Na^+ ion conductivity and reduced processing temperature (< 1000 °C). This would then be used as electrolyte material for fabricating an all-solid state Na^+ battery.

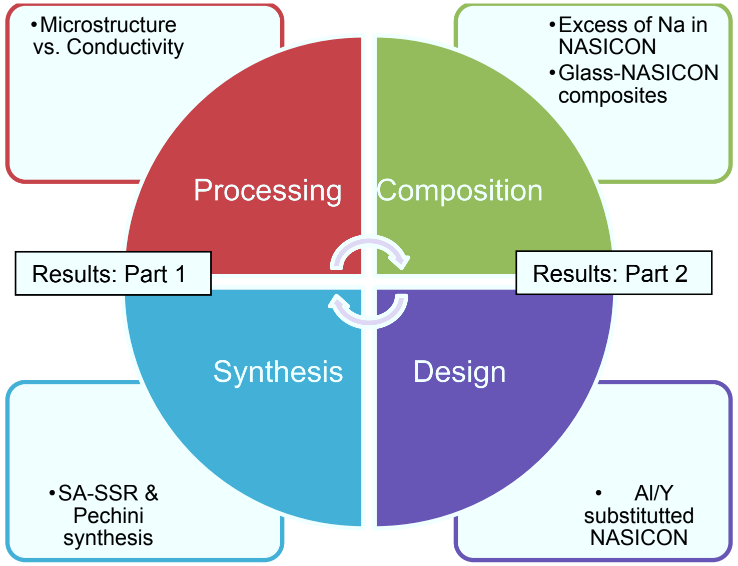

Fig. 2.6: Schematic of the scope of this thesis covering a range of studies related to NASICON materials.

Chapter 3: Experiments and Methods

Several experimental techniques and methods were used to characterize and analyze the samples. These methods are descripted in this section.

3.1. Synthesis methods

Synthesis plays a lead role in determining the quality of powder precursor that eventually determines its further processability. In this thesis, two different synthesis methods were used to synthesize the materials. They are briefly described below, and later compared in detail in section 4.1.

3.1.1. Solution Assisted Solid State Reaction (SA-SSR)

In SA-SSR method, $Na_3Zr_2(SiO_4)_2(PO_4)$ was prepared by mixing stoichiometric amounts of $NaNO_3$ (99.5 %), $ZrO(NO_3)_2$ (99 %) and $Si(OC_2H_5)_4$ (99 %), supplied from VWR International, Belgium, in a quartz glass container. After the nitrates were dissolved in distilled water, a stoichiometric amount of tetraethyl orthosilicate, $Si(OC_2H_5)_4$, was added. When the $Si(OC_2H_5)_4$ was hydrolyzed, a corresponding amount of $NH_4H_2PO_4$ was added and stirred for 30 minutes to form a homogeneous precipitation. The mixture was stirred overnight with 300 rpm at 50 °C. The homogenized mixture was firstly heated from 50 up to 100 °C to slowly evaporate the water. Subsequently, the product was fired in a furnace at 600 °C for 3 h to form an amorphous raw powder. During this heat treatment, the precipitate was pyrolyzed and NO_x, CO_2, H_2O evolved as gaseous products. Further calcination (800 °C, 12 h) and sintering (1250 °C) in Pt crucibles of the raw powder resulted in the desired ceramic.

3.1.2. Pechini synthesis

In Pechini method, named after an Italian scientist M. P. Pechini [122], the stoichiometric amounts of metal nitrates, e.g. $NaNO_3$ (99.5 %), $Al(NO_3)_2 \cdot 9\ H_2O$ (99.2 %), $Y(NO_3)_2 \cdot 6\ H_2O$ (99.8 %), $ZrO(NO_3)_2 \cdot x\ H_2O$ (99 %), and $Si(OC_2H_5)_4$ (99 %), supplied by VWR International (Belgium), were mixed and dissolved in a quartz glass container, followed by the addition of citric acid ($C_6H_8O_7$) twice the molar amount of metal cations (Na^+, Al^{3+}, Y^{3+}, Zr^{4+}, NH_4^+) to form citrate complexes. After formation of a clear solution, a stoichiometric amount of $NH_4H_2PO_4$ was added and stirred for 0.5 h to form an homogeneous precipitation. Ethylene glycol was then introduced in the same molar amount as citric acid. The mixture was stirred overnight at 300 rpm and 50 °C. Citric acid acts as a complexing agent and ethylene glycol acts as a polymerizing agent. The formation of citrate complexes results in a better distribution of ions and prevents the separation of components in later processes. With the presence of ethylene glycol, esterification results in the formation of a gel. The homogenized mixture was first heated from 50 °C up to 100 °C to slowly evaporate H_2O. Further heating of up to 300 °C leads to the polycondensation of ethylene glycol and citric acid, and results in the formation of a highly viscous polymer gel. The stirring bar should be taken out before the viscosity increases. Subsequently, the gel was fired in a furnace at 600 °C for 3 h to form an amorphous precursor. During this heat treatment, the polymer matrix was pyrolyzed and NO_x, CO_2, and H_2O evolved as gaseous products. Further calcination (800 °C, 12 h) of the precursor and sintering in Pt crucibles resulted in the desired crystalline phase.

3.2. Crystal structure

3.2.1. X-ray diffraction

X-ray diffraction (XRD) is a rapid and non-destructive analytical technique used for phase identification of crystalline materials and can also provide further information on the crystallographic properties of the material. The X-rays are targeted on the sample surface where they are scattered by the ordered facets of a crystalline material, and those undergoing constructive interference are recorded by a detector, as shown in Fig. 3.1a. The criterion for constructive interference is given by Bragg's law (Fig. 3.1b) [123].

$$n\lambda = 2d_{hkl}\sin(\theta) \qquad \text{Eq. 1}$$

where n is an integer, θ the angle of incidence with the lattice plane and d_{hkl} the distance between lattice planes. Any set of lattice planes can be indexed by hkl, the so-called Miller indices, which represent the points of intersections of the plane with the unit cell edges.

The whole sample surface is scanned when $2\theta = 180^0$, and the points where the scattered waves interfere constructively Bragg's law is applicable. A diffraction pattern is obtained by measuring the intensity of scattered waves (reflections) as a function of scattering angle (using a movable detector, Fig. 3.1a). Very strong intensities known as Bragg peaks are obtained in the diffraction pattern when the lattice is highly ordered [123].

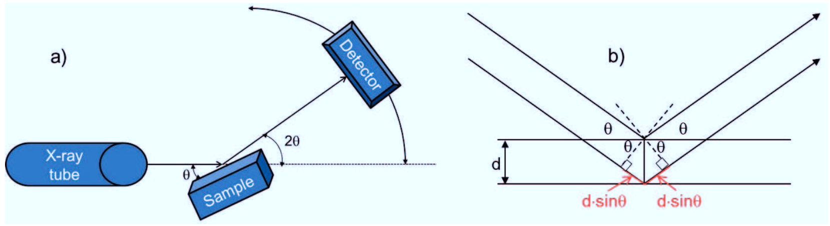

Fig. 3.1: Schematic of (a) X-ray diffractometer and (b) Braggs diffraction law [124].

The unit cell information for a given lattice is obtained using the following relationship [125]:

$$\frac{1}{{d_{hkl}}^2} = \left(\frac{h}{a} + \frac{k}{b} + \frac{l}{c}\right)^2 \qquad \text{Eq. 2}$$

for a cell any crystalline material, however it is reduced to

$$\frac{1}{{d_{hkl}}^2} = \frac{4}{3a^2} \times (h^2 + k^2 + l^2) + \frac{l^2}{c^2} \qquad \text{Eq. 3}$$

for a rhombohedral unit cell where $a = b \neq c$ and $\alpha = \beta = 90\,°$ and $\gamma = 120\,°$

$$\frac{1}{{d_{hkl}}^2} = \frac{h^2}{a^2 sin^2\beta} + \frac{k^2}{b^2} + \frac{l^2}{c^2 sin^2\beta} - \frac{2hlcos\beta}{ac\ sin^2\beta} \times (1 - cos^2\beta)^{-1} \qquad \text{Eq. 4}$$

for a monoclinic unit cell where $a \neq b \neq c$ and $\alpha = \gamma = 90\,° \neq \beta$

The space group and lattice parameters can be calculated using Eq. 3 and Eq. 4 for rhombohedral and monoclinic structure respectively from given set of d-values. Despite the fact that these calculations are simple for one reflection at a certain d-value, the calculation of a complete XRD pattern for polycrystalline material is rather complex and complicated. This is due to the fact that XRD pattern of a polycrystalline material is influenced by parameters such as preferred orientation of crystallographic planes or the overlapping of reflections (e.g., from different structures of one or more phases). Therefore, complex algorithms are necessary to derive the correct space group and unit cell parameters from a complete diffraction pattern. These algorithms have been developed and are used during the data analysis in the Jana computer program [126].

The phase purity of the different synthetized powders or sintered pellets was controlled by XRD. The X-ray analyses were carried out with the diffractometer D4 ENDEAVOR from the company Bruker. A typical measurement was in the range of diffraction angles 2θ from 10° to 80°, increment of 0.02° for 2θ and 075 second of measurement time per step. The data were analyzed with the program package X'Pert HighScore (PANalytical B.V., version 3.0.5).

High temperature XRD (HT-XRD) measurements were performed on an Empyrean diffractometer, PANalytical GmbH, in the temperature range of 25 to 700 °C, with an increment of 100 °C.

3.2.2. Rietveld refinement

The XRD patterns can provide detailed information about the crystal structure, atomic positions, lattice parameters and site occupancies of atoms within the unit cell upon fitting the shape and intensities of the reflections *via* Rietveld refinement method. This fitting method is named after H.M Rietveld [127, 128], who formulated mathematical expressions that can generate diffraction patterns similar to that of neutron powder diffraction patterns. After a decade the similar simulation was performed with XRD diffraction patterns [129]. This is due to the fact that any XRD pattern is a combination of several superimposing and overlapping Gaussian peaks in addition to background. A Rietveld refinement incorporates all these peaks for fitting the XRD pattern using combination of complex mathematical expressions [130].

With time and advancement of computation technology, the Rietveld method has been formulated into several computer programs significantly reducing the effort to perform such refinement. In this work, the crystallographic details of materials were determined using the Jana program [126] using full-matrix least-square fits against F_{hkl}^2 [131] method. For such a refinement, the program requires high resolution XRD patterns that were recorded using the same diffractometer as used by routine measurement but different parameters: 10 ° ≤ 2θ ≤ 140 ° with increment of 2θ of 0.01° increment for 2θ and measurement time of 2 sec at each step.

The mathematical expression used by H.M. Rietveld back in 1960 was complex, and he calculated the intensity $I_{c,i}$ at each 2θ step i as;

$$I_{c,i} = s \times \sum_{hkl} L_{hkl} \times |F_{hkl}|^2 \times \varphi(2\theta_i - 2\theta_{hkl}) \times P_{hkl} \times A + I_{b,i} \qquad \text{Eq. 5}$$

In this equation, the second intensity term $I_{b,i}$ is the intensity of the background, whereas the first term represents the contribution of every Bragg reflections and in each contribution both the crystal structure (atomic coordinates, thermal displacement and site occupancies) and the diffraction experiment (unit cell, peak profile broadening, etc.) are described with:

- s, the overall scale factor
- L_{hkl}, containing the Lorentz and polarisation factors as well as a multiplicity factor
- F_{hkl} , the structure factor for the (hkl)th Bragg reflection
- $\varphi(2\theta_i - 2\theta_{hkl})$, a profile function were $2\theta_i$ is the diffraction angle corrected for the 2θ zero error
- P_{hkl}, a preferred orientation function
- A, the absorption factor depending on the instrument geometry [130, 131]

3.3. Powder characterization

3.3.1. Elemental analysis (ICP-OES)

The stoichiometry of the materials was controlled by inductively coupled plasma optical emission spectroscopy (ICP-OES) using the **Thermo Scientific iCAP7600** spectrometer with optical scale and CID semi-conductor detector, axial und radial reflection, and wavelengths between 166 nm and 847 nm. 20 mg of powder were mixed to 0.25 g lithium borate in a platinum crucible and heated for 0.5 h at 1000 °C. The liquefied material was dissolved in 30 mL HCl (5%). After dissolution, the sample solutions were transferred to sample vials containing 0.5 ml of HF and filled to 50 mL volume. Each test sample was diluted and measured twice.

3.3.2. Particle size distribution

Laser diffraction spectroscopy was used for the particle size distribution (PSD) measurements. This technique utilizes the diffraction patterns of the laser beam targeted on sample particles. It is capable of measuring the particles ranging from nanometers to millimeters in size [132]. It can also measure the geometric dimensions of particles based on the Fraunhofer diffraction theory [133].

The particle size distribution was obtained using Horiba LA-950V2 laser diffraction particle size distribution analyzer with ethanol as dispersing medium[1].

3.4. Impedance spectroscopy

In the recent past, impedance spectroscopy has become one of a leading technique in the field of electrochemistry and materials science research. It allows investigation of numerous electrical as well as electrochemical properties of both solid and liquid state systems. The ionic-conducting, semi-conducting, mixed-conducting or dielectric and the dynamics of bound and mobile charge in the bulk and interfaces can be studied. Furthermore, information about microstructure, chemical composition, reaction parameters, corrosion rates, surface porosity, coating integrity, mass transfer, electrode or interface characteristics can be obtained [134-136].

---

[1] Courtesy of V. Nischwitz, Central Institute for Engineering, Electronics and Analytics, ZEA-3, Forschungszentrum Jülich GmbH

In this work, the ionic conductivity between 100 °C – 30 °C was determined on dense pellets with gold electrodes sputtered on the surfaces with a multi-potentiostat VMP-300 from Bio-Logic SAS, France. The used frequency range was 1 Hz – 7 MHz at intervals of 20 points per decade with amplitude of 50 mV.

The ionic conductivity at high temperature (30-400 °C) was measured in Ar (ProGasMix from NorECs) with the Alpha-A high performance modular measurement system (Novocontrol Technologies). The frequency range used was 1 Hz – 20 MHz at intervals of 20 points per decade with amplitude of 50 mV.

During the impedance measurement, a sinusoidal signal U_t with small amplitude U_0 is applied to the system electrode/sample/electrode:

$$U_t = U_0 \sin(\omega t) = U_0\, e^{j\omega t}, \omega = 2\pi f \qquad \text{Eq. 6}$$

where ω is the angular frequency and f is the AC signal frequency.

U_0 should be small enough to get a pseudo-linear response of the system. In this case as well as for linear systems, the current response to U_t is also a sinusoid at the same frequency but with a phase shift ϕ.

$$I_t = I_0 \sin(\omega t + \phi) = I_0\, e^{j(\omega t+\phi)} \qquad \text{Eq. 7}$$

where I_0 is the amplitude of the current response.

For pure resistive systems, the frequency-dependent phase shift ϕ is zero [134]. According to Ohm's law, the impedance can be calculated according to:

$$Z(\omega) = \frac{U_t}{I_t} = \frac{U_0\, e^{j\omega t}}{I_0\, e^{j(\omega t+\phi)}} = |Z|e^{-j\varphi} = Z' - jZ'' \qquad \text{Eq. 8}$$

where Z' and Z'' are real and imaginary components of the complex impedance [134].

Impedance measurements are performed in a defined frequency range at discrete frequency values. For each frequency, the magnitude $|Z|$ and phase ϕ are measured and Z' and Z'' are calculated and plotted against each other in the impedance spectra as a function of frequency.

An impedance spectrum is represented by imaginary or capacitive impedance on y-axis and real or resistive impedance on the x-axis. In such graphs, semi-circles representing different polarization processes occurring in the system electrode | sample |electrode are observed. Each semi-circle (or each polarization process) can be analyzed as a combination of capacitive and resistive properties. The spectra can be simulated and fitted using an equivalent circuit composed of capacitors and resistors. Other processes like diffusion, dielectric relaxation of charge carriers, ferroelectric properties, double layer and adsorption properties at an interface between electrode and sample can also be simulated [137] but they are beyond the scope of this thesis.

Table 3.1: Capacitance values and their possible related phenomena [138].

Capacitance / F	**Phenomenon responsible**
10^{-12}	Bulk
10^{-11}	Minor, second phase
10^{-11} - 10^{-8}	Grain boundary
10^{-10} - 10^{-9}	Bulk ferroelectric
10^{-9} - 10^{-7}	Surface layer
10^{-7} - 10^{-5}	Sample/electrode interface
10^{-4}	Electrochemical reactions

Impedance spectra of polycrystalline materials are often composed of two semicircles, each corresponds to a contribution of a certain process (bulk or grain boundary) and, as a sum, result in the total impedance. The semicircle visible at higher frequencies, generally called first semicircle, represents the contribution of bulk resistance. The first semicircle is an intrinsic property and mainly depends on the composition of material. The second semicircle appearing at lower frequencies arises from the grain boundary contribution to the total impedance. This semicircle is an extrinsic property and mainly depends on processing conditions and characteristics of the starting powder. A detailed description of the mathematical expressions used to calculate the total, bulk and grain boundary conductivities is given in section 4.2.4.

3.5. Microstructure

In scanning electron microscopy (SEM) a sample is subjected to a beam of electrons, and their interaction with the sample surface produces various signals that give information about the morphology and topology, composition and even electrical conductivity. The signals arise from differently scattered electrons:

- Back scattered electrons (BSE) give information about the composition. In this mode, the targeted electrons are scattered after an elastic collision. The number of BSE electrons reaching the detector is proportional to the mean atomic number ($\bar{Z}$) of the sample atoms. Heavy atoms appears brighter and vice-versa. When two elements have similar $\bar{Z}$, they produce similar brightness and therefore are indistinguishable.
- Secondary electron (SE) signal is used to obtain the surface topography and morphology of the samples. SEs are knocked off from outer shells of the sample atoms at the sample surface (few nm) as they are energized by the electron beam. The image is constructed based on the distance between emitted surface and detector. One major limitation is when the SE is emitted from edges of the sample, the so-called

"edge effect" in which the image appears brighter. In this work, both of the following signals were used [139].

An example comparing the images obtained from BSE and SE modes is shown in Fig. 3.2.

- A third mode is often used (not in this thesis) where X-rays are produced and emitted from the sample surface upon an inelastic collisions of the electron beam with the sample atoms. A special X-ray detector measures the wavelengths which correspond to the energy levels of the electrons in different shells of the respective element. This mode gives information about the composition of the sample. This mode is commonly known as energy-dispersive X-ray spectroscopy (EDX).

In this work, the SEM pictures were taken with a Zeiss Ultra 55 and a Zeiss Supra 50 VP[2] (Carl Zeiss NTS GmbH, German). The electronic conductivity of the samples was enhanced by sputter deposition of a thin platinum layer prior to the analysis.

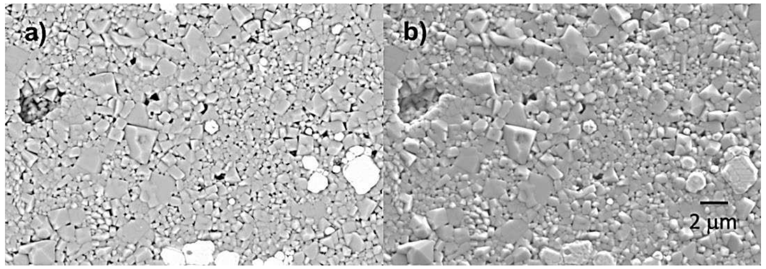

Fig. 3.2: Comparison of a) BSE and b) SE modes giving different information about NZSiP with ZrO_2 as secondary phase.

3.6. Thermal etching

The SEM images of polished cross-section were not good enough to observe the grain and the grain boundaries of NZSiP. This problem was overcome by thermal etching, in which a heat treatment of polished sample is performed at 1150 ºC for 15 min. Because the grain boundaries are more reactive than grains due to surface grooving by diffusion at high temperature and therefore are clearly visible when viewed at direct angles. If the temperature is too high or the time is too long, the sample may get over etched meaning that the grains also get oxidized, therefore the etching temperature and time was optimized after several trials. Fig. 3.3 shows a SEM image of NZSiP samples with and without thermal etch.

---

[2] Courtesy of Dr. D. Sebold, Material Synthesis and processing (IEK-1) and Dr. D. Grüner, Microstructure and properties of materials (IEK-2), Forschungszentrum Jülich GmbH

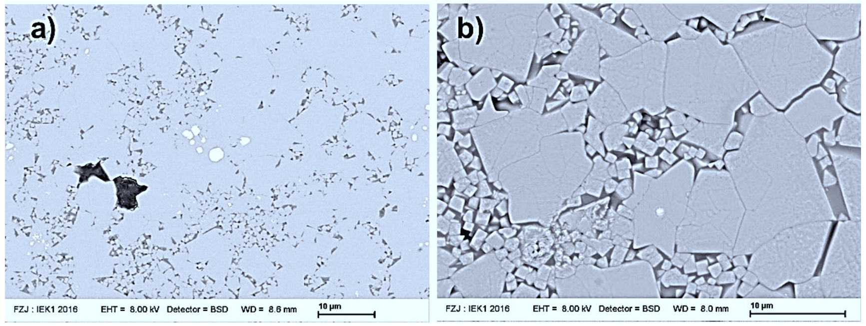

Fig. 3.3: The SEM image of NZSiP sintered at 1250 ^{o}C for 10 h with and without thermal etching.

3.7. Image analysis

SEM images were analyzed using the analySIS pro imaging software as shown in Fig. 3.4. The grain boundary identification process is semi-automatic and depends crucially on grain boundary discernibility. This can be achieved by chemical or, in this case, thermal etching. The SEM images with suitable resolution were loaded into the program and scales are calibrated. Subsequently, a “separator” command was used as a filter for separating objects (i.e. grains). With this filter, it is possible to separate segments of an image with different intensities, like particles’ interfaces. The separator creates light or dark lines dividing objects of the same color or creates objects distinguishable from the background due to their intensity value. The software is also able to edit the resulting image interactively. Finally, statistical data of microstructural parameters can be obtained. The color categories in Fig. 3.4 reflect different grain size intervals. Since the grain size was obtained from 2D images, a multiplication factor of 1.571 for tetrakaidecahedron-shaped particles was applied, according to the ASTM standard [140].

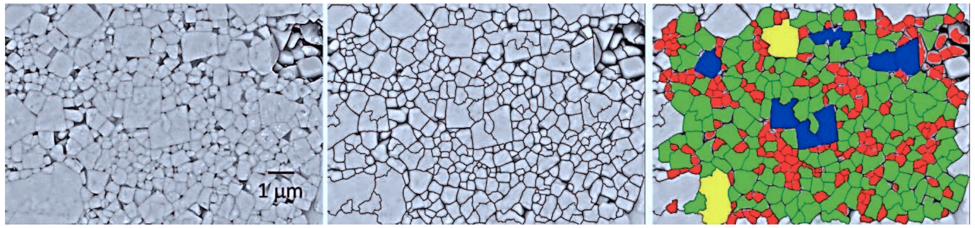

Fig. 3.4: Images of grain identification and size statistics using analySIS pro. The colors show different intervals of grain sizes where left is the original image, middle shows grain boundary identification and right depicts the grain size categorization.

3.8. Thermal Analysis

3.8.1. DTA/TG

Differential thermal analysis / thermogravimetry (DTA/TG) and differential scanning calorimetry / thermogravimetry (DSC/TG) measurements were carried out with the thermal analyzer STA449 F1 Jupiter coupled to the mass spectrometer QMS 403C Aëolos both from the company Netzsch. In both cases, two methods are applied simultaneously to one sample: TG with DTA or TG with DSC.

During a TG experiment, the changes in weight are measured in dependence on temperature and give information about the thermal stability, the purity and the presence of humidity in a sample.

The DTA experiment records the temperature differences between the sample and a reference while they undergo identical thermal treatments; a DTA curve is therefore a plot of the differential temperature against temperature (or time) and the peaks orientation depends on the observed phenomenon either as exothermic (downwards peak) or endothermic (upwards peak). For example, the following phenomenon can be observed:

- Crystal structure change, phase transition (exo- or endothermic)
- Crystallization (exothermic)
- Melting (endothermic)
- Solid state reaction (exo- or endothermic)
- Oxidation or reduction (exothermic)

The DSC experiment records the quantity of heat that is absorbed or released by a substance undergoing a physical or a chemical change during a thermal treatment. There again, the orientation of the peak indicates an exothermic (crystallization, decomposition) or endothermic (glass transition, melting, evaporation) phenomenon [141]. In this experiment, the height of the peaks is directly influenced by the heating rate. A mass spectrometer is coupled to the DSC/TG in order to get information about the nature of the species released from the sample during the heating.

3.8.2. Dilatometry

The dilatometry experiments were carried out with dilatometers 402C and 402E from Netzsch. During the measurement, a sample is heated and its length change is recorded.

The dilatometer 402 was used on sintered samples to measure the dimensional changes as a function of temperature to determine the coefficient of thermal expansion (*CTE*). In a temperature range ΔT, a sample with a reference length L_0 will have a length change ΔL and its *CTE* is calculated according to:

$$CTE = \frac{\Delta L}{L_0 \Delta T} \qquad \text{Eq. 9}$$

From the dilatometer measurement, a plot of $\frac{\Delta L}{L_0}$ against the temperature is obtained and CTE can be calculated from the slope of the linear data.

Dilatometry experiments with dilatometer 402 were also carried out on hand-pressed powder to get knowledge on the sintering behavior. Since the shrinkage of the sample is recorded during the dilatometry experiment, the data can be used to adjust the proper sintering conditions for the systematic studies of the grain size and morphology changes [142]. During the sintering experiment, the sample is heated up to a given temperature and the temperature is hold for a given time. $\frac{\Delta L}{L_0}$ is plotted against the temperature or against the time during the isothermal period of the thermal program.

Chapter 4: Results and Discussion Part I: Investigation of NZSiP

4.1. Synthesis of NASICON

4.1.1. Motivation

Materials synthesis is the first step towards the applicability of any material. In this chapter, the NASICON composition $Na_3Zr_2Si_2PO_{12}$ (hereafter: NZSiP) is synthesized and characterized to understand the influence of the synthesis route on the sintered product.

In the past, several methods have been used to synthesize NZSiP, which include:

- Conventional solid-state reaction [86, 87, 143],
- Precursor based sol-gel methods (i.e. metal alkoxides [29, 144-148], citrate gel (Pechini's method [149]) [150, 151], silica gel [152-154],
- Hydrothermal synthesis [155-157]),
- Nonhydrolytic synthesis [158],
- Coprecipitation [95],
- Mechanochemical synthesis [159], and
- Combustion method [160]

Conventional high-temperature solid-state reaction (SSR) is the most simple synthesis method that involves mixing the oxides, hydroxides or carbonates of the cations followed by calcination and sintering at high temperature to get the desired material [161]. Reaction at high temperature can result in secondary phase formation (i.e. monoclinic ZrO_2) due to elevated partial pressure of sodium and phosphorous compounds [151]. So far, to our knowledge the best reported total conductivity achieved using SSR powder is $1.2 \cdot 10^{-3}$ S cm^{-1} at 25 °C [162].

Sol-gel derived methods involve reactions at low temperature, where monomers are converted into a colloidal solution (sol) and act as precursor for an integrated network (gel) for either discrete particles or network polymers [163]. Based on the type of precursors, sol-gel synthesis can be classified into metal-organics, metal-citrates, metal-silicates and hydrothermal synthesis [161]. The best reported conductivity of NZSiP prepared from sol-gel powder is $6.6 \cdot 10^{-4}$ S cm^{-1} at 25 °C and 0.11 S cm^{-1} at 300 °C [164].

Nonhydrolytic synthesis involves a reaction of precursor materials in anhydrous solvents like CH_3CN followed by addition of a sodium source and calcination to obtain the NASICON material [158]. In mechanochemical synthesis, metal oxides are ball-milled in ethanol, dried, and mechanically activated in a planetary ball mill before calcination to achieve a NASICON phase.

Samples produced by sintering of co-precipitated powder have low conductivity of $9.2 \cdot 10^{-5}$ S cm^{-1} [95]. The highest conductivity of $1.8 \cdot 10^{-3}$ S cm^{-1} at 25 °C is reported for spark plasma sintering of SSR powder. However, it is an expensive fabrication route and therefore industrially less viable [165]. The density of specimens is however not always reported. These methods along with the advantages and disadvantages are summarized in Table 4.1.

Table 4.1: Summary of various synthesis methods reported for NZSiP comparing advantages and disadvantages of the applied methods.

Method		Advantages	Disadvantages	Ref.
Solid state reaction		▪Simple and easy ▪Cheap raw materials	▪High temperature sintering ▪Large particle size ▪Inhomogeneity	[86, 87, 143]
Sol-gel synthesis applying	Metal alkoxides	▪Molecular mixing of precursors prior to hydrolysis ▪Good homogeneity ▪High purity ▪Low sintering temperatures (reduced loss of volatile and metastable phases) ▪Industrial application: coatings, thin films, fibres, nano powder production	▪Complex chemistry ▪Sensitive reactions involved	[29, 144-148]
	Citrate gel (Pechini)			[150, 151]
	Silica gel			[152-154]
	Hydrothermal synthesis			[155-157]
Nonhydrolytic synthesis		▪Easy control of hydrolysis rate ▪Volatile byproducts ▪Broad solvent choice ▪Careful control of process	▪Byproduct formation ▪Toxic solvents	[158]
Coprecipitation		▪Chemical homogeneity ▪Molecular mixing ▪Nano-powder ▪Careful control of solution conditions	▪Post washing and drying procedures	[95]
Mechanochemical synthesis		▪Particle size control	▪Long time ball milling ▪Poor microstructure control	[159]
Combustion		▪Nano powder ▪Good homogeneity	▪Sensitive parameter control ▪Only useful for small batches	[160]

In the present study, we applied a so-called "solution-assisted solid state reaction" (SA-SSR), method for synthesizing NASICON materials. SA-SSR involves cheap raw materials (water- or acid-soluble salts), no sensitive parameter control and easy scale-up. For comparison, NZSiP was also synthesized by Pechini’s method and processed by similar conditions, as shown in the schematic Fig. 4.1. Both the synthesis methods are already described in the section 3.1.

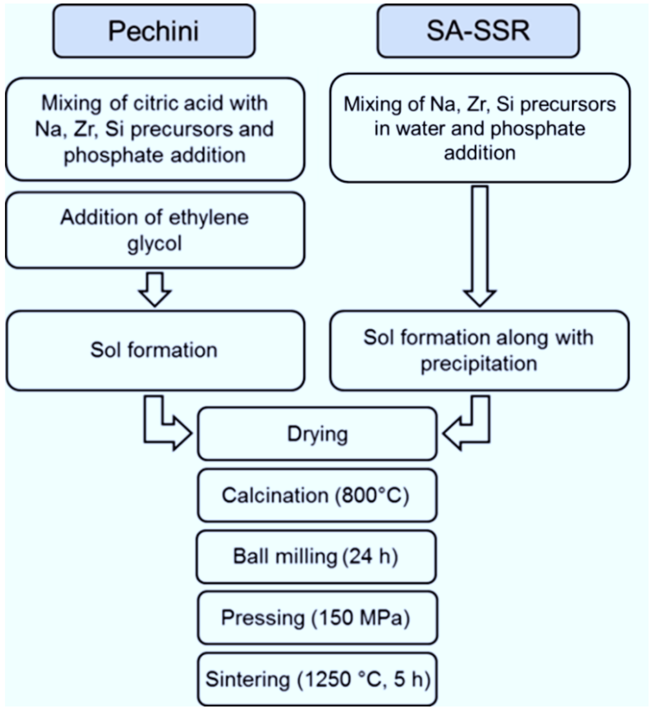

Fig. 4.1: Illustration of the preparation steps involved in Pechini and SA-SSR methods of synthesizing NASICON material.

4.1.2. X-ray diffraction

The X-ray diffraction patterns of NZSiP synthesized by Pechini method and SA-SSR at different stages of heat treatment are shown in Fig. 4.2. Dried products contain precipitates of $NaNO_3$ in both samples due to the lack of gelation at 25 °C. Until 600 °C, the Pechini sample is amorphous, whereas SA-SSR sample still contains small amounts of $NaNO_3$. At 700 °C, both powders start to crystallize into the desired NASICON structure. After calcination at 800 °C for 12 h, crystallization of both samples is much more pronounced but the reflections are still broad. In the SA-SSR sample broader peak widths are indicating an existence of finer particle size distribution as compared to the Pechini powder. This observation is also confirmed by the SEM images of the powders (see Fig. 4.6). In addition, the Pechini powder shows the crystallization of a second phase corresponding to a disilicate besides the NASICON reflections.

After sintering at 1250 °C for 5 h, a well crystallized monoclinic NASICON structure (space group C2/c) is obtained for both samples. In both cases the samples contain monoclinic ZrO_2 as secondary phase in different amounts. The reflection intensity of ZrO_2 is stronger in the

Pechini sample, indicating a lower amount of ZrO_2 in the SA-SSR sample. Rietveld refinement estimates the ZrO_2 amount to be 3 and <1 wt. % in the Pechini and SA-SSR sample, respectively. This difference is due to different reaction paths in developing the NASICON structure, i.e. Pechini samples first form an amorphous network (see XRD pattern at 600 °C) whereas, the SA-SSR samples directly start to crystallize the attempted crystal structure even though the XRD reflections after heat treatment 600 °C still indicate a high degree of disorder and very small crystallites.

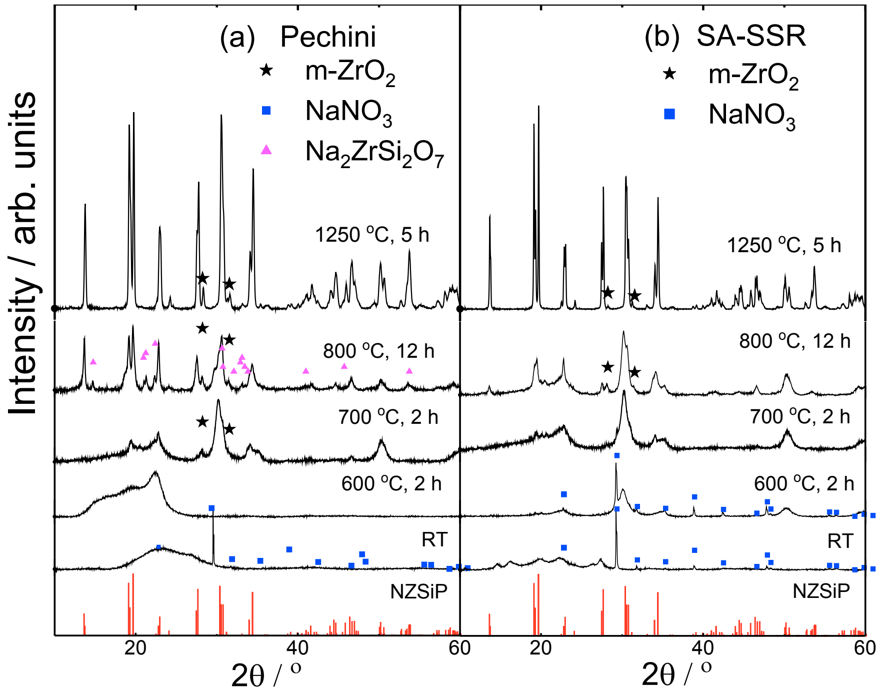

Fig. 4.2: Phase evolution of NZSiP at different temperatures prepared by the Pechini method (left) and by SA-SSR (right). The reference pattern of $Na_3Zr_2(SiO_4)_2(PO_4)$ [166], monoclinic ZrO_2 [167], $NaNO_3$ [168] and $Na_2ZrSi_2O_7$ [169] from literature.

The formation of ZrO_2 during the densification of NZSiP was also observed by other synthesis and processing methods [22, 95, 165]. This is due to an earlier crystallization of ZrO_2 prior to the NASICON formation resulting from the high thermodynamic stability of ZrO_2 and not due to volatility of reagents (e.g. sodium monoxide) at the sintering temperature. In this case, ZrO_2 starts to crystallize at 700 °C for Pechini and 800 °C for SA-SSR powders. A small amount of ZrO_2 has a minimal impact on Na^+ conduction considering percolation theory. However, higher amounts of ZrO_2 may reduce the Zr content from the

NASICON phase resulting in stoichiometric differences that can significantly influence the conductivity [122, 170].

4.1.3. Elemental analysis (ICP-OES)

The chemical analysis of the NASICON materials synthesized by the two different methods reveals the stoichiometries of $Na_{2.98\pm0.02}Zr_{1.94\pm0.01}Si_{1.94\pm0.01}PO_{12}$ and $Na_{2.95\pm0.02}Zr_{1.92\pm0.01}Si_{1.81\pm0.01}PO_{12}$ for the Pechini and SA-SSR powder, respectively. The obtained atomic ratios were normalized to one phosphorous atom per formula unit. The deviation of the Zr contents might be explained by the purity level of the educt and presumably by adsorbed water during storage of the $ZrO(NO_3)_2$. The deviations of the Si contents up to 10 % are significant and also seem to be related to the educt. Further studies are necessary to better control the Si contents and to understand the impact of Si deficiency in the materials.

The carbon content after calcination was measured to be 0.116 ± 0.012 and 0.059 ± 0.001 wt. % in Pechini and SA-SSR powders, respectively, indicating that calcination at 800 °C results in almost complete removal of carbon.

4.1.4. Particle size and Morphology

The particle size distribution (PSD) of Pechini and SA-SSR powders before and after ball milling is shown in Fig. 4.3. Before ball milling, Pechini powder has a mono-modal PSD and an average agglomerate size of ~105 µm. The SA-SSR powder, however, has a bimodal PSD averaging at ~10 µm and ~60 µm. This observation is in agreement with the powder morphology observed in the low magnification SEM images in Fig. 4.4a and 4.4b. In general, Pechini powder has similar sized agglomerates, whereas SA-SSR powder is composed of a wide range of diverse sized agglomerates. Nevertheless, after ball milling, PSD of both powders is indistinguishable (Fig. 4.3b) averaging at about 2 µm, also confirmed in Fig. 4.4c and 4.4d.

The Brunauer–Emmett–Teller (BET) surface area of Pechini and SA-SSR milled powder is 7.64 $m^2\,g^{-1}$ and 3.94 $m^2\,g^{-1}$, respectively, indicating that surface area is profoundly affected by the morphology of particles after calcination although the particles have the same sizes.

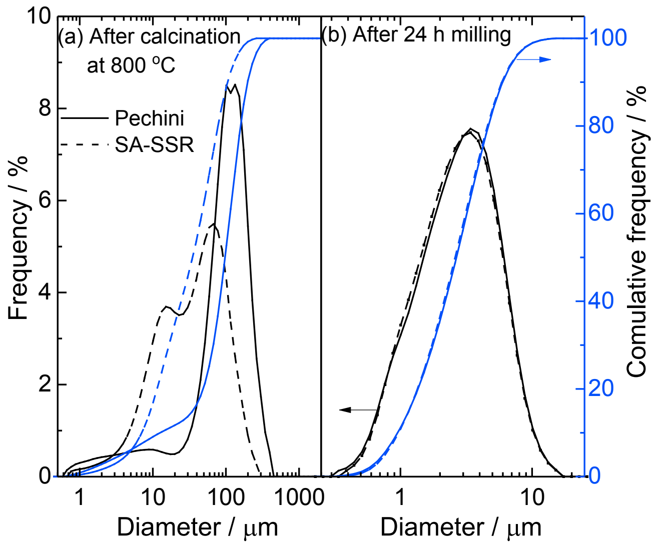

Fig. 4.3: The particle size distribution of the powders (a) after calcination at 800 °C for 12 h in air and (b) after subsequent ball milling for 24 h with zirconia balls in ethanol.

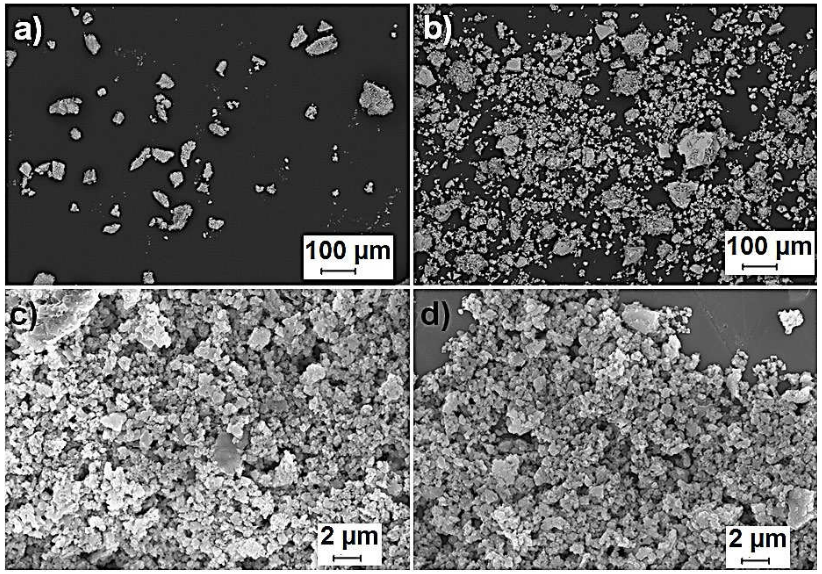

Fig. 4.4: Visualization of the size distribution of Pechini and SA-SSR powders by SEM before (top) and after (bottom) ball milling. The dark background is a carbon tape used during sample preparation.

Fig. 4.5 shows Pechini and SA-SSR powders of NZSiP after calcination at 800 °C for 12 h in air at higher resolutions. The morphology of powder agglomerates before 24 h ball milling is presented in Fig. 4.5a-4.5d. The Pechini powder (Fig. 4.5 a and 4.5c) has a majority of regular submicron-sized grains of 0.3-0.5 µm and a small amount of comparatively smaller particles. The SA-SSR powder (Fig. 4.5b and 4.5d) has a very different morphology. Instead of individual grains, the powder consists of ultrafine particles (0.1-0-2 µm) at the surface of larger agglomerated grains. Apparently, these grains are comprised of even smaller particles which are already densified as a result of the heat treatment. The very small particle sizes visible here also explain the broadening of XRD reflections in Fig. 4.2.

Fig. 4.5 (e, f) shows the powders after ball milling. Both powders have similar agglomerate morphology, as confirmed by the PSDs in Fig. 4.3b. The secondary phases could not be identified by phase contrast in back-scattered images (not shown here).

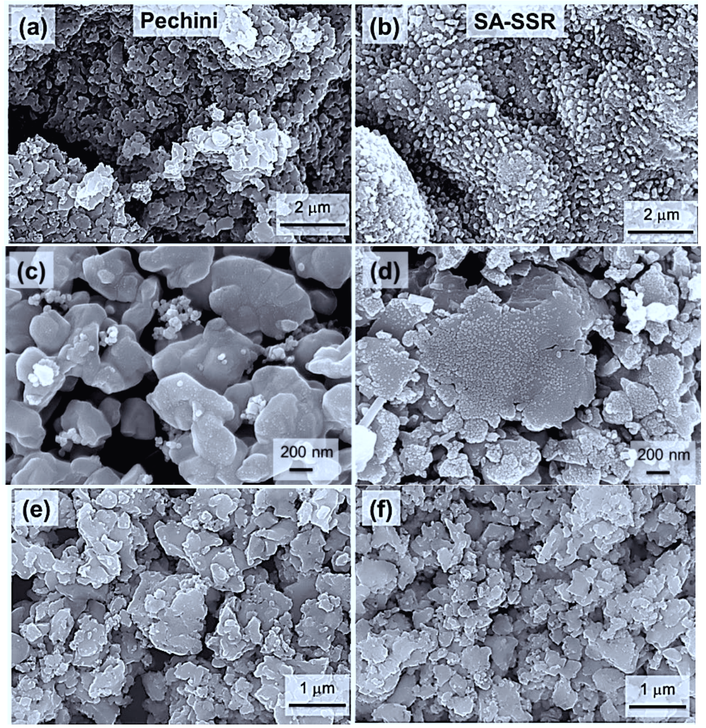

Fig. 4.5: The SEM images of powder synthesized by Pechini method (left) and SA-SSR method (right). Here, (a – d) are before and (e, f) are after ball milling. Both powders were calcined at 800 °C for 12 h in air.

4.1.5. Microstructure

SEM images of polished cross-section and fracture surface of sintered specimens sintered at 1250 °C for 5 h is shown in Fig. 4.6. Fig. 4.6a-b reveals a higher monoclinic ZrO_2 concentration in Pechini than in SA-SSR sample. A set of cross-section images was analyzed using AnalysisPro software to determine the phase percentages based on grey scale differences. The percentage area of ZrO_2 phase is 0.6±0.1 and 3.5±0.5, of pores about 7.5±1.2 and 5.5±0.3 and the fraction of main phase is about 91.8±1.3 and 91.9±0.8 for SA-SSR and Pechini specimen, respectively. The fraction of ZrO_2 obtained through image analysis agrees with the Rietveld refinement of the XRD reflection patterns. The density of SA-SSR and Pechini samples was 2.97 g cm^{-3} and 3.02 g cm^{-3}, respectively, as compared to the theoretical value of 3.26 g cm^{-3}.

In addition to the secondary phase, polished sintered surface in Fig. 4.6c-h and fracture surfaces in Fig. 4.6i-j reveals that both samples have bimodal-type grain size distribution. However, the SA-SSR sample has a homogeneous grain growth resulting in noticeably larger grain size as compared to the Pechini sample. Since the fabrication conditions of both samples were same and their green density was within 59-61 %, the difference can only come from sinterability difference induced by the powder synthesis route. Furthermore, more homogeneous and larger grain size in samples sintered from SA-SSR powder would result in a lower grain boundary resistance, as discussed in section 4.1.6.

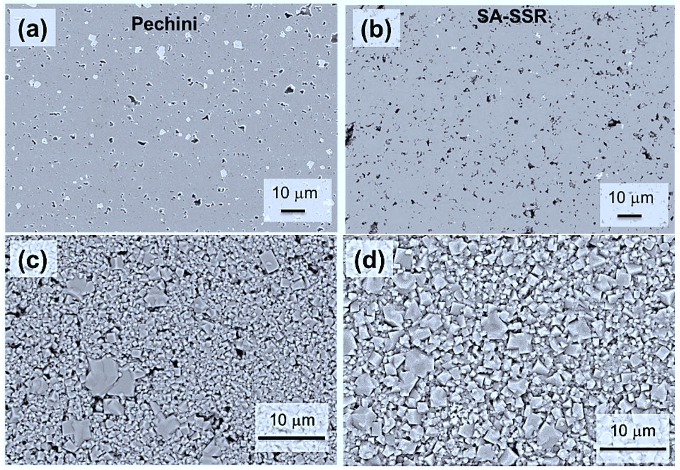

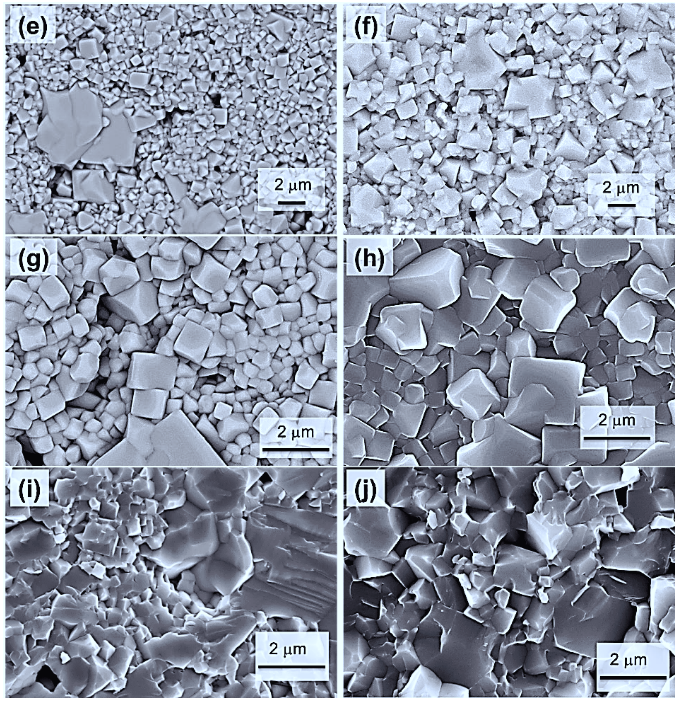

Fig. 4.6: SEM microstructure of NZSiP sintered at 1250 °C for 5 h in air. (a, b) are polished cross-sections, (c-h) are sintered surfaces and (i, j) are fracture surfaces of samples sintered from powders made by Pechini method (left) and SA-SSR (right), respectively.

4.1.6. Electrical conductivity

The Nyquist plots of the impedance spectra obtained for both NZSiP samples are shown in Fig. 4.7. Fitted curves using the given equivalent circuits are also shown. At 25 °C (Fig. 4.7a), only one semicircle appears for both specimens at high frequencies, a straight line is observed at low frequencies. The straight line is due to Na^+ blocking response at the interface of gold electrodes, referred to as electrode polarization. The arc is not originating from zero at 25 °C, indicating that bulk conductivity (σ_b) and grain boundary conductivity (σ_{gb}) is not clearly distinguishable and only the grain boundary is observed in this frequency range. They can be better distinguished either by reducing the measurement temperature or by increasing the measurement frequency. In our case, temperature was reduced to -20 °C and the phenomenon is evident by the appearance of two semicircles, as shown in Fig. 4.7b.

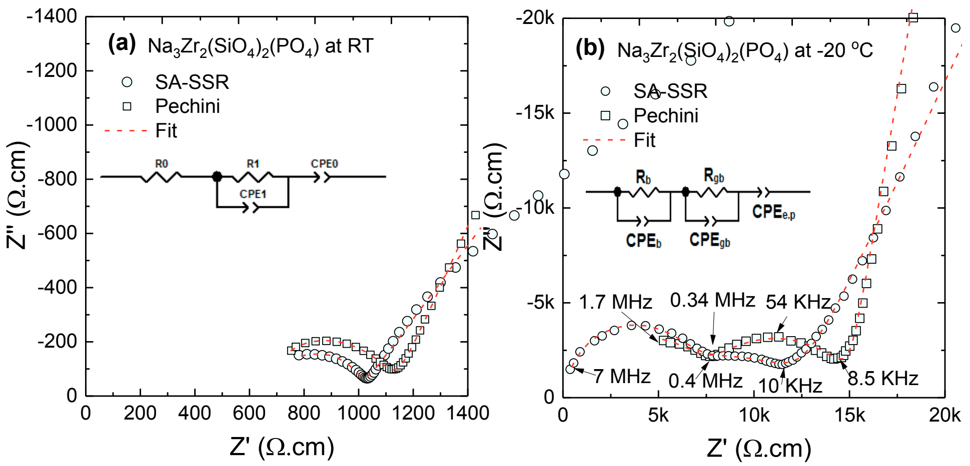

Fig. 4.7: Nyquist plot of NZSiP samples prepared by the Pechini method and SA-SSR measured at (a) 25 °C and (b) -20 °C. Samples were pressed and sintered at 1250 °C for 5 h in air. The equivalent circuits used to fit the impedance spectra are also shown. The sample dimensions were used to calculate the specific resistance values.

In order to quantify the contribution of σ_b and σ_{gb}, equivalent circuits are used and shown in Fig. 4.7. At -20 °C, the resistances represent the ionic conduction in bulk (R_b) and grain boundaries (R_{gb}). For both samples, resistances are obtained by fitting impedance spectra and extracting the lowest value of -Z" as total resistance (R_{Total}). The constant phase element (CPE) represents a non-ideal capacitive contribution of transport processes in the bulk (CPE_b), grain boundaries (CPE_{gb}) and at electrode/electrolyte interface at low frequencies (CPE_{el}). At 25 °C, only half of the semicircles appear, therefore fitting of σ_b and σ_{gb} is not precise. However, it is possible to accurately determine the total conductivity ($\sigma_{Total} = \sigma_b + \sigma_{gb}$).

In Fig. 4.7b, at frequencies lower than 8 kHz, a straight line is observed due to the electrode polarization. The semicircle in the high frequency range (1-7 MHz) can be attributed to bulk and the middle frequency range (5 kHz-1 MHz) to grain boundary processes. The capacitance associated with the high frequency arc is found to be around 10^{-11} F and the one associated to the lower frequency arc lies between 10^{-9} and 10^{-8} F. High frequency arc is identified as bulk property from the fact that capacitance is of the order of pF and lower frequency arc as grain boundary property since capacitance is in the nF range. The third capacitance represented by CPE_{el} is in the order μF and can be associated to the polarization of electrode [29].

Conductivity of both samples was measured as a function of temperature in the range of -30 to 100 °C (Fig. 4.8). The conductivity follows an Arrhenius law and the activation energy obtained for both samples is similar and in agreement with previous studies [86, 87].

The bulk and grain boundary conductivities of pellets were calculated from R_b and R_{gb} obtained from fitting the equivalent circuits, and plotted as a function of inverse temperature in Fig. 4.8. Up to 60 °C, the bulk and grain boundary conductivities were differentiable, at higher temperature there is no semicircle formation. The conductivity follows an Arrhenius law and the activation energy, also given in Table 4.2, was calculated from the slope of the straight line in an ln (σ_{Total}) vs. 1/T plot. At -20 °C, where two semicircles clearly appear, σ_{Total} of the Pechini and SA-SSR sample is 7.3×10^{-5} S cm^{-1} and 9.2×10^{-5} S cm^{-1}, respectively. The σ_b for both specimens is similar ~1.6×10^{-4} S cm^{-1}, whereas σ_{gb} of SA-SSR specimen is two times higher than σ_{gb} of Pechini sample. Furthermore, a similar trend is observed at 25 °C (Table 2). Total conductivity of the sintered samples using Pechini and SA-SSR powder is 8×10^{-4} S cm^{-1} and 1×10^{-3} S cm^{-1}, respectively. These values are very close to the highest reported conductivity for this material via spark plasma sintering, i.e. 1.8×10^{-3} S cm^{-1} [165].

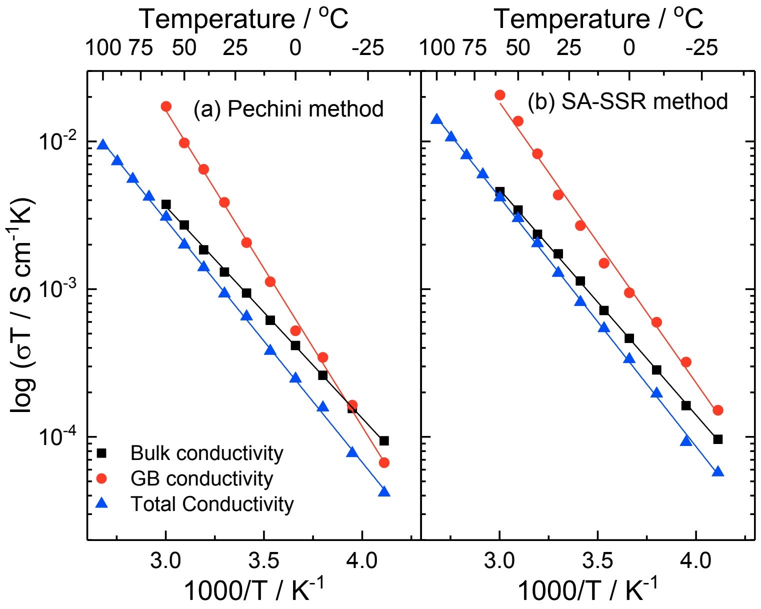

Fig. 4.8: Arrhenius plot of NZSiP synthesized by (a) Pechini method and (b) SA-SSR method. The activation energies are also shown. Grain, grain boundary and total conductivities are obtained after fitting with the equivalent circuits (Fig. 4.7).

Table 4.2: The total conductivities measured at 25 °C and 100 °C and the activation energies of the NASICON material synthesized by both methods.

Method	**$E_{a, bulk}$ (eV)**	**$E_{a, gb}$ (eV)**	**$E_{a, Total}$ (eV)**	**$\sigma_{25\ ^oC}$ (10^{-3} S cm^{-1})**	**$\sigma_{100\ ^oC}$ (10^{-3} S cm^{-1})**
Pechini	0.309 ± 0.002	0.449 ± 0.007	0.352 ± 0.002	0.8	9.4
SA-SSR	0.327 ± 0.002	0.401 ± 0.010	0.361 ± 0.002	1	13.9

The differences in conductivity can be explained in terms of activation energies of bulk ($E_{a,b}$), grain boundary ($E_{a,gb}$) and total conductivity ($E_{a,total}$). $E_{a,total}$ for Pechini and SA-SSR samples are similar, 0.352 ± 0.002 eV and 0.361 ± 0.002 eV, respectively, which are slightly higher than literature values (0.29 and 0.33 eV [29, 87]). $E_{a,b}$ values are also similar, 0.309 ± 0.002 eV and 0.327 ± 0.002 eV, respectively. However, the $E_{a,gb}$ differs substantially, i.e. 0.449 ± 0.007 eV and 0.401 ± 0.010 eV for Pechini and SA-SSR sample, respectively.

The comparable $E_{a,b}$ of both materials accounts for identical conduction mechanisms of ionic migration within grains, which depends mainly on crystal structure and sodium positions/vacancies and not on synthesis method [91]. Conversely, a significant dissimilarity in $E_{a,gb}$ implies that ionic migration across the gain boundaries is different for both samples. Since the relative density of green and sintered pellets for both samples was comparable, smaller grain boundary resistance of SA-SSR ceramic can only be attributed to its enlarged grain size and differences in stoichiometry. Henceforth, the sinterability of material and its sintering conditions play a key role in the microstructure and the grain boundary chemistry. Furthermore, it also elucidates the reason why different synthesis methods reported in literature (Table 4.1) have shown different total conductivity values for NZSiP.

The high σ_{Total} and lower $E_{a,gb}$ of the SA-SSR pellet is explained based on the microstructure in Fig. 4.6. There are two reasons: first is higher concentration of monoclinic ZrO_2 in Pechini-synthesized pellet (Fig. 4.6a-b). It is not ZrO_2 itself that contributes to a lower conductivity because the amount is so low that it does not have a significant impact in a two-phase mixture [171, 172]. It is rather the fact that higher ZrO_2 content lowers the Zr content in the main NASICON phase and evidently has a significant impact on conductivity at grain boundaries. The second reason is related to the coarser grains of SA-SSR sample as compared to Pechini sample (Fig. 4.6c-h). Larger grains reduce the amount of total grain boundary area incurred by charge carriers (Na^+) and the consequence is a lower R_{gb}. Since the fabrication conditions of the sintered bodies were same, the difference can only result from the powder characteristics and their sintering properties.

In addition to better electrical conductivity, the SA-SSR method has several other advantages over Pechini method. 1) It is cheaper, as it does not involve citric acid and ethylene glycol that are essential in Pechini's process. 2) As a consequence, during calcination, less CO_2 is released and therefore powders in large amounts can be produced cleanly. This is a significant benefit, because, as an example, the synthesis of one kg of NASICON requires about 4.0 kg of ethylene glycol and 4.3 kg of citric acid that results in CO_2 emission in large amounts during calcination. 3) Furthermore, the method is simple, water-based and requires no sensitive parameter control.

Fig. 4.9 shows a comparison of electrical conductivity of various sodium ion-conductors including NZSiP synthesized by SA-SSR, Pechini, SSR, sol-gel (aqueous and $M(OR)_4$) and co-precipitation methods. All conductivities shown in this figure represent σ_{Total}. The figure shows that both this materials exhibit higher conductivity than NZSiP prepared by other methods so far, except the sample sintered by spark-plasma sintering.

In addition, a comparison of NZSiP electrolyte with cubic Na_3PS_4 glass-ceramic [173], NASICON-type $Na_{3.2}Hf_2Si_{2.2}P_{0.8}O_{12}$ [120] and β-alumina (consisting of a mixture of β and β'' phases) [28] is also shown in Fig. 4.9. The NASICON-type material $Na_{3.2}Hf_2(SiO_4)_{2.2}(PO_4)_{0.8}$ has a conductivity of $\sim 2.3 \times 10^{-3}$ S cm^{-1} at 25 °C with an activation energy of 0.36 eV till 100 °C and 0.19 eV for higher temperatures [120]. Another highly conductive material is β-alumina having conductivity in the order of 10^{-3} S cm^{-1} at 25 °C. However, it requires sintering at high temperature (1600-1800 °C) in order to achieve high density and to reduce the grain boundary resistance [28]. Although the conductivity of β-alumina is higher at lower temperature, the conductivity of $Na_3Zr_2(SiO_4)_2(PO_4)$ synthesized by SA-SSR becomes equal to that of β-alumina at 50 °C, and at temperatures >50 °C the conductivity of $Na_3Zr_2(SiO_4)_2(PO_4)$ is higher. The glass-ceramic Na_3PS_4 is another class of material having a conductivity of $\sim 3 \cdot 10^{-4}$ S cm^{-1} at 25 °C which is lower than NZSiP.

This shows that the use of SA-SSR to synthesize NZSiP results in high conductivity and also gives the advantages of a simple and easy preparation method.

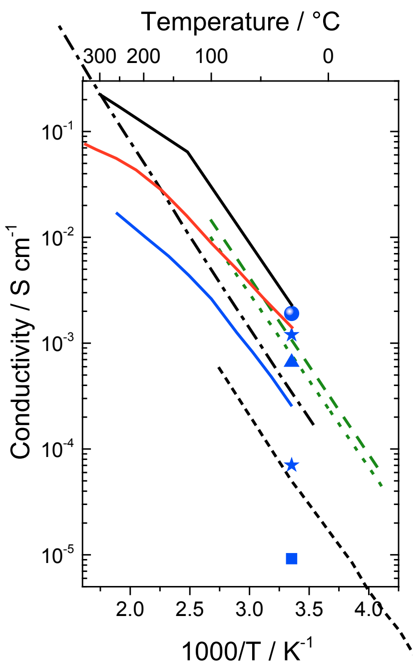

Fig. 4.9**:** Arrhenius plot of NZSiP synthesized by SA-SSR (green dashed line), Pechini (green dotted line), xerogel (short-dashed line) [29], SSR (dashed-dotted line) [87], co-precipitation (square) [95], sol-gel aqueous (triangle) [164], SSR (stars) [95, 162] indicating the wide range of possible conductivity data obtainable with this method, and SSR combined with spark-plasma sintering (sphere) [95]. Comparison with other high Na-ion conductive materials are shown as solid lines, i.e. glass-ceramic Na_3PS_4 (blue) [173], NASICON-type $Na_{3.2}Hf_2Si_{2.2}P_{0.8}O_{12}$ (black) [120] and β/β″-alumina sintered body (red) [28].

4.2. Processing of NASICON

4.2.1. Motivation

Due to the high potential of NZSiP, it was further processed at various sintering conditions to optimize the electrical properties and to understand its microstructural evolution. Because of a wide spread of NZSiP from 9.2 × 10^{-5} S cm^{-1} [95] to 1.0 × 10^{-3} S cm^{-1} [122] for conventional sintering and 1.8 × 10^{-3} S cm^{-1} [165] for spark plasma sintering. A wide scatter of conductivity data is due to the difference in density and microstructure of NZSiP, which is directly influenced by its processing conditions.

Ceramic processing therefore is the quality-determining step of any polycrystalline material and the main reason for different total conductivity of NASICON materials [75]. More precisely, the quality of a ceramic is determined by the powder characteristics and the sintering conditions. Powder characteristics (particle size distribution, particle shape, and sintering activity) strongly depend on synthesis method. Shaping (pressing, casting, printing etc.) and subsequent sintering determines the density and microstructure of the ceramics. The total conductivity of materials therefore is directly influenced by these aforementioned factors. Table 4.3 enlists various processing conditions and reported conductivity values, indicating a profound influence of processing conditions on the total conductivity of NZSiP material.

Table 4.3: Various synthesis methods, processing parameters and conductivities at room temperature reported for NZSiP.

Method		σ (mS cm^{-1})	Activation energy (eV)	Compaction pressure (MPa)	T_s (°C)	t_s (h)	Obtained $\rho_{relative}$ (%)	Ref.
Solid state reaction		0.75 1.2	0.38	300 200	1175 1275	5, 24 25	~98	[87, 143, 162, 166]
Solution assisted solid state reaction		1.0	0.36	150	1250	5	~93	[122]
Sol-gel derived	Metal alkoxides	0.6	0.33	100	1200	0.5	~ 70	[29, 144-148]
	Citrate gel (Pechini)	0.86	0.35	150	1250	5	~91	[122]
	Silica gel	0.66	0.40	-	1200	48	~ 85-95	[152-154]
Nonhydrolytic		-	-	-	1150-1200	15-20	92-95	[158]
Coprecipitation		0.12	-	300	1175	5	-	[95]

In in this study, the impact of sintering time and temperature was systematically investigated by keeping the powder properties constant. For this purpose, pellets with a constant green density were sintered at T_s = 1200 and 1250 °C for t_s = 0, 2, 4, 6, 8 and 10 h each. The obtained pellets were studied with scanning electron microscopy and impedance spectroscopy to investigate the microstructural properties on bulk and grain boundary resistance.

4.2.2. X-ray diffraction

The XRD patterns were recorded to investigate the phase purity of SA-SSR synthesized NZSiP after sintering at 1250 °C and different times (Fig. 4.10). In all samples, monoclinic ZrO_2 was detected in addition to a well crystallized monoclinic NASICON structure (space group C2/c). The amount of ZrO_2 was estimated to be 4 wt.% for t_s = 4 h and 1 wt.% in case of t_s = 0 h, whereas all other samples contain 2 wt.% ZrO_2. In addition, a small reflection at 2θ = 28.06° may indicate a formation of SiO_2. The formation of ZrO_2 is already discussed previously in section 4.1.2.

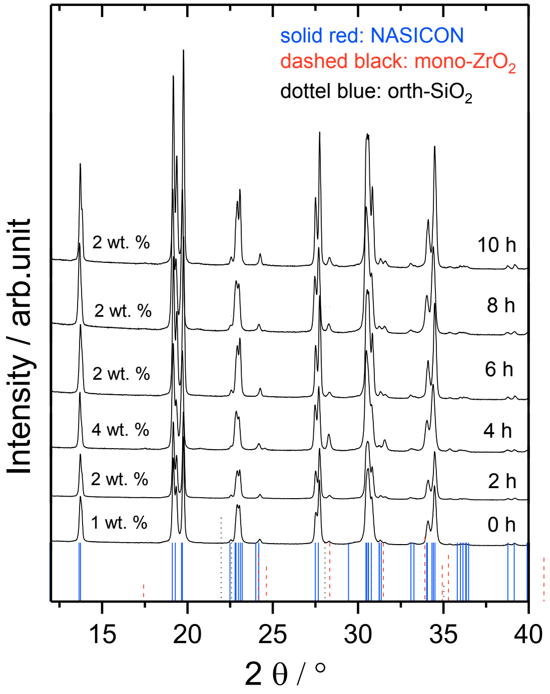

Fig. 4.10: The XRD patterns of NZSP sintered at 1250 °C applying different dwell times. As a reference, the diffraction patterns of observed phases, i.e. NZSiP (blue-solid) [166], monoclinic ZrO_2 (red-dashed) [167] and orthorhombic SiO_2 (black-dotted) [174] are also shown as vertical lines at the bottom. The percentage values denote the content of ZrO_2 in weight percent.

The chemical analysis of SA-SSR synthesized NZSiP at all sintering conditions is shown in Fig. 4.11. Overall, the Na contents lie within the expected range for all compositions considering the experimental error of ±3 %. However, a slight Na loss was observed in the 1250 °C sintered pellets compared to those sintered at 1200 °C, which is due to evaporation of sodium oxide. However, the Zr and Si contents are similar at both T_s, nevertheless Zr was lower than expected in all samples. It must be mentioned here that the starting powder for all samples was synthesized via SA-SSR, as described in section 4.1.

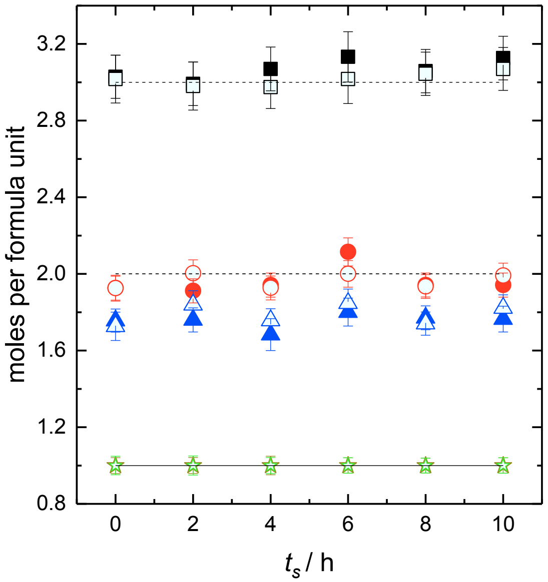

Fig. 4.11: Analytical stoichiometries of NZSiP obtained from ICP-OES. The filled and empty black squares (Na), red circles (Si), green stars (P) and blue triangle (Zr) represent samples sintered at 1200 °C and 1250 °C, respectively. The solid lines represent the nominal compositions and standard error including the experimental error is also shown.

4.2.3. Microstructure and Analysis

The microstructure of the pellets sintered at both temperatures for different sintering times are shown in Fig. 4.13 and Fig. 4.14.. For t_s = 1200 °C, the microstructure shows no densification for up to 2 h, after which it starts to densify and exhibit significant grain growth. Nonetheless, all the microstructures show substantial porosity (Fig. 4.13). At 1250 °C, however, the microstructure exhibits only minor densification for 0 h, i.e. just by heating the sample to maximum temperature. For sintering times of more than 2 h, the microstructure shows increasing densification and, hence, a linear increase in relative density in this density range, as seen in Fig. 4.12. Furthermore, gradual grain growth is also observed with an increase in sintering time for all the samples.

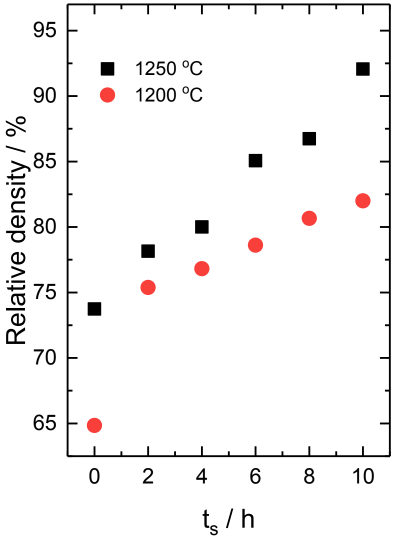

Fig. 4.12: The relative density of NZSP sintered at 1200 °C and 1250 °C measured by pycnometry.

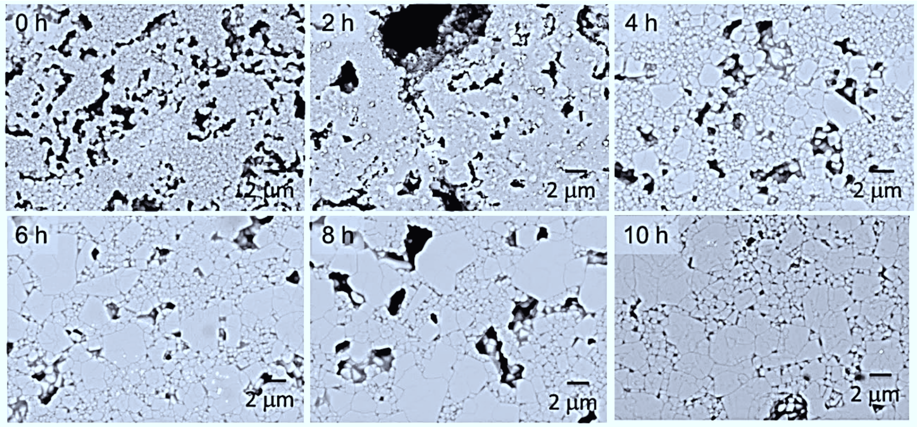

Fig. 4.13: SEM images of NZSP microstructure at different magnifications after sintering at 1200 ˚C for different dwell times.

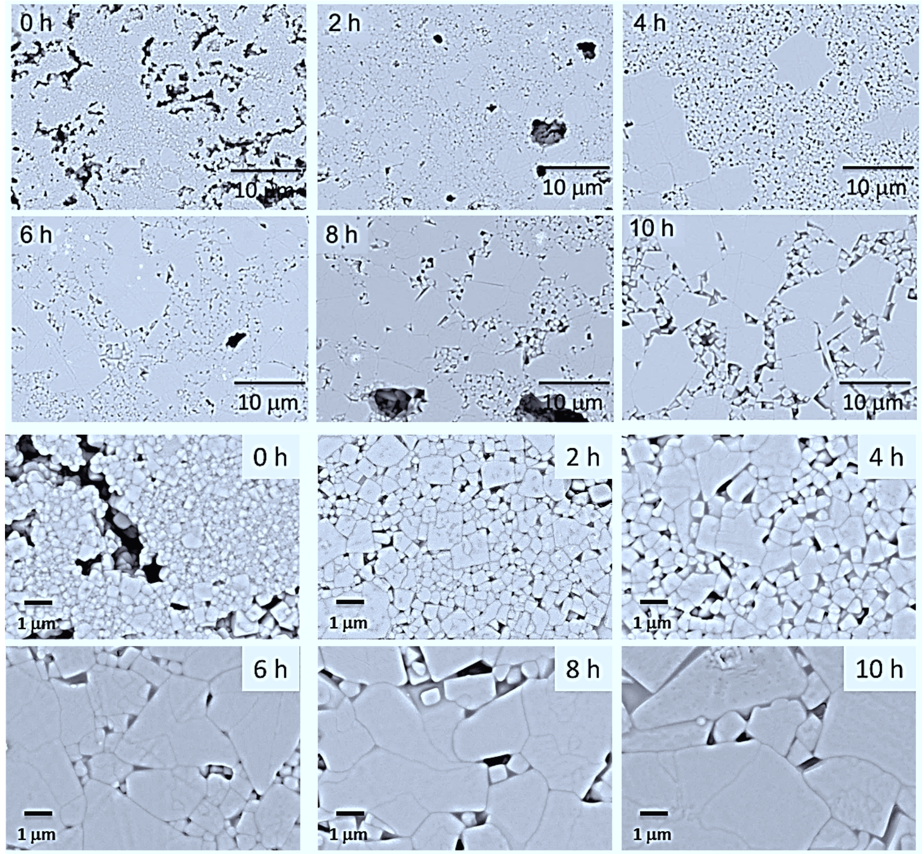

Fig. 4.14: Two sets of SEM images of NZSP microstructure with different magnifications after sintering at 1250 ˚C for various dwell times. The two magnifications reveal a broader view of grain growth in two different size regimes.

Examples of SEM images analyzed using the analySIS pro imaging software is shown in Fig. 4.15 where the color categories reflect the different grain size intervals, as explained in detail in section 3.6. The statistical data of microstructural parameters is given Table 4.4. The porosity obtained from image analysis is smaller than pycnometric values because image analysis is performed only on a localized area whilst not take into account the artifacts such as voids and cracks.

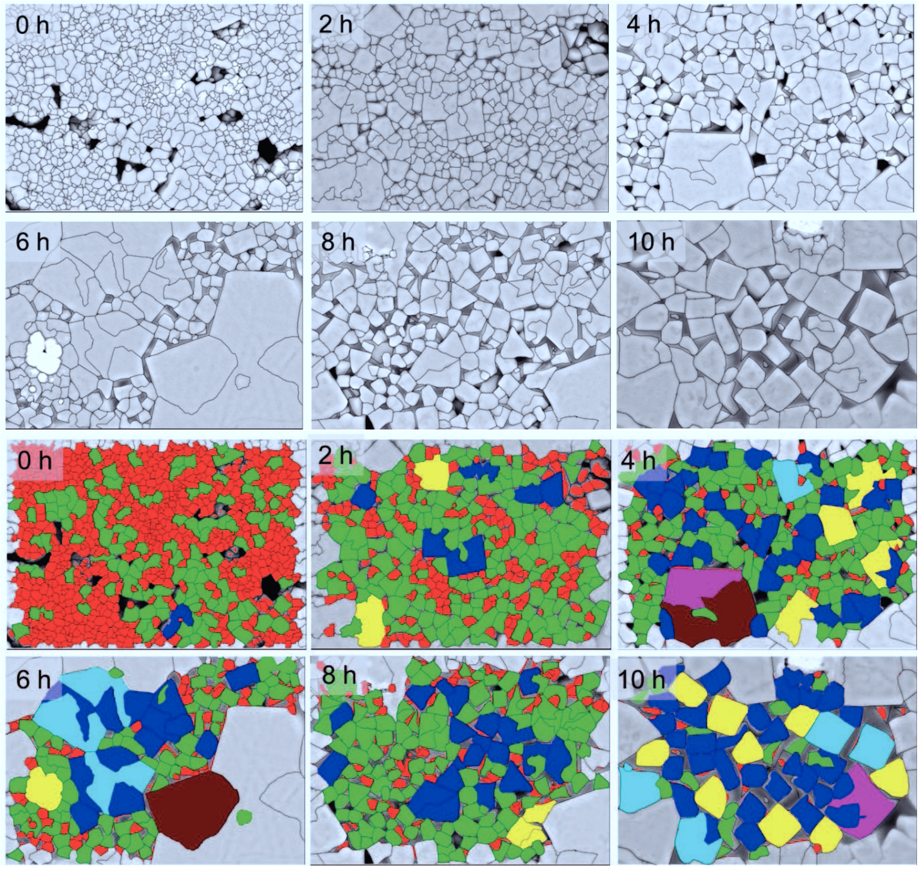

Fig. 4.15: Images of grain identification (upper two rows) and size statistics (lower two rows) using analySIS pro. The colors show different intervals of grain sizes.

Table 4.4: The area fractions of different phases obtained from image analysis on samples sintered at 1250 °C.

t_s	Diameter mean (small)	Diameter mean (large)	NASICON	Glassy	Pores	ZrO_2
h	µm		Area %			
0	0.645 ± 0.004	-	83.2 ± 1.5	1.7 ± 0.1	14.8 ± 1.5	0.1 ± 0.1
2	0.907 ± 0.008	-	92.7 ± 1.0	3.1 ± 0.3	3.6 ± 0.8	0.7 ± 0.4
4	1.032 ± 0.014	1.794 ± 0.060	91.9 ± 0.4	7.4 ± 0.3	0.8 ± 0.2	0.2 ± 0.0
6	1.139 ± 0.026	3.884 ± 0.173	92.0 ± 0.8	6.3 ± 0.6	1.0 ± 0.3	0.4 ± 0.1
8	1.319 ± 0.017	5.895 ± 0.173	92.4 ± 0.7	6.3 ± 0.6	1.0 ± 0.1	0.3 ± 0.1
10	1.763 ± 0.028	8.183 ± 0.047	91.1 ± 1.1	8.5 ± 1.0	0.4 ± 0.2	0.1 ± 0.1

The mean diameter is plotted as a function of relative density in Fig. 4.16a, revealing an abrupt increase of larger grains as compared to gradual increase of smaller grains. This abnormal grain growth can also be seen in Fig. 4.16b as a function of t_s. The possible reasons of such an abnormal grain growth are anisotropic grain boundary energy or high grain boundary mobility [175].

The grain size distributions indicate varying grain growth at different T_s and t_s. At 1200 °C and up to 4 h, the grains were smaller than the threshold of picture analysis (0.5 µm). For longer times and a higher temperature, however, a systematic change in grain size distributions was observed. Evidently, grain growth is observed in all samples through a shift in the frequency distribution peaks towards larger diameters. In addition, the formation of a right shoulder indicates that grain growth occurs at multiple speeds within the samples. This phenomenon of abnormal grain growth is visible more clearly at 1250 °C (Fig. 4.17b), where a mono-modal distribution at 0 h transforms into a bi-modal distribution curve at 10 h, in addition to an overall size increase of the initial grains (as seen in the SEM images). An abrupt increase in the grain size is observed after sintering at 1250 °C for more than 4 h in Fig. 4.17b, whilst for longer t_s the grains grow further in two different sizes. This phenomenon of abrupt change in grain size and grain boundaries as a function of time and temperature can be conjointly represented in a time–temperature–transition (TTT) diagram [176, 177]. However, this would require more experiments at different temperatures and dwell times in order to establish a complete TTT diagram for NASICONs.

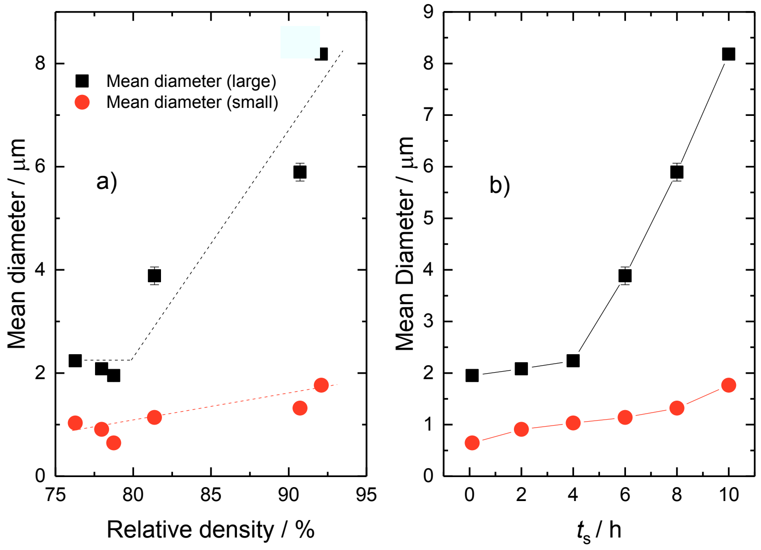

Fig. 4.16: a) Mean diameter as a function of relative density. b) Average grain size of initial and abruptly grown grains (only large grains were selected from Fig. 4.14). Both figures show data of samples sintered at 1250 °C.

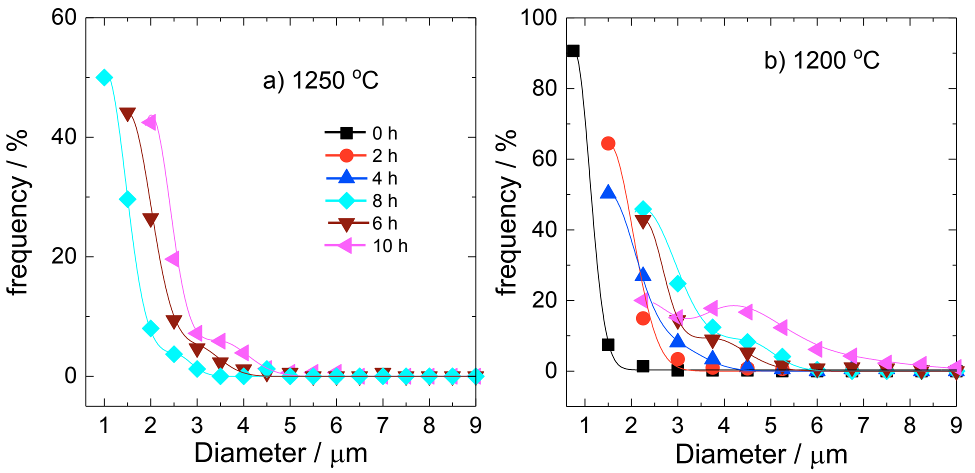

Fig. 4.17: The grain size distribution (normalized to the total number of particles) obtained from image analysis of specimens sintered at (a) 1200 °C and (b) 1250 °C. At 1200 °C, it was not possible to analyze the samples sintered for 0 h to 4 h due to their particle sizes being too small. For the particle diameters, a multiplication factor of 1.571 was applied for tetrakaidecahedron-shaped particles. The lines connecting the data points are drawn as a visual guide.

4.2.4. Electrical conductivity

The impedance spectra of samples sintered at both temperatures were measured from -30 to 100 °C, but only those obtained at -20 °C are shown in Fig. 4.18. For accurate comparison, the impedance data were normalized to the dimensions of the pellets.

Impedance spectra

The complex impedance plot of the samples sintered at 1200 °C and 1250 °C for different dwell times is shown in Fig. 4.18. the impedance spectra are normalized to the sample dimensions and thus allow a direct comparison of the spectra. The base material is the same for all samples ($Na_3Zr_2Si_2PO_{12}$), differing only in terms of sintering conditions. It can therefore be assumed that the bulk impedance of the samples should not differ much. However, the grain boundary impedance may differ substantially. This is a result of the increased densification and grain growth due to the higher sintering temperature and prolonged dwell time, respectively, resulting in turn in the alteration of the transport processes across grain boundaries. The sample sintered at 1250 °C for 10 h (Fig. 4.18b) has the lowest grain boundary resistance due to its larger grain sizes compared to the other samples.

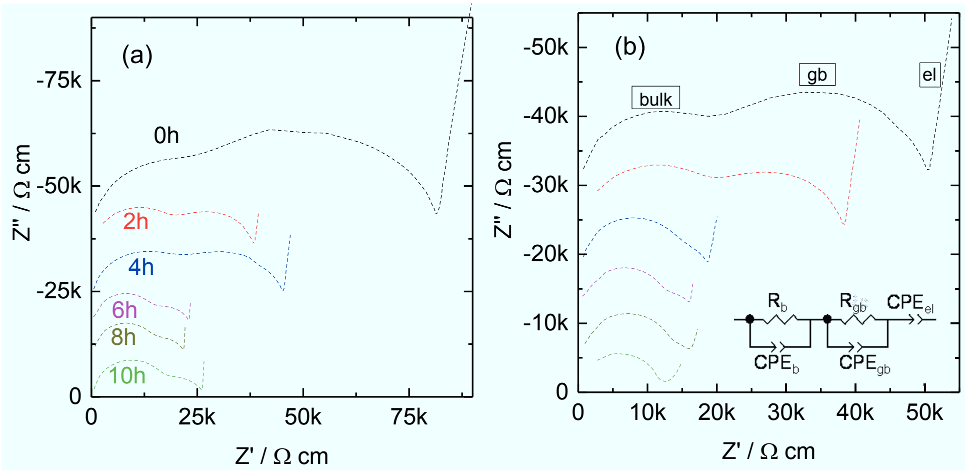

Fig. 4.18: Impedance spectra (at -20 °C) of NZSP sintered at (a) 1200 °C and (b) 1250 °C for different sintering times.

Electrical conductivity

The total conductivity as well as the conductivity of the bulk (σ_b) and grain boundaries (σ_{gb}) can be obtained by fitting the impedance spectra with an equivalent circuit (see Fig. 4.18). The description of the equivalent is already described in section 4.1.6. The obtained fitting data are given in Table 4.5. In the software used to analyze the impedance spectra (Zview®), the CPEs can be used to simulate the imperfect capacitance of transport processes. The impedance of the CPE element is calculated using Eq. 10 with ω as the frequency. The exponent *n* usually varies between 1 and 0.5. The C_{CPE} is related to the capacitance C as written in Eq. 11 [178].

$$Z_{CPE} = \frac{1}{C_{CPE}(j\omega)^n} \qquad \text{Eq. 10}$$

$$C = R^{\frac{1-n}{n}} C_{CPE}^{1/n} \qquad \text{Eq. 11}$$

When $n \rightarrow 1$ then $C_{CPE} \rightarrow C$ and an ideal capacitor is observed, whilst decreasing *n* indicates a non-ideal system, e.g. when $n = 0.5$ then a pure diffusion process is involved.

Table 4.5: Fitting data of impedance spectra at -20 °C shown in Fig. 4.7.

				T_s = 1200 °C					*Sum of Sq. error
t_s	R_b (Ω cm)	R_{gb} (Ω cm)	C_b (F)	n_b	C_{gb} (F)	n_{gb}	C_{el} (F)	n_{el}	
0h	$2.30 \cdot 10^4$	$5.82 \cdot 10^4$	$6.98 \cdot 10^{-11}$	0.95	$4.64 \cdot 10^{-10}$	0.85	$1.26 \cdot 10^{-6}$	0.89	0.13
2h	$1.94 \cdot 10^4$	$1.89 \cdot 10^4$	$7.00 \cdot 10^{-11}$	0.93	$1.64 \cdot 10^{-9}$	0.89	$2.74 \cdot 10^{-6}$	0.91	0.08
4h	$2.08 \cdot 10^4$	$2.41 \cdot 10^4$	$8.50 \cdot 10^{-11}$	0.95	$1.21 \cdot 10^{-9}$	0.89	$1.12 \cdot 10^{-6}$	0.90	0.06
6h	$1.53 \cdot 10^4$	$7.67 \cdot 10^3$	$8.53 \cdot 10^{-11}$	0.95	$3.66 \cdot 10^{-9}$	0.91	$9.43 \cdot 10^{-7}$	0.96	0.44
8h	$1.60 \cdot 10^4$	$5.65 \cdot 10^3$	$8.38 \cdot 10^{-11}$	0.93	$5.00 \cdot 10^{-9}$	0.95	$7.67 \cdot 10^{-7}$	0.96	0.56
10h	$1.74 \cdot 10^4$	$8.79 \cdot 10^3$	$8.10 \cdot 10^{-11}$	0.96	$3.68 \cdot 10^{-9}$	0.85	$6.47 \cdot 10^{-7}$	0.97	0.72
				T_s = 1250 °C					
0h	$1.94 \cdot 10^4$	$3.05 \cdot 10^4$	$8.08 \cdot 10^{-11}$	0.95	$1.26 \cdot 10^{-9}$	0.88	$1.82 \cdot 10^{-6}$	0.90	0.71
2h	$1.51 \cdot 10^4$	$4.29 \cdot 10^3$	$8.78 \cdot 10^{-11}$	0.90	$6.84 \cdot 10^{-9}$	0.99	$4.93 \cdot 10^{-7}$	0.97	0.68
4h	$1.62 \cdot 10^4$	$2.00 \cdot 10^3$	$9.27 \cdot 10^{-11}$	0.92	$1.23 \cdot 10^{-8}$	0.98	$8.06 \cdot 10^{-7}$	0.83	0.80
6h	$1.32 \cdot 10^4$	$2.80 \cdot 10^3$	$9.51 \cdot 10^{-11}$	0.93	$1.18 \cdot 10^{-8}$	0.98	$5.34 \cdot 10^{-7}$	0.93	0.58
8h	$1.42 \cdot 10^4$	$2.82 \cdot 10^3$	$7.98 \cdot 10^{-11}$	0.93	$1.20 \cdot 10^{-8}$	0.77	$3.54 \cdot 10^{-7}$	0.89	0.20
10h	$1.17 \cdot 10^4$	$2.68 \cdot 10^3$	$8.55 \cdot 10^{-11}$	0.96	$2.60 \cdot 10^{-8}$	0.78	$1.46 \cdot 10^{-7}$	0.87	0.07

Bulk and grain boundary conductivities can be extracted from the impedance spectra using the brick layer model [179, 180]. According to this model, the real grain boundary conductivity ($\sigma_{gb,real}$) is often wrongly reported in the literature. Whereas σ_b can be calculated with

$$\sigma_b = \frac{L}{AR_b} \qquad \text{Eq. 12}$$

and normalized to the sample dimensions, the analogue calculation of $\sigma_{gb,norm}$ using Eq. 13

$$\sigma_{gb,norm} = \frac{L}{AR_{gb}} \qquad \text{Eq. 13}$$

is often misinterpreted as the "real" $\sigma_{gb,real}$. This way of calculating σ_{gb} is not correct, because the actual volume fraction of grain boundaries is much smaller than the volume fraction of grains within the sample dimensions. Therefore the $\sigma_{gb,real}$ has to be calculated taking into account the net contribution of grain boundaries in the total conductivity. Therefore, the net grain boundary conductivity is calculated using Eq. 14 with the capacitance obtained from Eq. 2, R_{gb} is the grain boundary resistance, *L* is the thickness of sintered pellets and *A* the area of the electrodes.

$$\sigma_{gb,real} = \frac{L}{A}\left(\frac{C_b}{C_{gb}}\right)\frac{1}{R_{gb}} \qquad \text{Eq. 14}$$

The $\sigma_{gb,real}$ is obtained using the ratio of the capacitances of bulk and grain boundaries and represents the real conductivity of the grain boundaries. The ratio C_b/C_{gb} is nothing but the overall volume fraction of grain boundaries in the sample assuming that both bulk and grain boundaries have same dielectric constants [178].

The σ_b, $\sigma_{gb,real}$ and $\sigma_{gb,norm}$ are calculated using Eq. 12 and are shown in Fig. 4.19. σ_b (black lines) very slightly increases with increasing the sintering time due to the grain growth and improving crystallization resulting in less resistance to mobile charge carriers. The $\sigma_{gb,real}$ (red lines) is about one order of magnitude smaller than σ_b. It also does not change substantially after sintering at 1200 °C, however, for prolonged dwell time at 1250 °C it decreases significantly. This deviation is due the changes in transport properties at the grain boundaries. The chemistry changes arise from multiple processes like grain boundary diffusion and lattice diffusion triggered by the high temperature and long dwell time.

The $\sigma_{gb,norm}$ (blue line) is increasing with increasing the t_s for both temperatures. Even though $\sigma_{gb,norm}$ is conventionally regarded as σ_{gb}, any interpretation in terms of microstructure would be misleading because $\sigma_{gb,norm}$ is calculated by normalizing the R_{gb} to the whole sample dimensions and not to the grain boundary dimensions itself. Therefore, based on the higher values of $\sigma_{gb,norm}$, any conclusion that ionic transport is favorable and governed along grain boundaries would be a false conclusion. Nevertheless, it would be correct to compare R_{gb} in terms of microstructural changes since it represents the overall resistance induced by the grain boundaries to Na^+ conduction. For instance, in Fig. 4.18, at first glimpse it appears that the grain boundary resistivity is lower than that of the bulk, particularly for samples sintered for 8 or 10 h. Closer examination of these materials, however, reveals that the samples have larger grains (see Fig. 4.14), and exhibit a lower grain boundary resistance simply because fewer boundaries are encountered by the mobile charge carriers. These results are coherent with proton-conducting $BaCe_{0.85}Gd_{0.15}O_{2.975}$ where a reduction in R_{gb} was also reported by increasing the grain size [178].

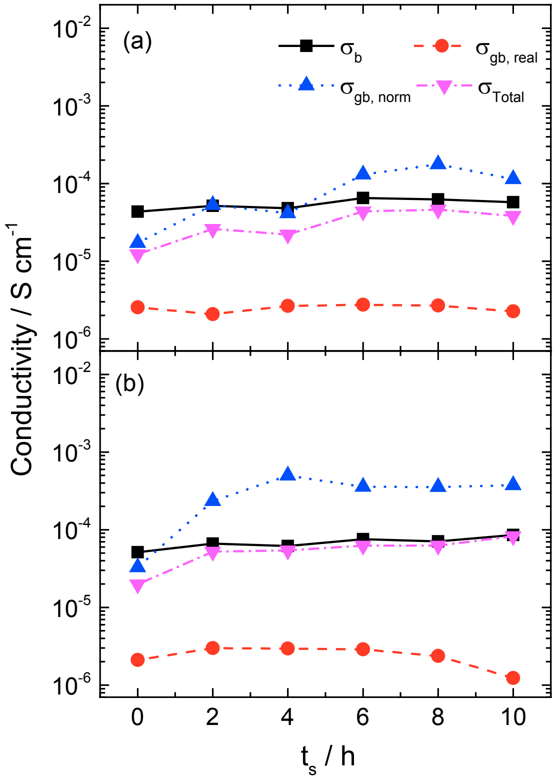

Fig. 4.19: The conductivity contributions in dependence of dwell time after sintering at (a) 1200 °C and (b) 1250 °C. The measurements were performed at -20 °C.

A correlation between conductivity and density is shown in Fig. 4.20 including data of previous studies. The conductivity increases nearly an order of magnitude by increasing the relative density from 65 % to 93 %, which signifies the importance of sintering conditions in ceramic technology. For simulating the transport properties of multi-phase materials, the generalized effective media theory (GEM) [181] is often applied. However, this model has been developed only for composites with specific microstructures, is very valuable for cermets and semiconducting ceramics, but do not take into account detailed microstructural features like grains sizes, grain anisotropies or orientations. Therefore it is not surprising, that the GEM curve in Fig. 4.20 do not fit very well to the data. The used formula

$$\sigma = \sigma_{ic}^{0}\left(1 - \frac{V_p + V_{ZrO2}}{V_{iso,c}}\right)^{n} \qquad \text{Eq. 15}$$

(with σ_{ic}^{0} is the specific conductivity of the ionic conductor, V_p and V_{ZrO_2} the volume fraction of pores and zirconia, respectively, $V_{iso,c}$ the critical volume fraction of isolating phases, where the first percolation pathways are formed by the ionic conductor, and n is an empirical exponent) do not include the grain boundary contributions. Therefore several models have been developed for solid electrolytes in combination with the brick-layer model [182, 183]. In its simplest form, the GEM formula can be expanded by taking into account the volume of grain boundaries and the grain boundary conductivity. Since C_b/C_{gb} is regarded as the volume fraction of grain boundaries, which, as listed in Table 4.5, depends on the densification of the samples and the grain boundary conductivity can be assumed as constant ($\sigma_{gb,real} = 2 - 4 \cdot 10^{-6}$ S/cm^{-1}, see Fig. 4.19), the GEM formula can be extended with the rule of mixtures to

$$\sigma = \left(\sigma_{ic}^{0}\left(1 - V_{iso} - V_{gb}\right) + V_{gb}\sigma_{gb}\right)\left(1 - \frac{V_{iso}}{V_{iso,c}}\right)^{n} \qquad \text{Eq. 16}$$

with $V_{iso} = V_p + V_{ZrO2}$ and using an exponential decay to fit the dependence of grain boundary volume fraction on density according to

$$V_{gb} = C_b/C_{gb} = 96.93\, e^{(-V_{ic}/0.10364)} - 0.0134 \qquad \text{Eq. 17}$$

The resulting curve agrees much better with the observed data (dashed line in Fig. 4.20).

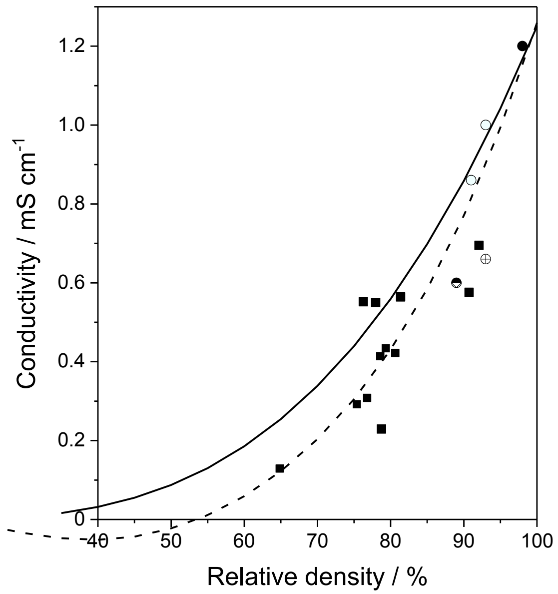

Fig. 4.20: Correlation of relative density and total conductivity of NZSP samples (filled squares). The conductivity measurements were performed at room temperature (25 °C). Additional data were taken from refs. [29] (half-filled circle), [152] (crossed circle), [122] (open circles), [162] (filled circle). The GEM curve (Eq. 15, solid line) and modified GEM curve (Eq. 17, dashed line) was calculated with $\boldsymbol{\sigma}_{\mathbf{ic}}^{\mathbf{0}}$ = 1.25 mS cm^{-1}, $V_{iso,c}$ = 0.85 and n = 3.

Activation energies

The total conductivity (σ_{total}) was calculated from the sum of R_b and R_{gb} of the samples and is plotted as a function of inverse temperature in Fig. 4.21. σ_{total} follows an Arrhenius law and the activation energies (Table 4.6) were calculated from the slope of the straight line in a $\ln(\sigma \cdot T)$ vs. 1/T plot.

After sintering at 1250 °C, all lines overlap at room temperature, except for 0 h, indicating no significant difference in σ_{total}. The activation energy (E_a) decreases with increasing sintering time and agrees with the observed grain growth in the microstructure. The change in slope of the lines indicates a variation in the ionic conduction mechanism across the grain boundaries. The lower activation energy for longer sintering times indicates that the increase in grain size reduces the amount of grain boundaries and the R_{gb}. Therefore, the resistance of Na^+ hopping decreases as the ions incur reduced grain boundaries due to grain growth at longer sintering times (Fig. 2 and section 3.1). For a better understanding of the process, grain and grain boundary conductivities are plotted separately in Fig. 4.22.

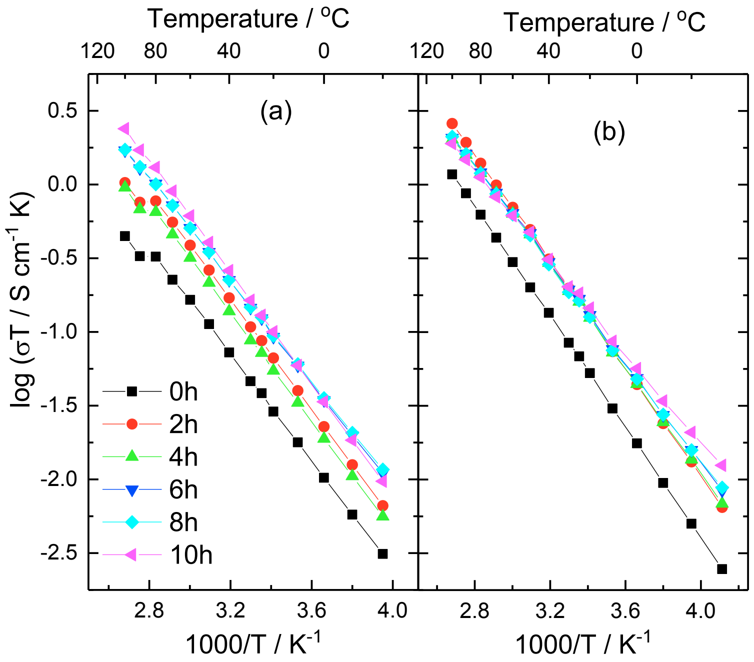

Fig. 4.21: Arrhenius-type plot of total conductivity of NZSiP sintered at (a) 1200 °C and (b) 1250 °C applying different sintering times.

In Fig. 4.21a, the conductivity slightly deviates from the Arrhenius behavior at temperatures ~ 90 °C. This is not observed in case of samples sintered at 1250 °C. It is assumed that this phenomenon is due to absorption of water molecules in the samples with higher porosity which are desorbed at higher temperature causing this deviation.

Table 4.6: The E_a of σ_{total} derived from a $\ln(\sigma_T)$ vs. 1/T plot according to Fig. 4.21.

t_s / h	T_s = 1200 °C	T_s = 1250 °C
0	0.339 ± 0.006	0.372 ± 0.001
2	0.350 ± 0.006	0.361 ± 0.001
4	0.349 ± 0.005	0.345 ± 0.003
6	0.335 ± 0.005	0.334 ± 0.002
8	0.331 ± 0.006	0.333 ± 0.002
10	0.374 ± 0.001	0.307 ± 0.002

Two semicircles were only observed up to 0 °C and 10 °C for samples sintered at 1200 °C and 1250 °C, respectively. Both the $\sigma_{gb,norm}$ and $\sigma_{gb,real}$ are calculated using Eq. 13 and Eq. 14. It is important to remark that at 0 °C, obtaining $\sigma_{gb,real}$ becomes unreliable for 1250 °C sintered samples when $t_s > 6$ h, due to very low n values (< 0.5; Eq. 11). However for 1200 °C sintered samples even for longer t_s the n values are > 0.9 and the calculations were reasonable since the $\sigma_{gb,real}$ calculation assumes that the dielectric coefficient of grain boundaries remain equal to the bulk and effects only the magnitude of the conductivity. Therefore, the E_a values obtained from an Arrhenius plot of $\sigma_{gb,norm}$ are used even though the magnitude of the conductivity is incorrect. It also illustrates why $\sigma_{gb,norm}$ is widely adopted as $\sigma_{gb,real}$, given that $\sigma_{gb,real}$ calculation is possible only for materials and at temperatures where grain boundary resistance contributes significantly to the total resistance.

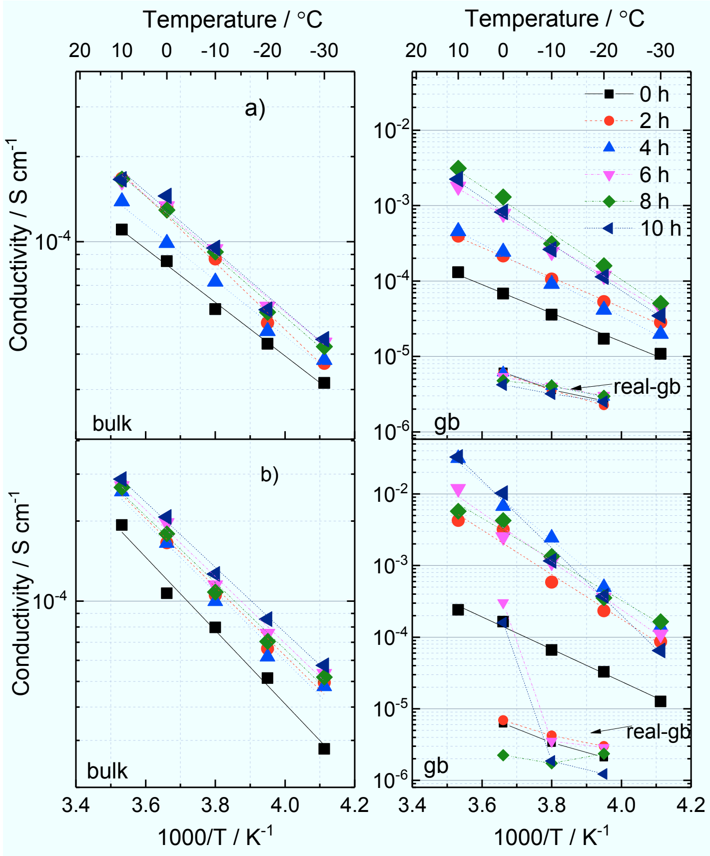

Fig. 4.22: Arrhenius-type plots of σ_b and σ_{gb} as well as $\sigma_{gb,real}$ obtained in the temperature range -20 to 10 °C of samples sintered at (a) 1200 °C and (b) 1250 °C.

The obtained activation energies of each process are shown in Fig. 4.23. The values of $E_{a,b}$ are nearly constant for the two different sintering temperatures, varying between 0.21 and 0.28 eV. However, the $E_{a,gb}$ values are significantly increasing with dwell time. After sintering at 1200 °C $E_{a,gb}$ systematically increases from 0.35 to 0.59 eV, which indicates a systematic alteration of the transport properties at the grain boundaries, which are affected only by the dwell time. The grain growth and small changes in stoichiometry due to evaporation of sodium oxide could be the only processes happening during sintering. However, after sintering at higher temperature (1250 °C), the $E_{a,gb}$ follows an irregular trend showing fluctuating transport properties across the grain boundaries by increasing the dwell time with an overall increase from 0.42 to 0.97 eV. The non-uniform $E_{a,gb}$ trend is an indication that multiple processes are affecting the grain boundary chemistry. These processes, in addition to obvious grain growth starting at t_s = 4 h and presumably reducing the activation energy, could be a simultaneous increase of the glassy phase. Since the amount of this phase is substantially increasing from t_s = 8 h to t_s = 10 h, it is likely that the increasing volume fraction of this phase might be associated with the strong increase of $E_{a,gb}$. This is confirmed by a correlation between the glassy-phase obtained from image analysis and $E_{a,\,gb}$, both giving similar trends as shown by dotted line connecting the steric symbols in Fig. 4.23b. It can be noticed, however, that despite fluctuations in $E_{a,gb}$ values they only have a minor impact on the total conductivity (Fig. 4.22) and its activation energy (Table 4.6).

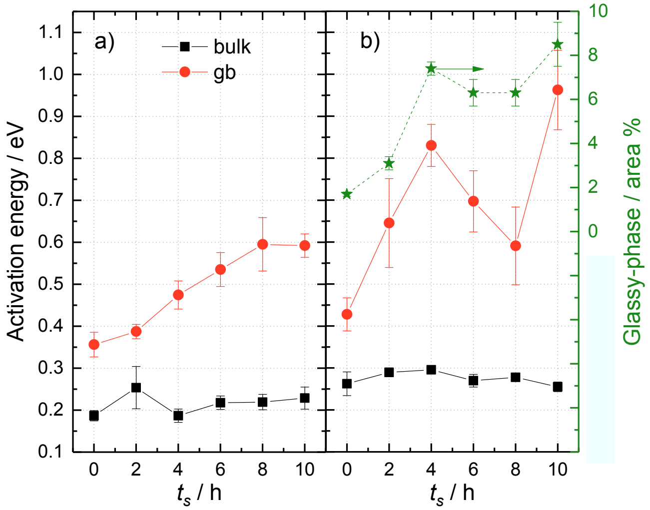

Fig. 4.23: Activation energies of bulk and grain boundary conductivity of samples sintered at (a) 1200 °C and (b) 1250 °C. The Ea's are obtained from Arrhenius equation according to Fig. 4.21. A correlation with the percentage of glass phase is also included from Table 4.4.

Correlations

The E_a of the total conductivity is correlated with relative densities, conductivity and sintering time in Fig. 4.24. All three parameters are inter-dependent, i.e. $\rho_{rel} \propto \sigma_{Total} \propto t_s$. Fig. 4.24 shows that apart from one sample (1200 °C, 0 h), the E_a has a decreasing trend with the correlated parameters. The exceptional sample has a ρ_{rel} of 65 % that is close to the green density of the pellets after pressing (59 – 61 %) and therefore densification has hardly started at the given sintering conditions. This leads to an argument that in all samples that have undergone densification (ρ_{rel} > 80%) in the sintering process behave in a similar way in terms of the E_a of total conductivity.

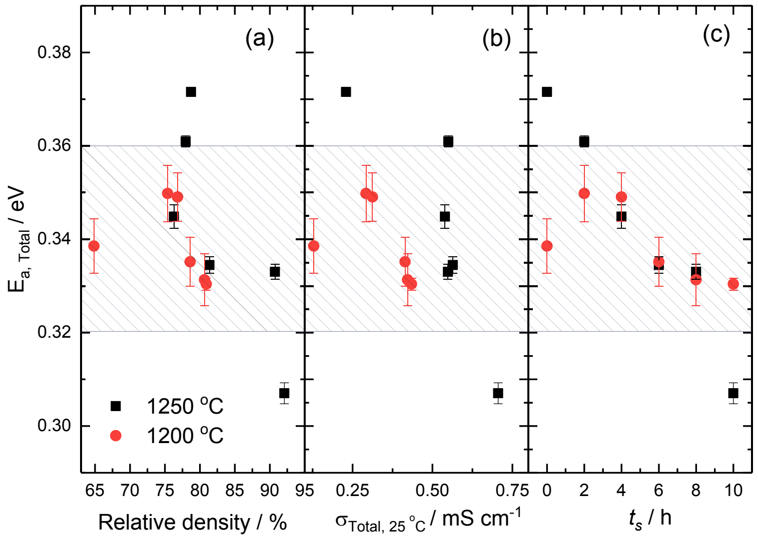

Fig. 4.24: Correlation of activation energy with (a) relative density, (b) total conductivity and (c) sintering time. The shaded region shows E_a values which are in close agreement with [184, 185].

In a previous work, Fuentes et al. [186] conducted a similar study on a different NASICON material ($Na_3Y_{0.12}Zr_{1.88}Si_2PO_{12}$) and found that the impact of sintering temperature (T_s) was negligible on the E_a values. However, by increasing the sintering time (t_s), they observed a decreasing E_a, which is in agreement with our study. Their sample sintered at 1220 °C for 80 h had an E_a of 0.26 eV, which is similar to the E_a of bulk conductivity of NZSiP. Assuming a negligible impact of the Y substitution, this evidence can be used to support the argument that prolonged sintering (t_s = 80 h) would result in large grain growth and decreasing grain boundary resistance. For the extreme situations of t_s this leads to the limits

$$\lim_{t_s \to 0} E_a \to E_{a,gb} \quad and \quad \sigma \to \sigma_{gb}$$

$$\lim_{t_s \to \infty} E_a \to E_{a,b} \quad and \quad \sigma \to \sigma_b$$

4.3. The effect of Na-excess on NASICON

4.3.1. Motivation

It has been reported that after sintering above 1200 ºC, NZSiP suffers from sodium oxide loss that diminishes the charge carrier concentration in the material and consequently reduces its ionic conductivity (σ_{ion}) [187-189]. This can be avoided by two potential strategies. The first rather complicated strategy is by upgrading the experimental apparatus and the other is by controlling the chemistry. The experimental setup can be designed in which sample is encapsulated in a closed system in order to minimize the sodium oxide loss, as practiced for many ceramics (powder-bed method). The second strategy is to control the chemistry by synthesizing NZSiP with an excess of sodium. The excess amount of sodium would compensate the loss during sintering process.

In this work, the second approach of improving σ_{ion} was followed by investigating the impact of an excess of sodium in NZSiP$_x$. The x was chosen as 0, 0.05, 0.1, 0.2, 0.3 and 0.4. Results of this study will be useful for optimizing sodium loss during the sintering of tape-cast sheets. Additionally, it will also help understanding the impact of excess charge carriers on the conduction properties of the material.

4.3.2. Particle size distribution

All compositions in NZSiP$_x$ were synthesized by SA-SSR method (section 3.1.2). After calcination, all powders were milled and the particle size distribution of milled powders is shown in the Fig. 4.25. All the powders have a similar d_{10} and d_{50} whereas the d_{90} has a relatively wider scatter. Furthermore, the PSD of all powders is similar therefore any differences in the sintering process would not be due to the different sizes of initially pressed powders. The PSD of $x = 0$ is already given in section 4.1.4.

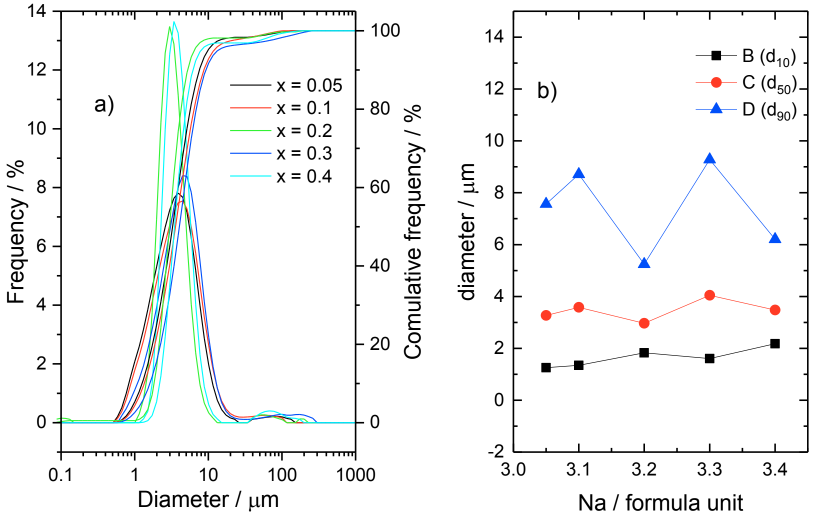

Fig. 4.25 a) The PSD of milled NZSiP$_x$ powders. b) Their characteristic diameters, i.e. d_{10}, d_{50} and d_{90}.

4.3.3. Two-step sintering

In a typical dilatometry curve, densification is rather a rapid phenomenon and occurs promptly before grain growth starts. To utilize this phenomenon, samples were first exposed to a high temperature for a short time (where densification occurs), which is followed by dwelling them at reduced-temperature for elongated time (where growth occurs). By using this sintering procedure we not only reduce the cost of operation but it also lowers the sodium loss because the sample remains at high temperature for only short time. The sintering route has already been used in the past [190-192].

NZSiP$_x$ was sintered by a two-step sintering method and the conditions were optimized after several trials. The resulting densities of the different trials are shown in the Fig. 4.26. The best conditions were: 1250 °C, 30 min → 1230 °C for 5 h that resulted in the relative density of ≥ 90 % for all compositions. Therefore, this heat treatment sequence was applied to sinter all samples for further investigations.

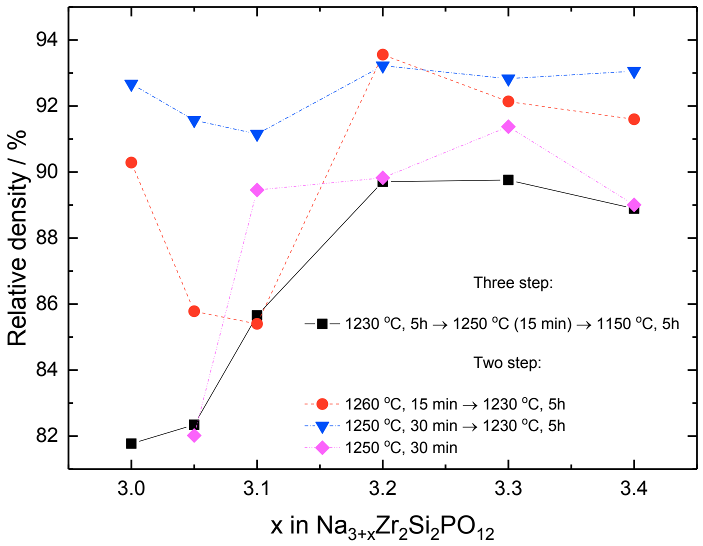

Fig. 4.26: The densities obtained after sintering at different step sintering conditions.

This sequence of heat treatment steps must be followed to obtain high densification: first step of sintering should done at higher temperature (for short time), followed by sintering at lower temperatures (longer duration). The reverse sequence would result in very different results, as witnessed in the three step sintering trail in Fig. 4.26.

4.3.4. Elemental analysis

All compositions in the series NZSiP$_x$ were chemically analyzed to obtain their accurate stoichiometry. Sodium content was found to be lower than anticipated, which is due to the hygroscopic nature of sodium source compound and sodium oxide loss during sintering. The results are also shown in Fig. 4.27a. The Zr content lies within the error limits of the measurement, whereas a systematic Si deficiency is arising from the source material (TEOS).

Table 4.7: Nominal and analytical stoichiometry of sintered and crushed NZSiP$_x$.

Nominal	**Analytical (ICP-OES)**
$Na_{3.00}Zr_2Si_2PO_{12}$	$Na_{2.72}Zr_{2.06}Si_{1.97}PO_{12}$
$Na_{3.05}Zr_2Si_2PO_{12}$	$Na_{2.90}Zr_{2.00}Si_{1.83}PO_{12}$
$Na_{3.1}Zr_2Si_2PO_{12}$	$Na_{2.93}Zr_{1.99}Si_{1.81}PO_{12}$
$Na_{3.2}Zr_2Si_2PO_{12}$	$Na_{3.11}Zr_{2.01}Si_{1.84}PO_{12}$
$Na_{3.3}Zr_2Si_2PO_{12}$	$Na_{3.12}Zr_{2.00}Si_{1.84}PO_{12}$
$Na_{3.4}Zr_2Si_2PO_{12}$	$Na_{3.22}Zr_{1.94}Si_{1.68}PO_{12}$

The sodium content was further studied before milling and after sintering and the results are shown in the Fig. 4.27b. It is revealed that Na content is lower than the anticipated nominal values in all cases. This systematic Na deficit is clearly because of the inaccurate starting calculation of sodium source ($NaNO_3$) and variation arise due to the hygroscopic nature of $NaNO_3$ [193]. In addition, a sodium loss during sintering process can also be seen. The sodium loss was negligible in case of NZSiP$_{0.2}$ sample.

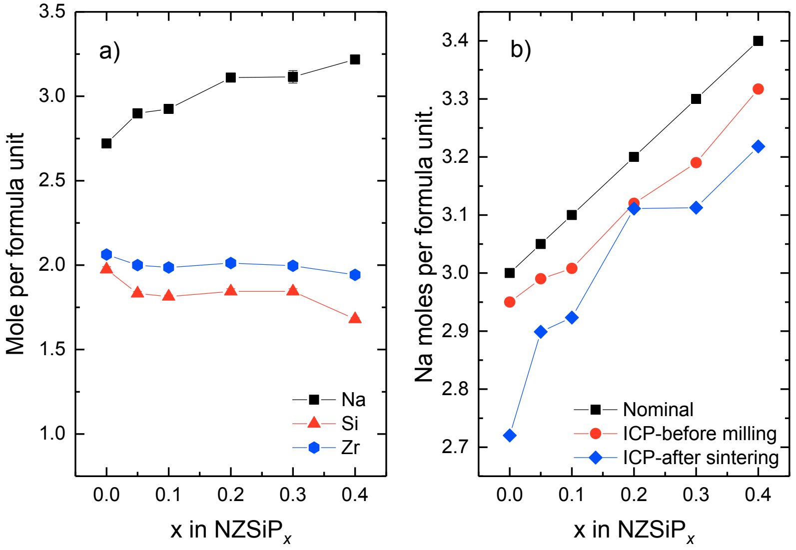

Fig. 4.27: The analytical stoichiometries of a) Na, Si and Zr in sintered NZSiP$_x$ and b) the deviation of Na content before milling and after sintering. For better comparison, the results before milling and after sintering were normalized to Si and P, respectively. The sintering conditions were 1250 °C, 30 min → 1230 °C for 5 h.

4.3.5. X-ray diffraction

The XRD of the sintered samples of NZSiP$_x$ is shown in Fig. 4.28 between 2θ values of 10 – 40°. All the compositions in the range $0 \leq x \leq 0.4$ crystallized in the desired monoclinic C2/c NASICON structure. All contained varying amounts of ZrO_2 as secondary phase, as depicted by blue vertical lines. The secondary phase content in all compositions was less than 2 wt. %.

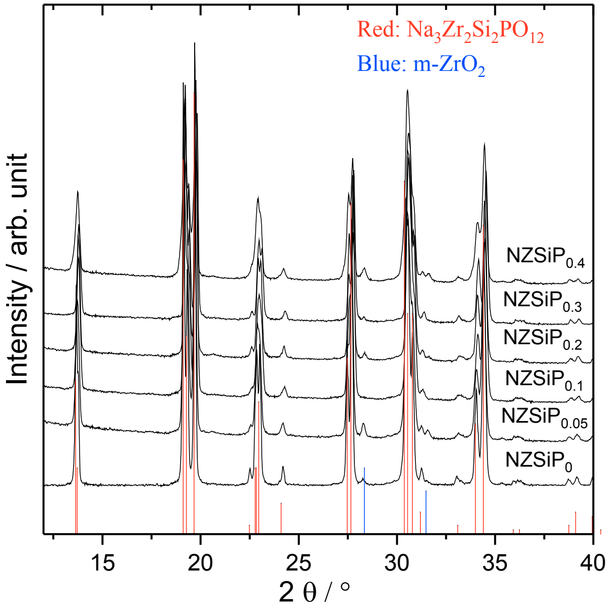

Fig. 4.28: The XRD patterns for the $NZSiP_x$ system at room temperature. The monoclinic ZrO_2 [167] and NZSiP [166] are taken from literature.

The unit cell parameters of all compositions obtained by Rietveld refinement are given in Table 4.8. The results obtained in this study are comparable to reported values [194].

Table 4.8: The unit cell parameters of $NZSiP_x$.

$NZSiP_x$	**a (Å)**	**b (Å)**	**c (Å)**	**β (⁰)**	**ZrO_2**
0	15.63(2)	9.01(1)	9.21(1)	123.70(6)	< 1 %
0.05	15.64(2)	9.05(1)	9.22(1)	123.75(6)	2 %
0.1	15.62(2)	9.04(1)	9.21(1)	123.72(6)	0 %
0.2	15.64(1)	9.05 (1)	9.22(1)	123.75(6)	< 1 %
0.3	15.61(1)	9.03(1)	9.21(1)	123.61(6)	< 1 %
0.4	15.61(2)	9.03(1)	9.20(1)	123.68(6)	3 %

4.3.6. Thermal analysis

The DTA/TG results of $NZSiP_x$ are shown in Fig. 4.29. The TG results show following events:

- a loss of carbon and water until 400 °C (confirmed through DTA Fig. 4.29b)

- no weight loss is observed upon further heating until 1250 °C, and
- after a dwell time of 6.5 h, a sodium loss was observed. The % wt. loss was highest for $NZSiP_{0.05}$ sample, (i.e., 1.5 %), and this composition had the highest glass phase content as seen in the microstructure (Fig. 4.30).

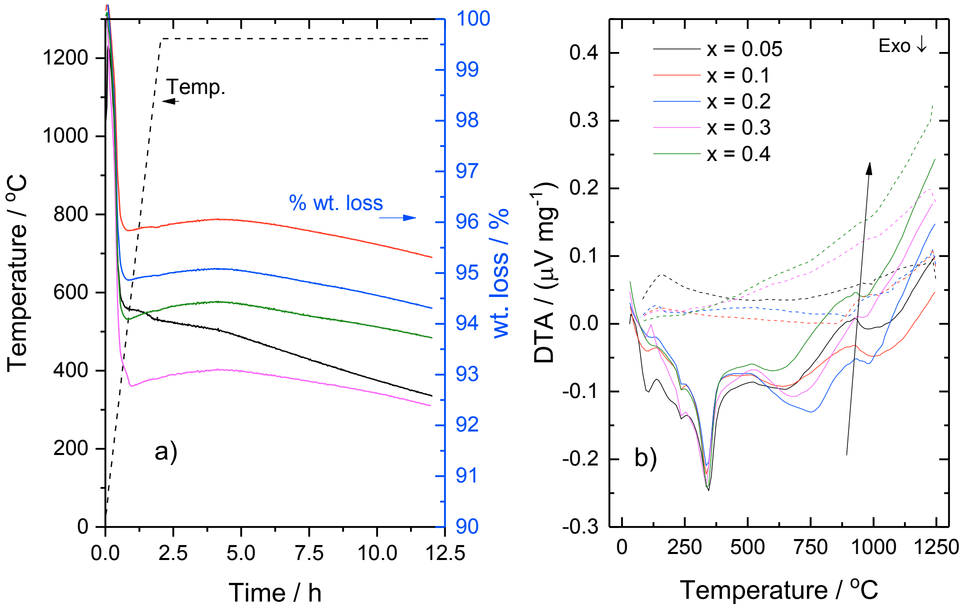

Fig. 4.29: Thermal analysis showing a) the TGA curves of $NZSiP_x$ indicating a sodium loss during the dwell time more than 6.5 h. b) The DSC curves of $NZSiP_x$, indicating a liquid phase formation in all samples during heating (solid lines) and its solidification during cooling (dashed lines) between 900 – 970 °C.

To conclude from TG results it is clear that in order to avoid the Na loss during sintering at 1250 °C, the dwell time should be less than 6.5 h. The other option to achieve stoichiometric compositions as well as keeping them for longer duration at higher temperature is to start with Na-access of 0.9 wt. %. This excess of sodium is to compensate its loss during the dwell time.

In the DTA curves, another interesting observation is the small hump between 900 – 1000 °C. This hump appears during both heating as well as the cooling of samples. This is a clear indication of liquid phase formation during heating that solidifies during cooling. Two mechanisms are possible for the formation of the liquid phase. The first is based on the lowest liquidus point in the phase diagram of Na_2O-SiO_2-P_2O_5 [195]. According to this work, a liquid phase can be formed at around 840 °C. The second mechanism is the melting of NASICON solid solution, which has a different composition than the original NASICON composition but it still lies on the liquidus line of the Na_2O-SiO_2-P_2O_5 phase diagram. In both cases, the liquid phase is likely to become a glassy phase during rapid cooling because the liquid is rich in glass-forming oxides such as silica and phosphorous oxides. The formation glassy is in agreement with other studies [185, 196-199].

4.3.7. Microstructure

The microstructure of $NZSiP_x$ obtained from scanning electron microscope is shown in Fig. 4.30. All compositions have similar grain growth similar to what was already seen in section 4.2. The secondary phase (ZrO_2) can also be seen, particularly in $NZSiP_{0.05}$ it exists in different morphologies such as cubic and monoclinic. The secondary phase is formed at the inter-granular regions or so called grain boundaries. The EDX analyses of these grain boundaries (not shown here) confirmed that these regions are Zr deficient and Si rich. This is another evidence of the formation of a glassy phase as already discussed in the previous chapter. It is also reported already in by others [197-199]. This glassy phase is present only at the grain boundary where it promotes the sinterability of NASICON. Nonetheless it has a larger resistance than NASICON and acts as an electrical barrier towards Na^+ conduction.

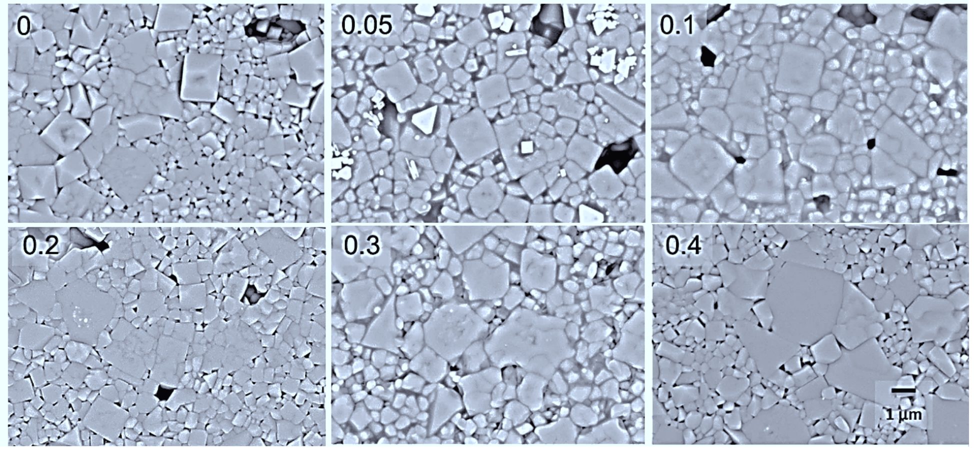

Fig. 4.30: The microstructure of $NZSiP_x$ obtained on thermally etched samples at 1150 °C for 0.25 h.

4.3.8. Electrical conductivity

The Nyquist plots of NZSiP$_x$ are shown in Fig. 4.31. All compositions with $0 \leq x \leq 0.4$, only show one semicircle at 25 °C that is starting not from zero-resistance. This indicates that both bulk and grain boundary contribute to the total resistance. The figure also indicates that the conductivity of the material is substantially influenced by the different sodium contents and NZSiP$_{0.2}$ has the highest bulk conductivity. This composition also had minimum glass phase formation as observed from the microstructure.

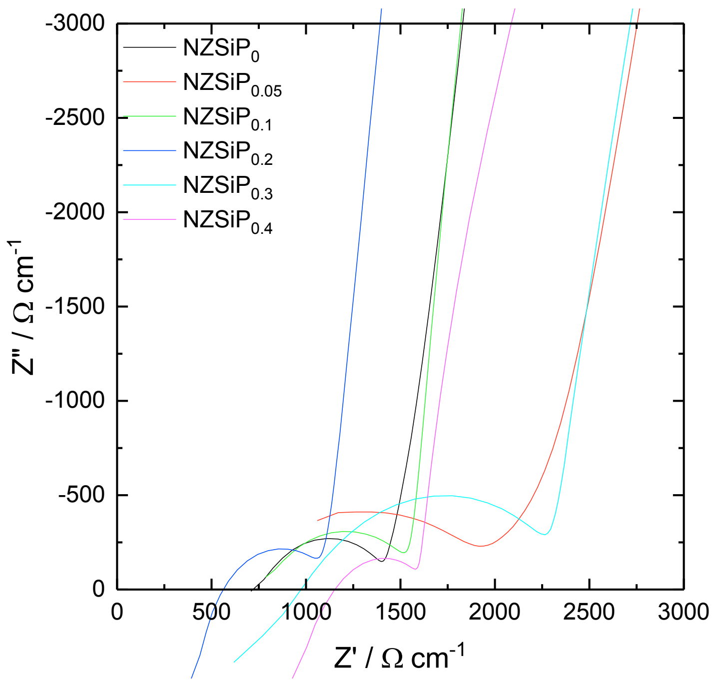

Fig. 4.31: Impedance spectra obtained at 25 °C for NZSiP$_x$ sintered at 1250 °C, 0.5 h and then 1230 °C for 5 h.

The Arrhenius plot of the σ_{Total} in the temperature range -30 – 100 °C is shown in Fig. 4.32 along with the activation energies. The figure shows that the lines have different slopes indicating that they have different E_a values. The conductivity is highest in NZSiP$_{0.2}$.

The E_a, when plotted against of Na content, a clear decreasing trend with an exception of NZSiP$_0$. Nevertheless, the whole range of activation energy of NZSiP$_x$ is within the reported range of E_a for NZSiP in section 4.2.4 and in [184, 185].

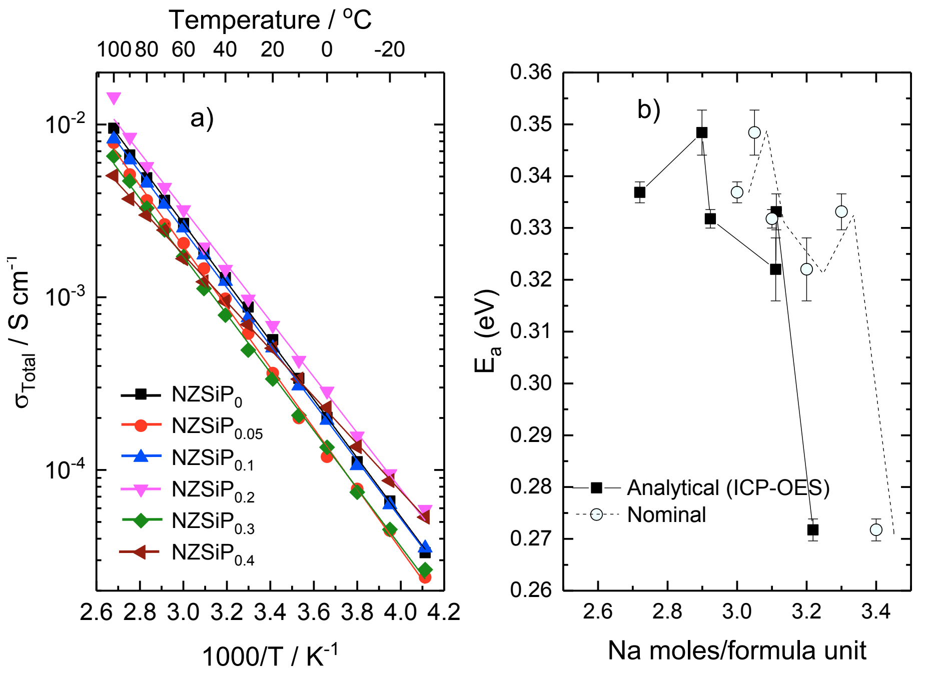

Fig. 4.32 a) The Arrhenius plot σ_{Total} obtained from impedance spectroscopy in the temperature range -30 – 100 °C and b) the E_a as a function of nominal and analytical composition.

The bulk and grain boundary contribution in the σ_{Total} was separated using an equivalent circuit. It was only possible to do it between -30 and 30 °C (Fig. 4.33), like previously performed in section 4.1and section 4.2. The slope of $E_{a,\ bulk}$ is varying whereas the position of σ_{bulk} is highest for NZSiP$_{0.2}$ with an analytical composition is $Na_{3.11}Zr_{2.01}Si_{1.84}P_1O_{12}$. This indicates that the σ_{bulk} of NZSiP$_{0.2}$ is highest, as previously seen in the total conductivities as well. On the other hand, the $\sigma_{gb,\ norm}$ have similar slopes and they follow an irregular trend.

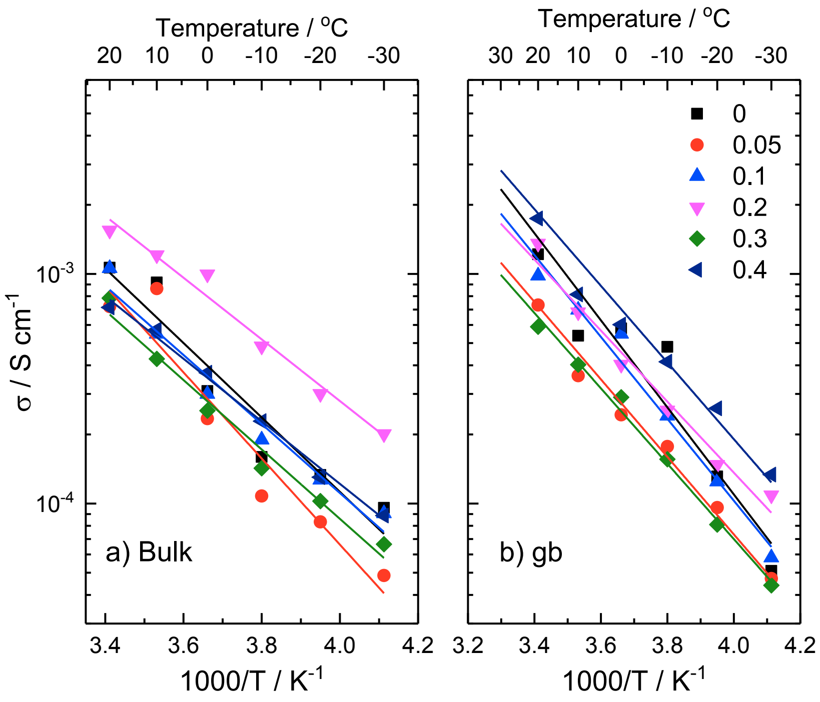

Fig. 4.33: The Arrhenius plot of σ_{bulk} and $\sigma_{gb,\ norm}$ after fitting the equivalent circuit to the impedance data in the range of 20 to -30 °C. The lines are linear fits of the data. The R-square of fit in all cases is above 95, except for grain boundaries, when x is 0 and 0.05, where it was 90.

The σ_{bulk} obtained from Fig. 4.33 is plotted as a function of *x* in Fig. 4.34. The figure shows that the maximum σ_{bulk} was observed when the Na excess in the formula unit was 0.2 moles i.e. NZSiP$_{0.2}$. This is the composition where the sodium loss after sintering was very low. Furthermore, when plotted against analytical stoichiometry, a similar trend is observed with highest σ_{bulk} for NZSiP$_{0.2}$.

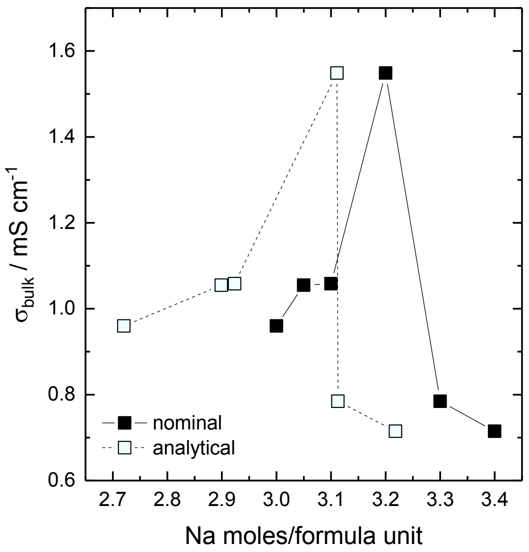

Fig. 4.34: The bulk conductivity as a function of nominal and analytical Na per formula unit in $NZSiP_x$ at 25 ºC. The line is drawn to guide the eye.

The E_a of $\sigma_{gb,\ norm}$ and σ_{bulk} are plotted against the nominal and analytical stoichiometry in Fig. 4.35. In case of nominal composition, since the Na excess here is not a true representation, the values show an irregular trend with an increasing Na amount. However, if E_a is plotted against the analytical stoichiometries, a clear negative slope is observed. On the other hand, the $E_{a,\ gb}$ behaves in an irregular manner with increasing the Na content.

.

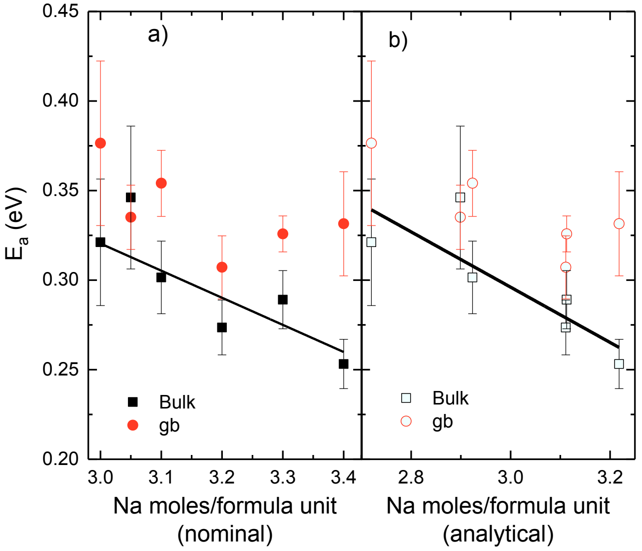

Fig. 4.35: The E_a of σ_{gb} and σ_{bulk} as a function of a) nominal and b) analytical Na moles per formula unit of $NZSiP_x$.

In a typical NASICON type NZSiP with monoclinic structure, the site occupancy of Na is 75 % and there are four missing Na sites in the 4 formula units. These sites are Na(1), Na(2) and Na(3) as already discussed in section 2.2.5. To obtain high conductivity, the ratio of charge carriers occupying the Na sites and the Na vacancies has to be optimum. Too high site occupancy would leave no available vacancies for ion hopping and would result in increasing the E_a of ion movement, and vice versa. The Na(1) sites are thermodynamically more stable than other two therefore it is likely that these sites will be completely filled with the Na atoms. This ratio is, as discussed earlier, 3.4 moles of Na per formula unit. Once Na(1) sites are filled, the remaining Na atoms are then randomly distributed over the available Na(2) and Na(3) sites [166]. The sodium conduction occurs in two pathways i.e., Na(1) – Na(2) and Na(1) – Na(3). Based on DFT computations in [194], the authors came to a conclusion that Na-excess in a monoclinic NZSiP structure increases the bottleneck area (T1) between the channel Na(1) – Na(2), which as a consequence results into expedited movement of Na^+ ions in the structure. However, they only studied 10 and 20 wt.% and found out that conductivity is maximum at 10 wt. % Na excess.

With increasing x in $NZSiP_x$, the concentration of charge carriers (Na^+) is also increased in the system. As a result, the Na^+ ion movement becomes easier until the optimum ratio of vacancies to Na is reached. This means that adding too much Na into the formula unit would, after a certain limit, result in reduced number of vacancies making the Na^+ ion transport difficult. M. Guin [189], performed a detailed study of $Na_{3+x}Sc_2Si_xP_{3-x}O_{12}$, where it is reported that the E_a vs. Na content has a v-shaped curve. The E_a first decreases until the Na content is between 3.0 – 3.4 moles/formula units. For Na content > 3.4 moles/formula unit, the E_a begin to increase [189]. It was later supported with a similar observation on $Na_{3+x}Sc_xZr_{2-x}Si_2PO_{12}$ solid solution [93]. Their results are in agreement with this study in the range of 3.0 – 3.4 mole of Na per formula unit (for the first half), assuming that the glassy phase Na is not considered (Fig. 4.35b). However, if the glassy phase Na is considered, that would leave NASICON stoichiometry different than what we have obtained in the analytical results. It can be any composition in the NASICON region of the Na_2O – SiO_2 – ZrO_2 – P_2O_5 quarterly phase diagram, which certainly requires deeper investigation and will be discussed in section 5.2.

It is, however, certain that any likelihood of Na occupying immobile Zr sites can be ruled out because we observed a changing (decreasing) E_a confirming the mobility of additional Na in $NZSiP_x$.

Chapter 5: Results and Discussion Part II: Orchestrating the NASICON chemistry

5.1. Equimolar Al/Y substituted NASICON

5.1.1. Motivation

This study is performed to verify the guidelines of designing fast ionic conducting NASICONs by Guin and Tietz [91] based on a structure-composition-property correlation comprising more than 110 NASICON compositions. These parameters are already described in section 2.3.4.

Previously, $Na_{3+x}Sc_2Si_xP_{3-x}O_{12}$ ($NSSiP_x$) [188] and $Na_{3+x}Sc_xZr_{2-x}Si_2PO_{12}$ ($NSZSiP_x$) [93] series were used to validate the hypothesis put forward in this review, as shown in Fig. 5.1. Both series fulfill the design parameters stated in [91] with the difference being the substitutional concept for increasing charge carriers, i.e. influencing the different bond strengths within the polyanionic lattice. In the series $NSSiP_x$, the structure contains only Sc^{3+} – O – Na^+ bonds whereas in the series $NSZSiP_x$ a mixture of Sc^{3+} – O – Na^+ and Zr^{4+} – O – Na^+ bonds are present. The Zr^{4+} ions polarize the oxygen atoms more strongly than the Sc^{3+} ions. These stronger attractive interactions should lead to shorter Zr^{4+}-O bond lengths and, as a result, to weaker Na^+-O interactions, facilitating the Na^+ mobility. In contrast, cations with lower valency, e.g. Sc^{3+}, polarize the oxygen atoms less and therefore they are expected to interact more with the Na^+ cations in the conduction pathways, consequently hindering the mobility of Na^+. For the stronger Zr^{4+} – O bonds, the Na^+ – O bond is weak and, as a consequence, Na^+ mobility is higher [200] as proven for the two series $NSSiP_x$ and $NSZSiP_x$ and shown in Fig. 5.1.

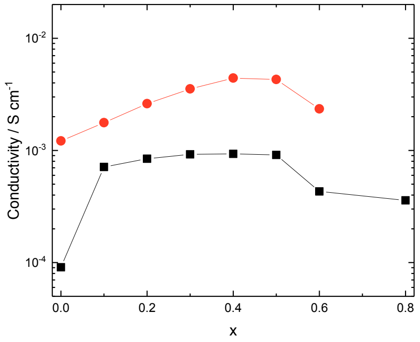

Fig. 5.1: The room temperature conductivity data of the $Na_{3+x}Sc_2Si_xP_{3-x}O_{12}$ [188] (squares) and $Na_{3+x}Sc_xZr_{2-x}(SiO_4)_2(PO_4)$ [93] (circles) series.

In contrast, the cation with a lower valency (Sc^{3+}; $r = 0.745$ Å) induces a weaker bond to the oxygen ion, which compensates the bonding force with a stronger attraction to the Na^+ ions, i.e. the sodium mobility is lower in the $Na_{3+x}Sc_2Si_xP_{3-x}O_{12}$ [200, 201] series. As an example, the best conductivities observed in both series are 4 mS cm^{-1} and 0.8 mS cm^{-1} for $Na_{3.4}Sc_{0.4}Zr_{1.6}Si_2PO_{12}$ and $Na_{3.4}Sc_2Si_{0.4}P_{2.6}O_{12}$, respectively [93, 188]. These results explain the electrostatic impact of the metal cations involved in the structure, as the steric effect in both series is almost negligible due to the very similar ionic radii. In order to further understand the influence of other substituting cations, a double substitution was considered in this study and a novel $Na_{1+2x+y}Al_xY_xZr_{2-2x}(SiO_4)_y(PO_4)_{3-y}$ solid solution ($0 \leq x \leq 1$, $y = 0, 2$) was investigated, where Zr^{4+} ($r = 0.72$ Å) is partially substituted with equimolar amounts of Al^{3+} ($r = 0.53$ Å) and Y^{3+} ($r = 0.90$ Å). Hereinafter, the compositions without silicon ($y = 0$) substitution will be abbreviated as NAYZP$_x$ and those with substitution ($y = 2$) as NAYZSiP$_x$. In this system, although r_{eff} is almost constant and varies only between 0.718 Å and 0.720 Å, the substituting cations with different radii but the same charge may interfere with the sodium transport in a different way to the substitution with Sc^{3+}. This study thus provides further insight into the influence of the electrostatic impact of the cations in the polyanionic sub-lattice.

5.1.2. X-ray diffraction

The XRD patterns of pechini synthesized NAYZP$_x$ (x = 0–0.3, 1) after sintering are shown in Fig. 5.2. Very weak reflections in a non-systematic but reproducible manner are found for x = 0 – 0.15 and 0.25 showing fluctuating minor contents between 1-5 wt.% for $Na_3Y_2(PO_4)_3$, YPO_4 [202], orthorhombic $AlPO_4$ [203] and monoclinic ZrO_2. In the sample with $x = 0.20$, the amount of YPO_4 is exceptionally and also reproducibly higher (about 10 wt.%). For $x >$ 0.25, a continuous increase in YPO_4 and $Na_3Y_2(PO_4)_3$ indicates that the solid solution has definitely reached its limit. For the complete Zr substitution (x = 1), the NASICON crystal structure completely disappeared and mainly YPO_4 formed in addition to smaller amounts of $Na_3Y_2(PO_4)_3$ [204].

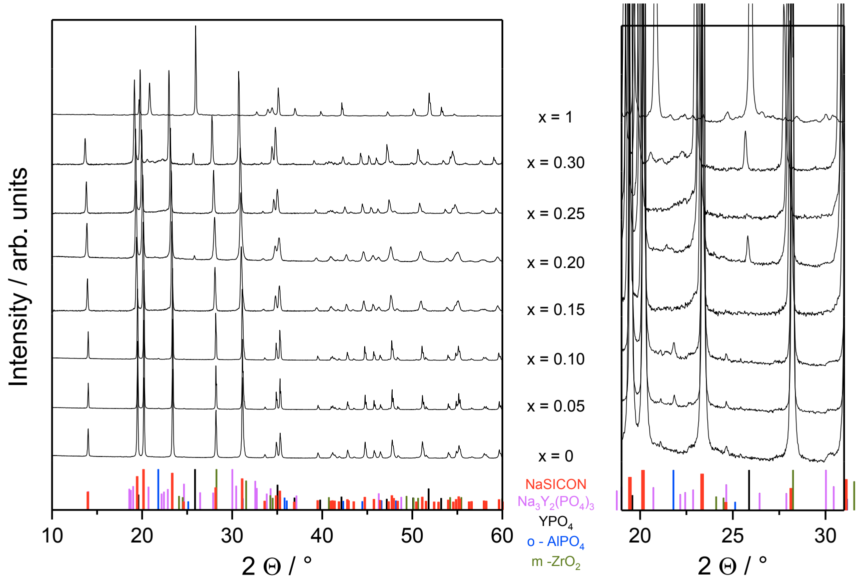

Fig. 5.2: The X-ray diffraction patterns of NAYZP$_x$ (x = 0–0.3 and 1) prepared using the Pechini synthesis method. The left figure shows the genera pattern and the right figure a detail with enlarged intensities to better visualize the small reflections of impurity phases. The bold red vertical lines refer to the NASCON phase [166], lines in magenta, black, blue and green indicate the patterns of $Na_3Y_2(PO_4)_3$ [205], YPO_4 [206], $AlPO_4$ [207] and ZrO_2 [167], respectively.

The XRD patterns of pechini synthesized NAYZSiP$_x$ (x = 0–0.3) after sintering are shown in Fig. 5.3a. The NAYZSiP$_x$ adopts a *C2/c* monoclinic structure for $0 \leq x \leq 0.2$, and transforms into a rhombohedral $R\bar{3}c$ phase when x = 0.3. Monoclinic ZrO_2 was detected in all samples. The monoclinic → rhombohedral transition can be seen by a merging of (111), $(\bar{2}\ 0\ 2)$ and $(\bar{3}\ \bar{1}\ \bar{1})$ reflections into $(\bar{1}\ 1\ 4)$ in Fig. 5.3b.

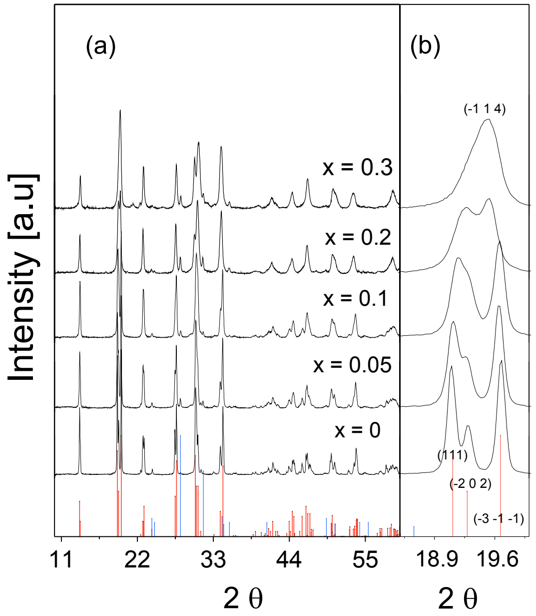

Fig. 5.3: a) XRD patterns of NAYZSiP$_x$ ($0 \leq x \leq 0.3$) after sintering. The red and blue vertical lines correspond to NASICON [166] and ZrO_2 [167], respectively, taken from [166, 167]. The zoomed in region (b) shows the monoclinic (C2/c, $0 \leq x \leq 0.1$) to rhombohedral ($R\overline{3}c$, $x \geq 0.1$) transition.

Table 5.1: Crystallographic data, coefficient of thermal expansion, and melting temperature for the compounds in the $Na_{1+2x}Al_xY_xZr_{2-2x}(SiO4)_y(PO_4)_3$ system.

Composition	**Space group**	**a (Å)**	**c (Å)**	**Fitting parameter R_{wp} (%)**	**V (Å^3)**	**$\sigma_{b,25\,°C}$ (Scm^{-1})**	**CTE 10^{-6} (K^{-1})**	**T_m (°C)**
$NaZr_2(PO_4)_3$	$R\overline{3}c$	8.805(5)	22.776(1)	4.5	1529.2	$3.1 \cdot 10^{-7}$		
$Na_{1.1}Al_{0.05}Y_{0.05}Zr_{1.9}(PO_4)_3$	$R\overline{3}c$	8.812(2)	22.779(2)	4.8	1531.8	$1.1 \cdot 10^{-6}$		
$Na_{1.2}Al_{0.1}Y_{0.1}Zr_{1.8}(PO_4)_3$	$R\overline{3}c$	8.816(1)	22.789(1)	3.7	1533.9	$5.0 \cdot 10^{-6}$		
$Na_{1.3}Al_{0.15}Y_{0.15}Zr_{1.7}(PO_4)_3$	$R\overline{3}c$	8.824(4)	22.805(3)	6.6	1537.8	$6.0 \cdot 10^{-6}$		
$Na_{1.4}Al_{0.30}Y_{0.30}Zr_{1.4}(PO_4)_3$	$R\overline{3}c$	8.876(3)	22.855(2)	8.8	1559.4	$6.2 \cdot 10^{-6}$		
$Na_3Zr_2(SiO_4)_2(PO_4)_3$*	C2/c	9.032(3)	23.042(4)	4.4	1629.5	$1.7 \cdot 10^{-3}$	5.42	1315
$Na_{3.1}Al_{0.05}Y_{0.05}Zr_{1.9}(SiO_4)_2(PO_4)$*	C2/c	9.047(6)	23.021(6)	4.2	1633.2	$1.6 \cdot 10^{-3}$	5.28	1300
$Na_{3.2}Al_{0.1}Y_{0.1}Zr_{1.8}(SiO_4)_2(PO_4)$*	C2/c	9.052(3)	22.948(2)	4.1	1619.6	$1.3 \cdot 10^{-3}$	7.94	1309
$Na_{3.4}Al_{0.2}Y_{0.2}Zr_{1.6}(SiO_4)_2(PO_4)$	$R\overline{3}c$	9.096(1)	22.741(2)	5.9	1629.4	$1.4 \cdot 10^{-3}$	8.92	1269
$Na_{3.6}Al_{0.3}Y_{0.3}Zr_{1.6}(SiO_4)_2(PO_4)$	$R\overline{3}c$	9.110(3)	22.671(1)	1.9	1631.1	$4.6 \cdot 10^{-4}$	8.80	

* The volume of the unit cell of monoclinic system is transformed into rhombohedral.

The lattice parameters of NAYZP$_x$ and NAYZSiP$_x$ are shown in Fig. 5.4. In the NAYZP$_x$ system, an enlargement of the hexagonal lattice is observed in both *a* and *c* directions with increasing *x*. However, in the NAYZSiP$_x$ system, the lattice parameters *a* and *c* show the opposite trend, *c* decreases when *x* is raised, *a* increases. Since the mean ionic radius (r_{eff}) remains constant in all compositions, the variation of the lattice parameters is mainly due to the increasing Na concentration.

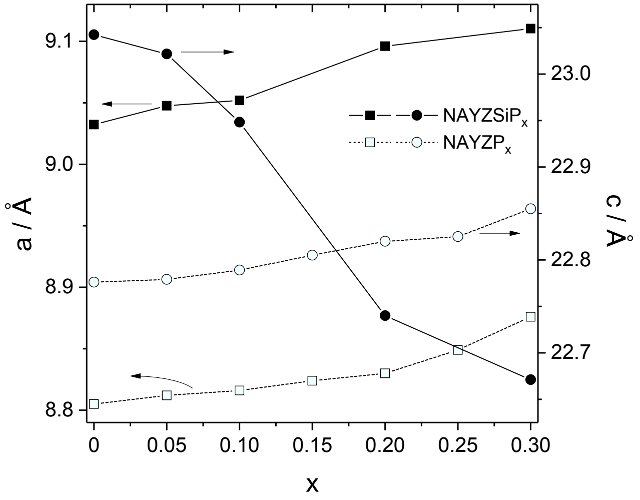

Fig. 5.4: Hexagonal lattice parameters of the series NAYZP$_x$ and NAYZSiP$_x$ with $0 < x < 0.3$.

5.1.3. Size of T1 bottleneck

The size of the bottleneck was calculated from the oxygen and sodium atom positions in the crystal lattice, which were obtained from Rietveld refinement of the XRD data. The area of triangles T1 and T_2 is plotted against the substitution level in Fig. 5.5, indicating that T1 is significantly smaller than T2. In addition, the T1 is decreasing in NAYZSiP$_x$ and increasing in NAYZP$_x$ when the substitution of Al and Y is increased. The decrease or increase in the T1 area indicates enlargement or contraction of the channels through which sodium ions have to pass. It is evident by an increasing in bulk conductivity with the enlargement of T1 area, as shown in Fig. 5.6. As a consequence, it directly affects activation energy of sodium ion conductivity, as reviewed in detail in [91]. Therefore, an increase in the activation energy (E_a) of sodium ion conductivity can be expected for NAYZSiP$_x$. However, E_a is also influenced by parameters like monoclinic distortion in the crystal structure and the sodium concentration per formula unit, but the extent of influence of each individual parameter is still not clarified yet.

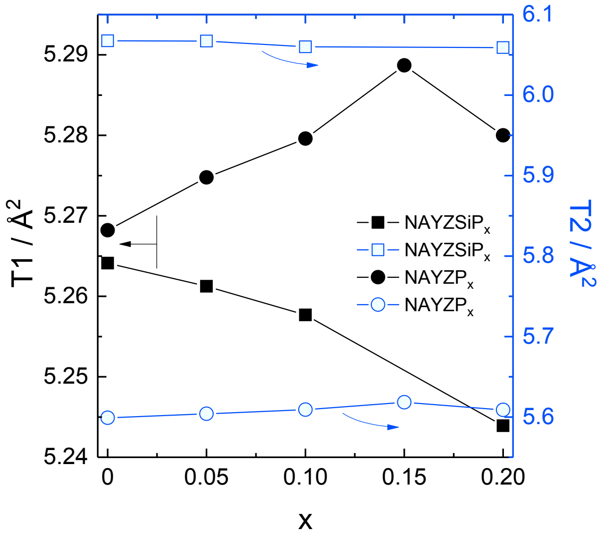

Fig. 5.5: Area of T1 and T_2 obtained from Rietveld refinement of the XRD data as a function of x in NAYZSiP$_x$ (squares) and NAYZP$_x$ (circles).

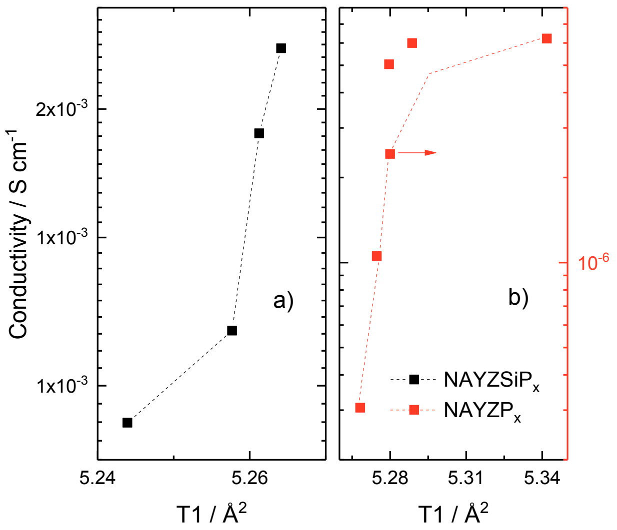

Fig. 5.6. σ_b as a function of T1 area of a) NAYZSiP$_x$ and b) NAYZP$_x$

5.1.4. Coefficient of Thermal Expansion

High-temperature XRD

The HT-XRD patterns of NAYZSiP$_x$ between 2θ = 18° and 20° are shown in Fig. 5.7. The figure depicts a monoclinic to rhombohedral phase transition taking place between 100 °C and 200 °C for NAYZSiP$_0$, NAYZSiP$_{0.05}$, and NAYZSiP$_{0.1}$. For temperatures higher than 700 °C, the patterns indicate a reversible secondary phase transition (not shown here). During heating, the peaks shift to the left due to an expansion of the lattice parameters.

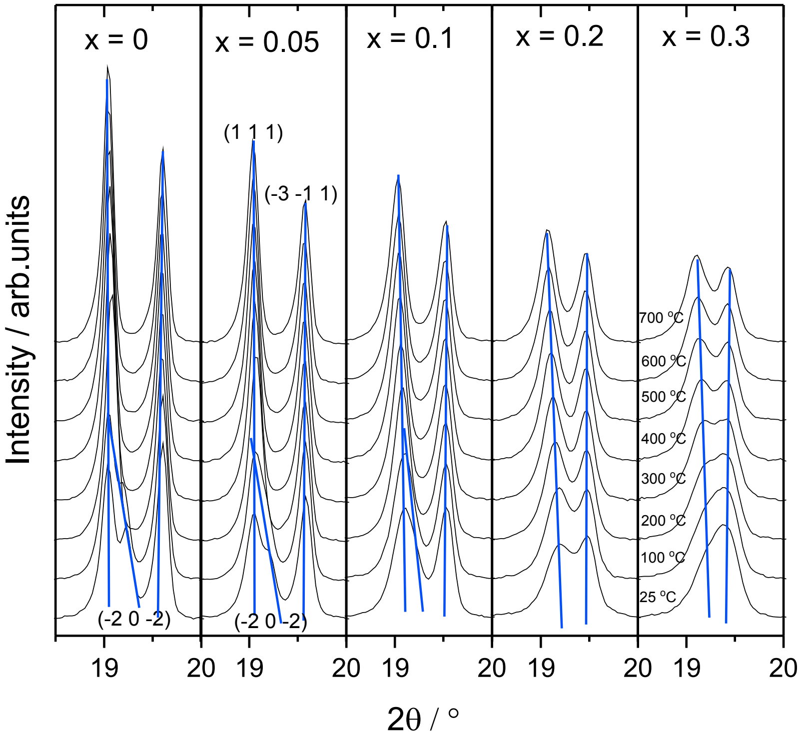

Fig. 5.7: The HT-XRD reflections of NAYZSiP$_x$ between 18° and 20° visualize the phase transition between 100 °C and 200 °C. The reflections shown at 19.1^0 and 19.7^0 correspond to the reflections (1 1 1) and $(\bar{3}\ \bar{1}\ 1)$ of the rhombohedral lattice. The reflections from $(\bar{2}\ 0\ 2)$ transform into (1 1 1) upon heating. The blue lines connecting the peak maxima provide visual guidance.

The hexagonal lattice parameters and volume of NAYZSiP$_x$ obtained from HT-XRD are plotted as a function of temperature in Fig. 5.8. The volume of the unit cell expands with increasing temperature and also shows that the system undergoes strong expansion in the *c* direction as opposed to the *a* direction. A similar expansion anisotropy is also observed for $Na_{3+x}Sc_2Si_xP_{3-x}O_{12}$ [188]. The anisotropic thermal expansion may lead to large residual stresses during cooling, inducing the formation of micro-cracks, as has already been reported for NASICON-type ceramics and is described further in section 3.3 [208, 209]. The volume expansion shows a remarkable slope change with temperature. Whereas $NAYZSiP_0$, $NAYZSiP_{0.05}$, and $NAYZSiP_{0.1}$ only differ in a shift of the absolute values, $NAYZSiP_{0.2}$ and $NAYZSiP_{0.3}$ have a much stronger volume expansion than the other three compositions.

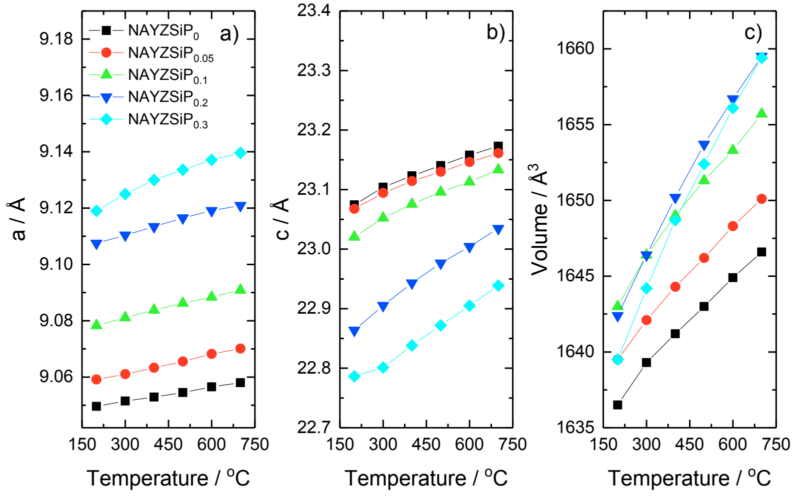

Fig. 5.8: Dependence of lattice parameters (a, b) and the unit cell volume of $NAYZSiP_x$ on temperature. Only the temperature region is shown in which the rhombohedral structure was observed i.e. > 200 °C.

The coefficient of thermal expansion (CTE) was calculated using the lattice expansion data of the HT-XRD measurements and the Eq. 18

$$CTE_{HT-XRD} = \left(\frac{\Delta a}{a} + \frac{\sqrt{3}\cdot\Delta a}{2a} + \frac{\Delta c}{c}\right)\frac{1}{\Delta T} = \frac{\Delta V}{V_0(\Delta T)} \qquad \text{Eq. 18}$$

The resulting CTE of the volume expansion can be related to the linear CTE obtained from dilatometry measurements with

$$CTE_{linear} = \frac{\Delta L}{L_0(\Delta T)} = \frac{1}{3}\frac{\Delta V}{V_0(\Delta T)} = \frac{1}{3}CTE_{HT-XRD} \qquad \text{Eq. 19}$$

The CTE_a, CTE_c, and CTE_{linear} obtained from Eq. 18 and Eq. 19 are compared in Fig. 5.9 for NAYZSiP$_x$ between 200 ^{0}C and 700 ^{0}C. There is strong difference in the thermal expansion of the two lattice parameters and the CTE_c/CTE_a ratio varies between 3 and 5. This anisotropy is typical for NASICON materials [210, 211].

The CTE_{linear} of NAYZSiP$_x$ increases from $4.1\cdot10^{-6}$ K^{-1} to $8.1\cdot10^{-6}$ K^{-1} for NAYZSiP$_0$ and NAYZSiP$_{0.3}$, respectively, which is in agreement with NASICON in which only yttrium was substituted $(5.9\text{-}11.7)\times10^{-6}$ K^{-1} [212].

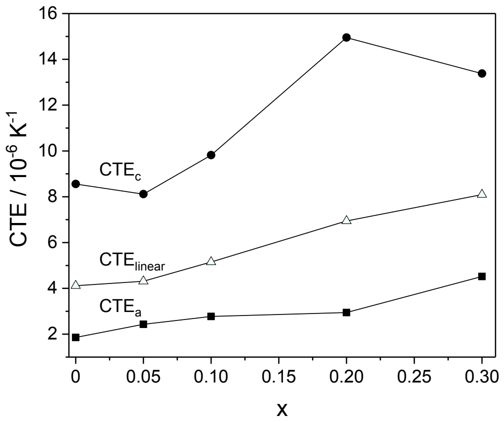

Fig. 5.9: The CTEs of NAYZSiP$_x$ derived from HT-XRD measurements.

Dilatometry

The dilatometry measurements of the series NAYZSiP$_x$ during heating is shown in Fig. 5.10. The dilatometry curves indicate a small change in slope between 120 and 160 °C, which corresponds to the monoclinic to rhombohedral phase transition [14]. The transition temperature decreases with increasing the substitution content till $x = 0.2$. As shown in Fig. 5.11a, the transition temperatures can be easily obtained from the first derivative of the dilatometry curves showing better the slope changes. Additional slope changes at higher temperatures are also visible in Fig. 5.10. The straight dashed lines indicate the deviation from a linear thermal expansion and show on the one hand that the additional expansion increases with increasing x and on the other hand that the onset temperature of the additional expansion decreases with increasing x. The slope changes at high temperatures are summarized in Fig. 5.11b and consist of two contributions which both tend to decrease in temperature with increasing x. In addition, in this temperature region secondary phase formation is observed by HT-XRD measurements. The onset temperatures and maxima of slope changes are listed in Table 5.2.

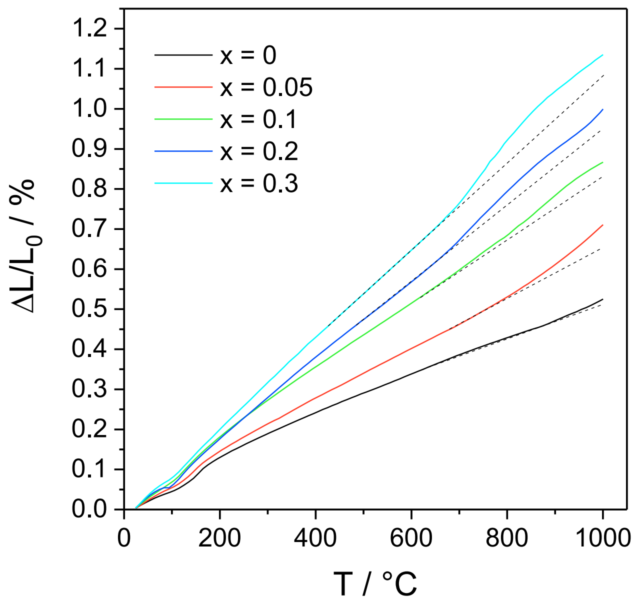

Fig. 5.10: Heating curves of the series NAYZSiP$_x$

This change in slope could be due to crystallization processes and, especially for the samples with $x \geq 0.1$, the formation of new phases as observed in HT-XRD measurements. Starting at about 700 °C, the substituting cations Al^{3+} and Y^{3+} leave the NASICON structure, form ternary compounds like $Y_4Al_2O_9$ and $AlPO_4$ and consequently reduce the unit cell volume of NASICON. It is therefore interesting to note that the substituting elements show a low solubility in the NASICON structure at 1000 °C and below, whereas they are widely incorporated in the host lattice at sintering temperatures of 1150-1200 °C. The leaching of Al^{3+} and Y^{3+} at 1000 °C can be monitored during the short dwell time of 0.5 h during the dilatometer measurements. In this period the samples elongate very systematically with an individual constant rate which is proportional to the substitution level. After 0.5 h they have accumulated a length increase by $(0.126 \pm 0.008)x$ (in %). This phenomenon is also the reason why the CTE obtained from dilatometry curves is higher than the values derived from HT-XRD (Table 2). Apart from the shift in length during the dwell time, the cooling curves do not show any unusual phenomena like hysteresis, abrupt length changes or smooth minima which were frequently observed in former investigations [211, 213-217].

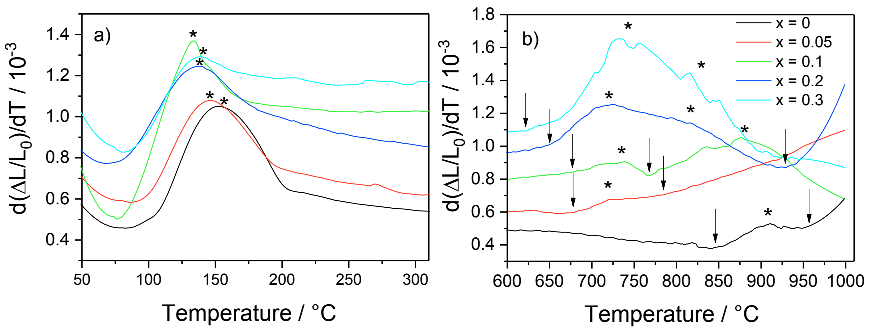

Fig. 5.11: The first derivative of the dilatometry curves during heating for identification of the phase transition (a) and characteristic temperatures related to high-temperature processes (b). Stars and arrows indicate the maximum slope changes and onset temperatures, respectively.

Table 5.2: Onset temperatures and maxima of slope changes deduced from Fig. 5.11 a-b. The values of the high-temperature processes have an error of about ± 20 °C.

x	$T_{mon\text{-}rhom}$	T_{onset1}	T_{max1}	T_{onset2}	T_{max1}
	(°C)				
0	152	850	910	955	> 1000
0.05	146	675	720	780	> 1000
0.1	138	670	735	770	880
0.2	136	650	720	935	815
0.3	138	625	740	-	830

This phenomenon is also the reason why the CTE obtained from dilatometry curves is higher than the values derived from HT-XRD. The CTE of NAYZSiP*x* can be obtained from the slope of the dilatometry curves by using Eq. 9.

In the case of NASICON materials, often the CTEs obtained from dilatometry are much smaller than the ones from HT-XRD. This is because these materials expand anisotropically that often leads to creation of cracks [213, 218] during cooling after sintering. Subsequently during the dilatometry measurements, these cracks vanish due the volume expansion of the material, and consequently the detected dimension changes of the sample is smaller than a crack-free material. Therefore in the past the NASICON materials were frequently claimed to be class of “zero-expansion materials”, a misinterpretation of erroneous dilatometer curves [215, 216, 218, 219]. However, a careful sample preparation would result in similar CTE values obtained from dilatometry and HT-XRD, e.g. in this study the difference is in the range 0.5 – 2.5 x 10^{-6} K^{-1}, as shown in Table 5.2.

In Fig. 5.12 the CTEs of the NAYZSiP$_x$ system are compared to those of $Na_{3+x}Sc_2Si_xP_{3-x}O_{12}$ [189], $Na_{1+x}Zr_2Si_xP_{3-x}O_{12}$ [213, 219] and $Na_{3+x}Y_{0.12}Zr_{1.88}Si_xP_{3-x}O_{12}$ [212]. Among these materials a general observations is evident: materials containing only Zr^{4+} as transition metal in the polyanionic lattice show a much smoother slope with increasing sodium content than those materials with mixture of tetra- and trivalent cations (Sc^{+3}, Al^{+3} and Y^{+3}) or materials containing only trivalent cations. Obviously, the two different bond strengths, i.e. $Zr^{4+} – O^{2-}$ and $M^{3+} – O^{2-}$ (with M = Sc, Y, Al), cause a different dependence of the thermal expansion and vibrational amplitudes on the composition of the NaSICON materials.

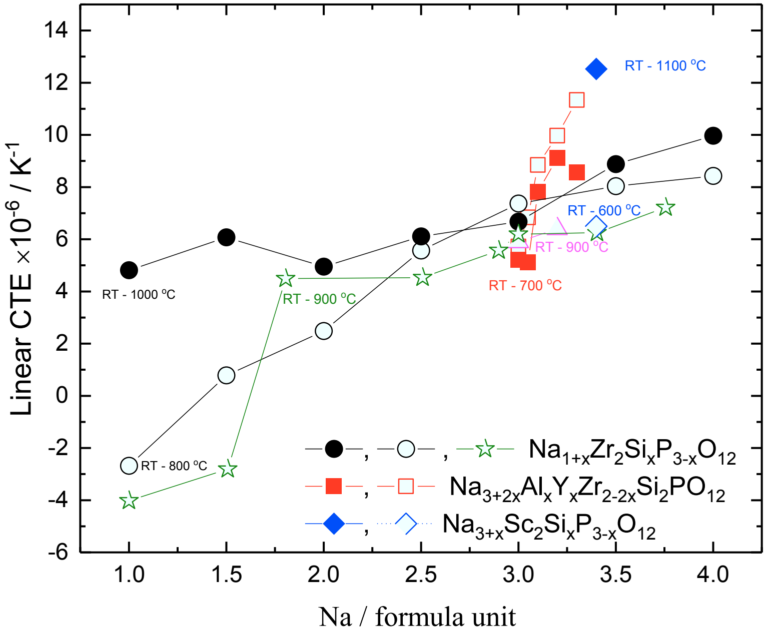

Fig. 5.12: The CTE data of NAYZSiP$_x$ (red triangles) obtained by HT-XRD and dilatometry (red squares). They are compared with other NASICON materials reported in the literature. Black circles represent $Na_{1+x}Zr_2Si_xP_{3-x}O_{12}$ [213], blue diamonds $Na_{3+x}Sc_2Si_xP_{3-x}O_{12}$ [189], green stars $Na_{1+x}Zr_2Si_xP_{3-x}O_{12}$ [219] and pink triangles $Na_{3+x}Y_{0.12}Zr_{1.88}Si_xP_{3-x}O_{12}$ [212]. Filled and empty symbols represent data obtained from HT-XRD and dilatometry, respectively.

On the one hand the CTEs of NASICON materials increase with Na content per formula unit when Zr^{4+} is used as transition metal cation in the polyanionic lattice. This is because at higher temperature sodium ions become highly mobile, induce increased repulsive forces and therefore increase the vibrational magnitude within the lattice. On the other hand, the substitution with trivalent transition metal cations (e.g. Al^{3+}, Sc^{3+}, Y^{3+}) also influences the CTE of the NASICON material. Since the trivalent cations are replacing Zr^{4+} in the crystal lattice (Fig. 5.13), the octahedra become larger due to less charge polarization of oxygen atoms, or in other words, reduced bond strength between trivalent cation and oxygen in the octahedra. This is validated by the calculations of the volume of ZrO_6 [166] and ScO_6 [188] octahedra, i.e. 11.69 Å^3 and 13.49 Å^3, respectively. As a consequence of enlarged octahedra with central trivalent cations, the lattice vibrations become more pronounced, especially at elevated temperatures. This explains why the CTE of NAYZSiP$_x$ and other NASICON compounds substituted with trivalent cations is increasing much more in dependence of x than NASICON materials with tetravalent cations.

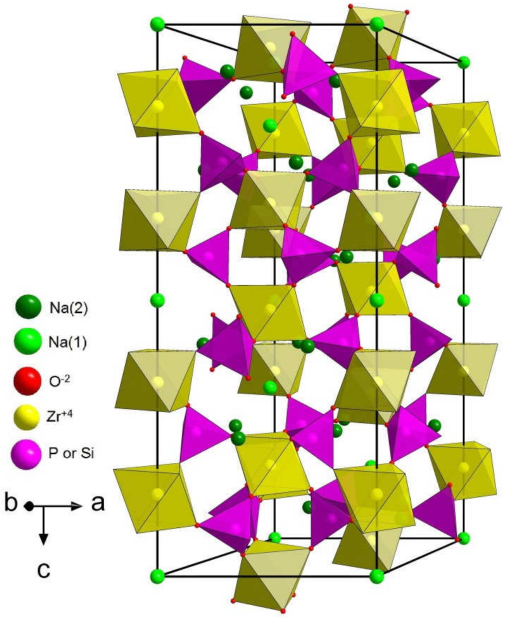

Fig. 5.13: Rhombohedral NASICON structure along c-direction indicating the ZrO_6 octahedra, $(P/Si)O_4$ tetrahedra and sodium atoms. The structural data are taken from [188]. The figure shows the hexagonal unit cell of the NASICON lattice, which exists above 150 °C in all NAYZSiP$_x$ compositions.

5.1.5. Thermal Investigation

DTA/TG curves of two selected specimens are shown in Fig. 5.14. Because the samples were stored in air, the weight loss below 500 °C can be attributed to release of H_2O (up to 250 °C) and CO_2. However, above around 1300 °C, the weight loss is due to the evaporation of Na_2O and/or P_2O_5. Since the sintering temperature ranged from 1000 °C to 1250 °C, any possibility of material loss during heat treatments can be neglected.

In NAYZP$_x$ system, the first thermodynamic event occurs below 400 ^{0}C as indicated by integer 1 in the Fig. 5.14 a-b. This is followed by the crystallization into a NASICON structure. A weight loss in TG curves after 1300 ^{0}C is due to the loss of sodium oxide.

In the case of the NAYZSiP$_x$ system, the first thermodynamic event is the removal of organics below 400 ^{0}C and indicated by integer 1 in the figure. The second even occurs between 750 – 800 ^{0}C for $0 \leq x \leq 0.3$ and it is indicated by integer 2 in the figure. This event was also observed for $Na_{3+x}Zr_2Si_2PO_{12}$ in section 4.3 where it was already interpreted as a partial melting or amorphisation. This forms a glassy phase upon solidification is richer in Si than the surrounding crystalline NASICON grains and appears gray in the SEM images (see next section). The third event appears at ~ 1300 °C, which corresponds to melting of the ceramic and it is indicated by integer 3 in the figure. The melting temperatures of the NAYZSiP$_x$ compounds are listed in Table 5.1. A weight loss in TG curves after 1300 ^{0}C is due to the loss of sodium oxide.

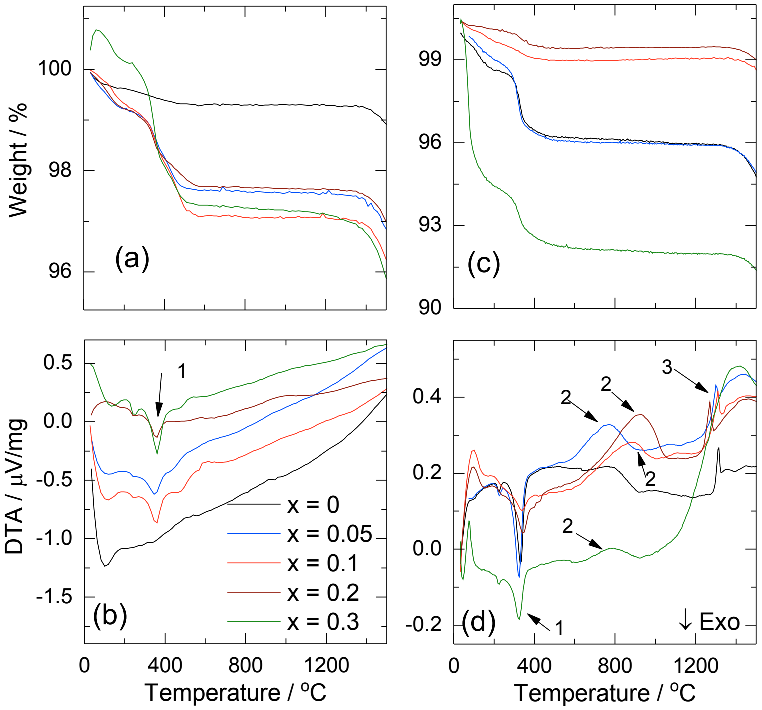

Fig. 5.14: Thermal investigation of NAYZP (left) and NAYZSiP (right) showing (b, d) the DTA results and (a, c) the TG results.

5.1.6. Microstructure

Microstructures of NAYZP$_x$ with $x = 0.10$, 0.20, and 0.25 sintered at 1200 °C for 10 h in air are shown in Fig. 5.15. The samples with $x = 0$ and $x = 0.05$ did not densify at the sintering temperature and relative densities of only 52 % and 75 % were achieved. For $0.1 \leq x \leq 0.3$, the relative density of the samples varied between 87 % and 91 %. The microstructure of all three compositions was similar in general. However, the NAYZP$_{0.20}$ composition contained YPO_4 as a secondary phase in addition to ZrO_2, with the latter present in all compositions. The microstructure of NAYZSiP$_x$ specimens with $x = 0$, 0.05, and 0.1 is also shown, indicating a similar relative density (85–93 %). The microstructure of the other compositions is very similar and therefore not shown here. The formation of ZrO_2 is already discussed in section 4.1.2.

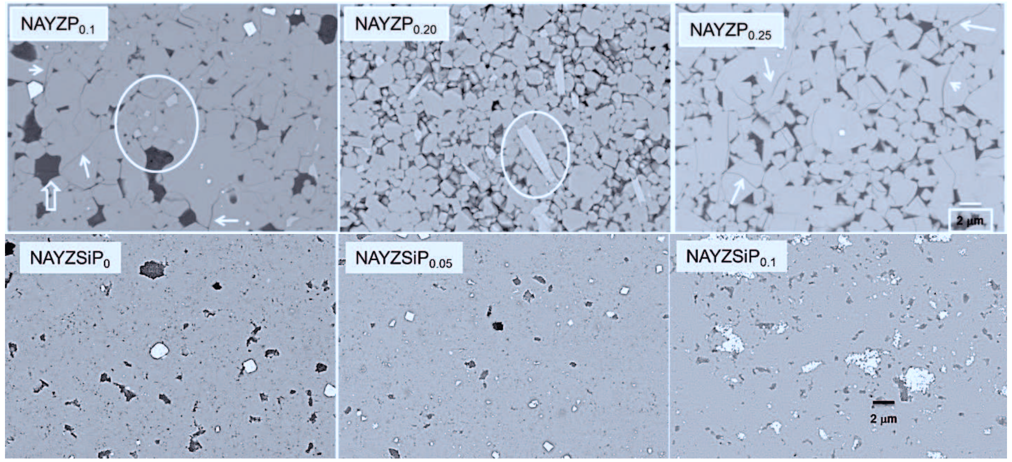

Fig. 5.15: Scanning electron microscopy images of polished cross sections of (top) NAYZP$_x$ sintered at 1200 °C for 10 h in air and (bottom) NAYZSiP$_x$ sintered in two steps (1200 °C for 0.5 h followed by 1150 °C for 5 h) in air. The white phase is ZrO_2, the circled phase is YPO_4, and the arrows indicate micro-cracks. The arrows indicate cracks and pores.

5.1.7. Electrical Conductivity

Nyquist plots of NAYZP$_x$ (x = 0–0.3) are shown in Fig. 5.16a. The formation of two semicircles indicates high grain boundary resistance in the sample in addition to bulk resistance. The bulk (σ_b) and grain boundary (σ_{gb}) conductivities were obtained from bulk and grain boundary resistance (R_b and R_{gb}) using the equation $\sigma = L/(A \cdot R)$, where L and A represent the length and area of the specimen, respectively. These semicircles were fitted using the ZView® computer software, to obtain bulk, grain boundary, and total conductivities, as shown along with the equivalent circuit in Fig. 5.16b.

In the NAYZP$_x$ system, σ_b increases with the number of Na per formula unit, except for when x = 0.2, which contains a high amount of the YPO_4 impurity phase. The conductivity of NAYZP$_x$ is in the order of 10^{-6} S cm^{-1}, which is low for an electrochemical application. The low conductivity is due to the low sodium content in the compounds. In addition, the rhombohedral crystal structure has only two sodium positions, Na(1) and Na(2), thereby allowing Na^+ ion conduction along only one pathway (see Fig. 2.5a). Conductivity increased due to the increase in the amount of charge carriers (Na^+). However, when it reaches 1.4 mol sodium per formula unit, conductivity started to decrease due to the increasing occurrence of secondary phases and micro-cracks.

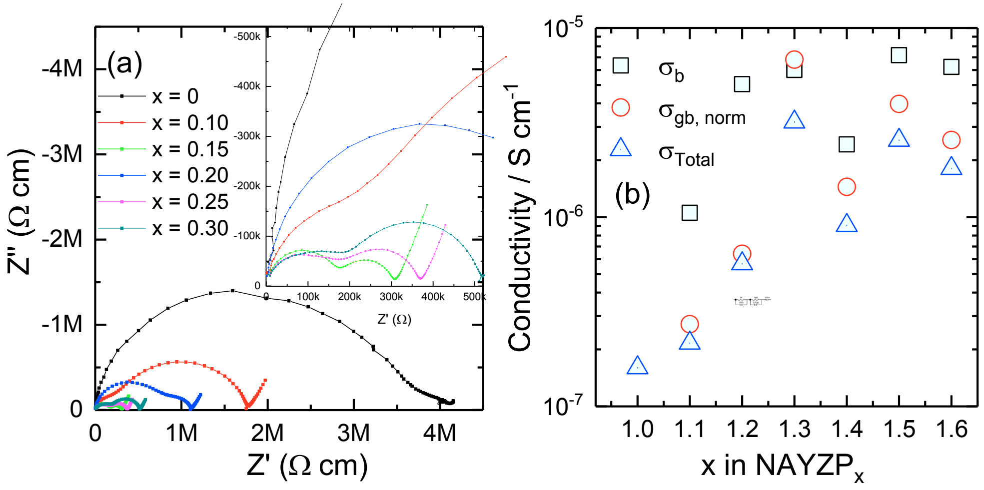

Fig. 5.16: a) Nyquist plot of samples in the NAYZP$_x$ series and b) the σ_b, $\sigma_{b,\,norm}$, and σ_{Total} at 25 ^{0}C. The equivalent circuit is also shown.

In the case of the NAYZSiP$_x$ series, the same interpretation of the impedance data was used. However, since only one semicircle is visible, the R_b/CPE_b element was discarded. Low and high intercepts of the observed single semicircles thus correspond to bulk resistance (R_b) and (R_{Total}), respectively, and the grain boundary resistance was calculated with

$$R_{gb} = R_{Total} - R_b \qquad \text{Eq. 20}$$

The calculated conductivities are shown along with the Nyquist plots in Fig. 5.17. Here, the Al/Y substitution in NAYZSiP$_x$ leads to a decrease in the σ_b and $\sigma_{gb,\ norm}$ values of the samples. Conductivity was highest for the unsubstituted sample, i.e. $x = 0$ (i.e. 3.0 Na/formula unit). The total conductivity of NAYZSiP$_x$ was in the range 0.5–0.06 mS cm^{-1} for $0 \leq x \leq 0.3$, which is two orders of magnitude higher than for NAYZP$_x$. The Si-substituted system, unlike NAYZP$_x$, exhibits monoclinic distortion and has three sodium positions: Na(1), Na(2), and Na(3) [220]. The Na$^+$ ions in the monoclinic lattice jump between these positions in two different pathways (Fig. 2.5b), and the material has a higher conductivity compared to the rhombohedral lattice [221]. Since the NAYZSiP$_x$ is only monoclinic when the Na content is less than 3.2 Na per formula unit, and becomes rhombohedral for Na content > 3.4 Na per formula unit, this might be the reason why σ_b drops significantly when $x > 0.3$ [91, 93, 188]. In addition, the decreasing σ_b within the monoclinic lattice ($0 < x < 0.2$) is related to the decrease in the bottleneck size (area T1, see section 5.1.3).

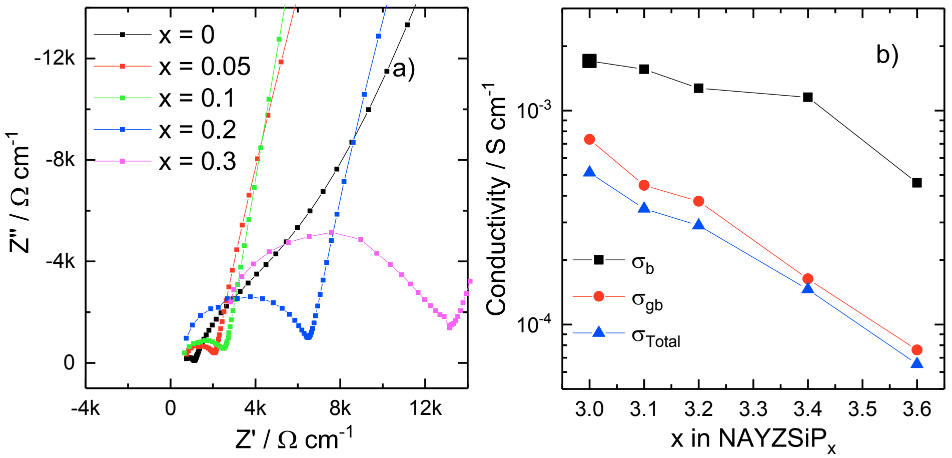

Fig. 5.17: a) Nyquist plot of samples in the NAYZSiP$_x$ series and b) the σ_b, $\sigma_{b,\ norm}$, and σ_{Total} at 25 ^{0}C.

The variation of σ_{gb} corresponds to the influence of the processing conditions affecting the sample microstructure. To keep these variations minimal, samples with relative densities in the range of 86–93 % for all compositions were prepared.

Conductivity measurements at elevated temperatures were carried out on both series, NAYZP$_x$ (only those with comparable relative densities) and NAYZSiP$_x$. The results are shown as a function of inverse temperature in Fig. 5.18 along with the corresponding activation energy. The Arrhenius plot shows that the conductivity of NAYZSiP$_x$ decreases with increasing *x* in the system. This is in agreement with the results in Fig. 5.17. The activation energy of the NAYZSiP$_x$ samples only varies between 0.3 eV and 0.33 eV, and is in agreement with previous studies on NASICON materials [184, 185]. The NAYZP$_x$ samples have conductivities one to four orders of magnitude lower than the Si-substituted compositions, depending on the composition and temperature, due to higher activation energies (0.42 – 0.46 eV).

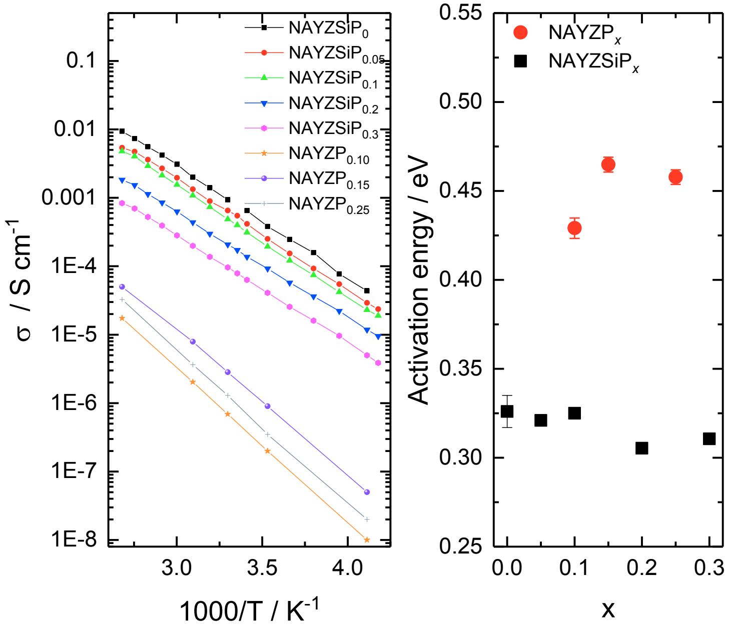

Fig. 5.18: Arrhenius plot (top) of NAYZP$_x$ and NAYZSiP$_x$ measured in the temperature range of -30 °C to 100 °C. The activation energies were determined using the Arrhenius law.

Both series are compared with the $Na_{1+x}Zr_2Si_xP_{3-x}O_{12}$ system as a function of Na per formula unit in Fig. 5.19. In contrast to the Sc-substituted materials (Fig. 5.1), the conductivity of NAYZSiP$_x$ decreased with increasing *x*. This could be due to both structural and processing reasons. The processing route determines the microstructure and, therefore, directly influences conductivity. However, in this case, the relative density of NAYZSiP$_x$ was controlled and in the range of 87–93 %, which is similar to the densities of the Sc-containing materials. The structural factors include crystallographic aspects, for example the lattice parameters, atomic positions, and the size of the bottleneck. The bottleneck size decreased in the NAYZSiP$_x$ system when the amount of substitution was increased and appears to affect its bulk conductivity [93, 188, 194, 214].

A suitable fast ion conductor is one that i) fulfills optimal crystallographic arrangements to enable high bulk conductivity, and ii) exhibits effective processability to ensure minimum grain boundary resistance. The total conductivity controls the successful application of a material as an electrolyte. Fig. 5.19 compares the total conductivities of the NAYZP$_x$ and NAYZSiP$_x$ series with the $Na_{1+x}Zr_2Si_xP_{3-x}O_{12}$ series. The best conductivity was observed for x = 2, i.e. 3.0 mol Na/formula unit [87]. The increasing conductivity as a function of x in Fig. 5.19 is directly attributable to the increasing number of charge carriers, i.e. the Na concentration. Theoretically, the maximum number of Na per formula unit is restricted to 4. However, the concentration of Na vacancies in the formula unit is also essential to enabling Na^+ to hop along the conduction pathways.

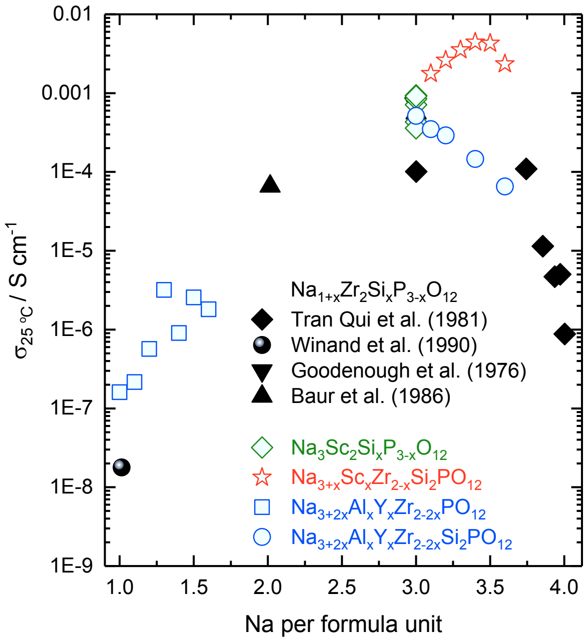

Fig. 5.19: Comparison of NAYZP$_x$ (empty squares) and NAYZSiP$_x$ (empty circles) with the $Na_{1+x}Zr_2Si_xP_{3-x}O_{12}$ series (filled symbols) [87, 221-223]. The series NSSiP$_x$ [189] and NSZSiP$_x$ are also shown [224].

In the $Na_{3+x}Sc_2Si_xP_{3-x}O_{12}$ and $Na_{3+x}Sc_xZr_{2-x}(SiO_4)_2(PO_4)$ series, the optimal ratio between charge carrier and vacancy concentration in the formula unit has been reported as 3.4:0.6 [93, 188]. However, NAYZSiP$_x$ does not follow this experimental observation. Even though the Na^+ concentration increases with Al/Y substitution, the conductivity of the material decreases in spite of the fact that the r_{eff} of the cations is close to 0.72 Å. In contrast to the Sc-containing series, the individual cation sizes differ substantially. Furthermore, the size of the T1 triangle also determines the ease of Na^+ ion transport [91], and its size decreases when the Al/Y substitution is increased, thus explaining the decrease in conductivity along the NAYZSiP$_x$ series. Taking these parameters into consideration, it can be concluded that even if the steric interactions are kept almost constant by using the same r_{eff}, the increasing dissimilarity of the cations involved, from Zr-Zr, Sc-Sc, and Sc-Zr to (Al/Y)-Zr, has a significant impact on ionic conductivity. Atomic orbitals of cations in the MO_6 octahedra (M = Zr, Sc, Y, Al) thus also appear to have a strong influence on the transport properties of the Na^+ ions, as ionic conductivity decreases from *4d* (Zr), *3d* (Sc) to *3p* (Al) elements, even if an additional *4d* element (Y) is involved.

5.2. Reducing the NASICON processing temperature

5.2.1. Motivation

The sodium super ionic conductors (NASICONs) have long been investigated acknowledging their electrical performances and potential in the application as electrolyte materials in batteries and other related applications [22, 225-229]. However, even though their ionic conductivity, in the best case reach 4 mS/cm, their application as electrolyte material has still not commercially realized. In addition to cost, the high processing temperature (1200 – 1300 °C) also restricts optimization of their interface with electrode materials in an all-solid state battery. To achieve this, the processing temperature must be reduced.

NASICON with a range of conductivity have already been compiled in the literature [91]. One reason of the variation in their total conductivity is the differences in the processing conditions. However, quite often the bulk conductivity also differs and any variation in bulk conductivity accounts to the chemistry. A phase diagram of the oxides of Zr, Si, Na and P is shown the phase diagram in Fig 5.21. The figure shows that NASICON structure, instead of a single composition, is a range of compositions adopting the NASICON-type crystallinity. Even though the structure is same, the chemistry can be different and is the lead source of varying conductivity. This is observed by different ICP-OES stoichiometries of SA-SSR and Pechini samples having varying conductivities, as discussed in section 4.1. In addition, it is further evident by a range of conductivities reported for single $Na_3Zr_2Si_2PO_{12}$ composition as shown in Fig. 4.9.

Furthermore, the formation of glass phases also seems likely as the NASICON solid solution is close to the adjacent regions of glass phases. It is already observed in the study of $Na_{3+x}Zr_2Si_2PO_{12}$, described in section 4.3 and all possible phase relations are reviewed by Tietz [230]. It is further confirmed by the reports regarding NASICON materials undergoing a liquid phase assisted sintering [197, 231, 232]. The reason lies in the quaternary phase diagram of the NASICON, where especially the Si-rich compositions tend to form glass materials, and therefore these materials are prone to partial melting during heat treatment. This aspect can be used as a tool to reduce the processing temperature by optimizing the glass phase content. However any attempt of reducing the processing temperature would be a compromise on its conductivity. This is due to the low conductivity of the glass phases 10^{-7} S/cm [233-236].

Since the formation of glass phase during the processing of NASICON cannot be avoided, many attempts were reported where studies have been conducted on NASICON glass-ceramics or so-called NASIGLAS [31, 79, 80, 82, 83, 173, 234, 237]. These NASIGLAS in addition to pure Na^+ ion conducting glass materials [27, 32, 81, 233, 235, 236, 238] are interesting from the fact that their processing temperature is lower than the NASICON ceramic depending upon the amount of glass present. The conductivity of such a glass-ceramic with cubic Na_3PS_4 at 25 ^{0}C is as high as 0.2 mS cm^{-1} and they were prepared by a mechanochemical technique and processed at temperatures even lower than 500 ^{0}C to achieve the given conductivity. It is noteworthy that these glass compositions remain unidentified by conventional XRD and often in the SEM images. However, their presence is significant and therefore makes NASICON materials to be categorized as composites. The properties of composite therefore can be optimized by altering the content of the glass phases. The low melting glass phase can reduce the sintering temperature to 1000 ^{0}C allowing a joint processing along with electrode materials like $Na_3V_2PO_{12}$.

With the target of reducing the processing temperature of NASICON materials, the compositions of the series $Na_{1+x}Zr_xSi_xPO_{(1+x+4x+4x+5)/2}$, where x = 0, 0.4, 0.8, 1.2, 1.6 and 2.0, were prepared. Their nominal stoichiometries are given in Table 5.3. These compositions were synthesized via SA-SSR method as given in detail in section 3.1.1 with a slight modification that the calcination was performed at 500 ^{o}C for 24 h in air.

5.2.2. Elemental Analysis

The elemental analysis of the series indicates an accurate synthesis. The stoichiometry obtained from ICP-OES are compared in Table 5.3 and also plotted against x in Fig. 5.20. All compositions are slightly deficient of Na and significantly deficient of Si and Zr.

The deficiency of these elements is due to the hygroscopicity of sodium and zirconium nitrates as source material. Zirconium nitrate is a strong hygroscopic compound as compared to sodium nitrate, which is observed by its stronger deviation from the nomical stochiometry as compared to Na. The Si deficiency could also be due to an inaccurate content due to storage of TEOS used its source compound. Nevertheless, inserting the ICP-OES stoichiometric compositions in the phase diagram still meet the criterion and achieve the objective of the currrent investigation.

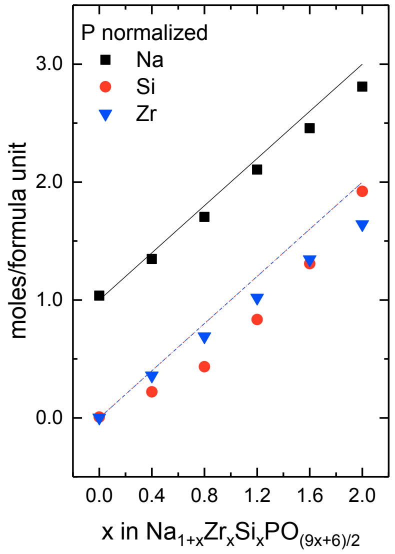

Fig. 5.20: Analytical stoichiometries obtained from ICP-OES of $Na_{1+x}Zr_xSi_xPO_{(9x+6)/2}$. The lines indicate the nominal stoichiometries.

Table 5.3: The nominal and analytical stoichiometries of $Na_{1+x}Zr_xSi_xPO_{(9x+6)/2}$.

	Nominal	Analytical (ICP-OES)
$x = 0$	$NaPO_3$	$Na_{1.04}PO_3$
$x = 0.4$	$Na_{1.4}Zr_{0.4}Si_{0.4}PO_{4.8}$	$Na_{1.35}Zr_{0.40}Si_{0.22}PO_{4.8}$
$x = 0.8$	$Na_{1.8}Zr_{0.8}Si_{0.8}PO_{6.6}$	$Na_{1.70}Zr_{0.70}Si_{0.43}PO_{6.6}$
$x = 1.2$	$Na_{2.2}Zr_{1.2}Si_{1.2}PO_{8.4}$	$Na_{2.11}Zr_{1.02}Si_{0.83}PO_{8.4}$
$x = 1.6$	$Na_{2.6}Zr_{1.6}Si_{1.6}PO_{10.2}$	$Na_{2.46}Zr_{1.34}Si_{1.31}PO_{10.2}$
$x = 2.0$	$Na_{3.0}Zr_2Si_2PO_{12}$	$Na_{2.81}Zr_{1.64}Si_{1.92}PO_{12}$

These analytical and nominal stoichiometeries are also depicted in the Na_2O – SiO_2 – ZrO_2 – P_2O_5 quarternary diagram in Fig 5.21.

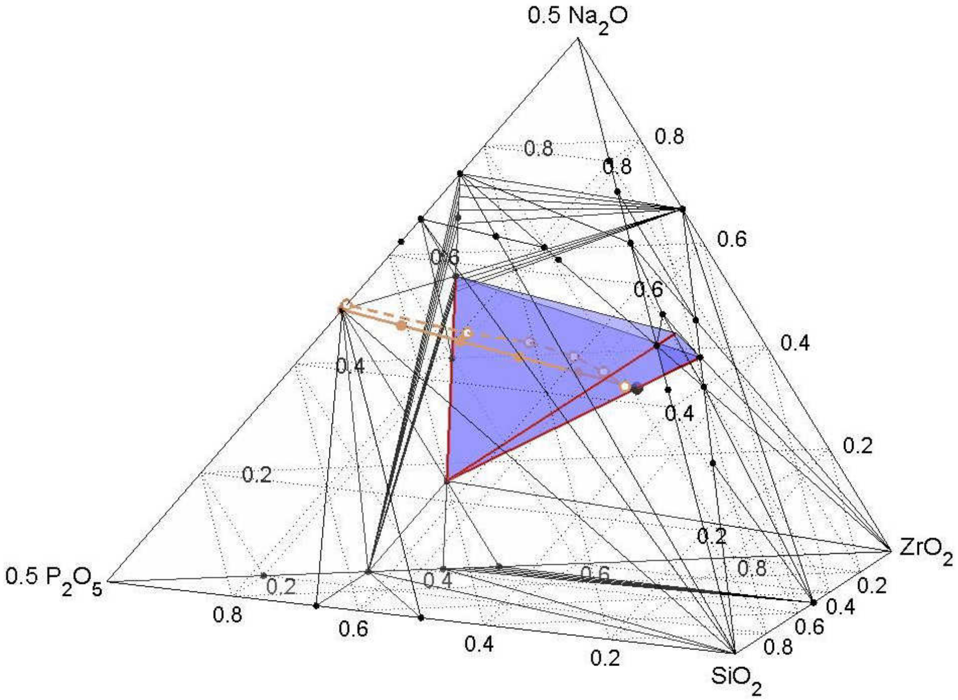

Fig 5.21: The quaternary phase diagram [230]. In the shaded blue region (pyramid), the NASICON structure exists. Solid and dotted orange line depicts the nominal and analytical stoichiometries of the investigated series, respectively.

5.2.3. X-ray diffraction

The XRD was performed and is shown in Fig. 5.22. In order to investigate the evolution of the crystal structure, the calcination was performed at various temperatures with a step size of 100 °C until the melting of the samples. The XRD results of all the compositions are shown in the Fig. 5.22. The figure provides following information about all six compositions:

1. Phases present
2. Melting temperature range (resolution 100 °C)
3. Crystallization of NASICON
4. Size of crystallites (sharpening/broadening of peaks)

In general, the compositions with x = 1.2, 1.6 and 2.0, the samples mainly contain ZrO_2 as an impurity at elevated calcination temperatures. The X-ray reflection at 30° is adjacent to both monoclinic ZrO_2 and cubic SiO_2.

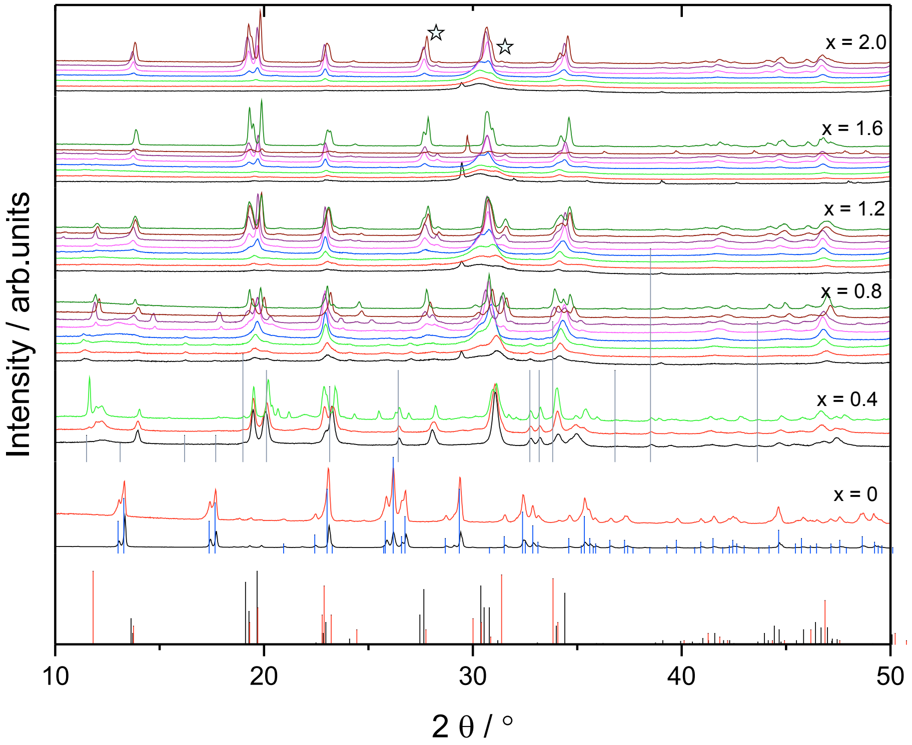

Fig. 5.22: The crystal structure evolution of $Na_{1+x}Zr_xSi_xPO_{(9x+6)/2}$ with increasing x. Each additional XRD pattern indicates an increase of temperature of 100 °C, with minimum and maximum of 500 °C and 1200 °C, respectively. Black, red, blue and grey lines in corresponding layers are the patterns of NASICON [166], $Na_5Zr(PO_4)_3$ [239], $NaPO_3$ [240] and $Na_4(P_2O_7)$ [241], respectively. The stars depict the position of ZrO_2 reflections [167].

All phases formed as a function of temperatures were obtained from XRD results and are summarised in Table 5.4. An overall observation is that for the two extremes, when x = 0 and 2, the phase that are formed are $NaPO_3$ and NASICON respectively. For the compositions in between, the material undergo a complex crystallographic arrangements where $Na_5Zr(PO_4)_3$ and $NaPO_3$ phases coexists along with the NASICON when $0.4 \leq x \leq 1.2$. Additionally, a $Na_4(P_2O_7)$ phase is also observed <1000 °C. However it disappears after heat treatment at high temperature. These phases could be an interesting addition, as one can expect surplus sodium charge carriers and reduced processing temperature due to these high sodium containing phases, respectively. In addition, peak shift of the NASICON phase is also be observed, especially when x = 0.8. This is an indication of varying lattice parameters due to phase formations upon heating.

Table 5.4: Summary of phase evolution of $Na_{1+x}Zr_xSi_xPO_{(9x+6)/2}$ as a function of temperature. Main phases are in bold letters.

Temp. (°C)	***x* = 0**	***x* = 0.4**	***x* = 0.8**	***x* = 1.2**	***x* = 1.6**	***x* = 2.0**
500 °C	**$NaPO_3$** $Na_5P_3O_{10}$	Not crystallized	**ZrO_2** $Na_3Zr_2Si_2PO_{12}$ $Na_5Zr(PO_4)_3$	**ZrO_2** Not Crystallized		
600 °C	**$NaPO_3$** $Na_5P_3O_{10}$	**$NaZr_2(PO_4)_3$** $Na_5Zr(PO_4)_3$ $Na_4P_2O_7$	**ZrO_2** $Na_3Zr_2Si_2PO_{12}$ $Na_5Zr(PO_4)_3$	**ZrO_2** $Na_3Zr_2Si_2PO_{12}$	**ZrO_2** Not Crystallized	
700 °C	Melts	**$NaZr_2(PO_4)_3$** $Na_2Zr(PO_4)_3$	**$Na_5Zr(PO_4)_3$** **$Na_3Zr_2Si_2PO_{12}$** ZrO_2	$Na_3Zr_2Si_2PO_{12}$ $Na_5Zr(PO_4)_3$	**ZrO_2** $Na_3Zr_2Si_2PO_{12}$	
800 °C		**$NaZr_2(PO_4)_3$** $Na_2Zr(PO_4)_3$ $Na_{5.27}Zr_{0.5}Si_{0.5}P_{2.5}O_{12}$	**$Na_5Zr(PO_4)_3$** **$Na_3Zr_2Si_2PO_{12}$** ZrO_2	**$Na_3Zr_2Si_2PO_{12}$** $Na_2Si_2O_5$	**$Na_3Zr_2Si_2PO_{12}$** Na_3PO_4 $Na_5Zr(PO_4)_3$	**$Na_3Zr_2Si_2PO_{12}$** Na_3PO_4
900 °C		Melts	**$Na_2Zr_2SiP_2O_{12}$** ZrO_2 $Na_2Zr(PO_4)_3$	**$Na_3Zr_2Si_2PO_{12}$** ZrO_2 Na_3PO_4 $Na_2Zr(PO_4)_2$	**$Na_3Zr_2Si_2PO_{12}$** ZrO_2 Na_3PO_4	**$Na_3Zr_2Si_2PO_{12}$** ZrO_2
1000 °C			**$Na_3Zr_2Si_2PO_{12}$** $Na_{5.27}Zr_{0.5}Si_{0.5}P_{2.5}O_{12}$ $NaZr_2(PO_4)_3$ ZrO_2 & Na_3PO_4	**$Na_3Zr_2Si_2PO_{12}$** ZrO_2 Na_3PO_4	**$Na_3Zr_2Si_2PO_{12}$** ZrO_2	
1100 °C			**$Na_3Zr_2Si_2PO_{12}$** $Na_5Zr(PO_4)_3$	**$Na_3Zr_2Si_2PO_{12}$** Na_3PO_4 $Na_5Zr(PO_4)_3$		
1200 °C			**$Na_3Zr_2Si_2PO_{12}$** $Na_5Zr(PO_4)_3$	**$Na_3Zr_2Si_2PO_{12}$** Na_3PO_4 $Na_5Zr(PO_4)_3$		
1300 °C			Melts			

5.2.4. Correlation of XRD and Microstructure

In order to visualize the NASICON crystallites and a potential glass phase, the powders x = 0.4 and 1.6 were hand-crushed after calcination at 500 °C, pressed with 200 MPa force and sintered at 700 °C. The sintered pellet the two were then divided into two parts: one for the XRD and one for the SEM investigation, the results are shown in Fig. 5.23 and Fig. 5.24, respectively. The XRD patterns indicate a peak broadening in $x = 1.6$ compared to the $x = 0.4$ composition.

This is due to the fact that for $x = 0.4$ is closer to the $NaPO_3$ glass in the phase diagram (Fig 5.21) as compared to the $x = 1.6$. Therefore, compositions with the net amount of NASICON phase in $x = 0.4$ is less and grows much more rapidly as compared to the $x = 1.6$.

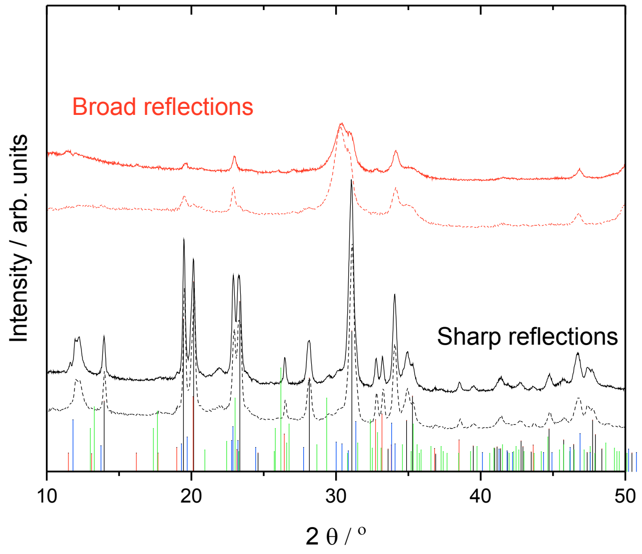

Fig. 5.23: The XRD of $x = 0.4$ (black lines) and $x = 1.6$ (red lines) after heat treatment at 700 °C. The reflections of powder (dotted lines) and pellets (solid lines) are identical. The black, red, green and blue vertical lines are the patterns of NASICON [166], $Na_4(P_2O_7)$ [241], $NaPO_3$ [240] and, $Na_5Zr(PO_4)_3$ [239] respectively.

The correlation of peak broadening is validated from the SEM images of the sintered pellets. The evidence is the crystallite size observed for both compositions. This can be seen at higher magnifications where particles are grown more in $x = 0.4$ as compared to $x = 1.6$.

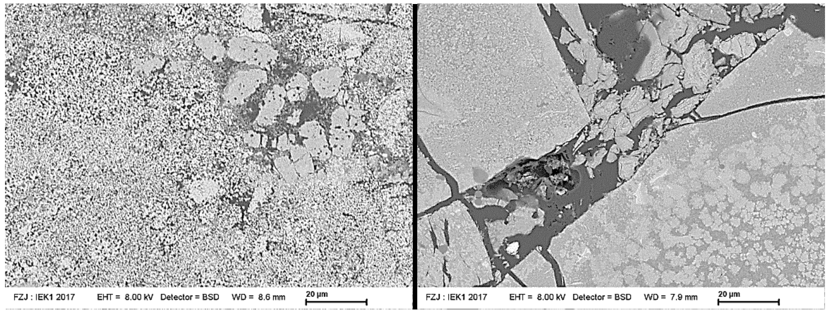

Fig. 5.24: The SEM images of x = 0.4 (left) and x = 1.6 (right).

5.2.5. Thermal analysis

DTA/TG measurements were performed and the results are shown in Fig. 5.25. Following events occurs during heating;

1. The moisture and carbon dioxide is removed below 300 ^{0}C.
2. At 560 ^{o}C an endothermic event is only seen when x = 0. It could be a phase transformation of $NaNO_3$, as it is not associated with any weight loss. This could be related to a unique and not seen in other compositions.
3. Further events occurs between 600 – 800 ^{0}C. These events are idenfied in Fig. 5.25a with a steric and cross symbols. These peaks are also associated with weight loss as seen in Fig. 5.25b correspond to the decomposition of $NaNO_3$ in two steps [242].
4. At 870 ^{o}C and 930 ^{0}C, two small humps are observed only in x = 0.4. These temperatures, when compared with the XRD results, correspond to partial melting of the sample. This is because the samples were deformed after 800 ^{o}C heat treatment, which is a strong indication of softening at this temperature. A very small endothermic hump is observed in all compositions at 750 °C as indicated by sterics in the Fig. 5.25.
5. A continuous rise observed 900 ^{o}C in all compositions except x = 0. This corresponds to the crystallization of NASICON structure.

The reason why x = 0 does not show any crystallization is because it melts already at 620 ^{o}C. However, a weight loss onsetting at 1220 ^{o}C, indicated by an arrow in Fig. 5.25b, might be regarded as sodium loss from the liquid. Furthermore, any possibility of partial melting in other compositions can not be ruled out. As descriped in previous section, the amount of NASICON is increasing with increasing *x* thereby forming only a small amount of molten phase. This might remain undetected through DTA/TG results either because the signal is too small or the signal gets hidden in the $NaNO_3$ decomposition peaks.

6. Finally, a melting of samples was observed by endothermic peaks indicated by diamonds in Fig. 5.25a. These are the temperatures where NASICON starts to melt. It was also observed by melting of pellets when sintering beyond 1200 °C for the XRD.

All these events are also indicated by symbols in Fig. 5.25 and listed in Table 5.5. These are sterics and crosses, downward arrows and diamonds representing the two-step decomposition of $NaNO_3$, the onset temperature of NASICON crystallization and the melting temperature of NASICON, respectively.

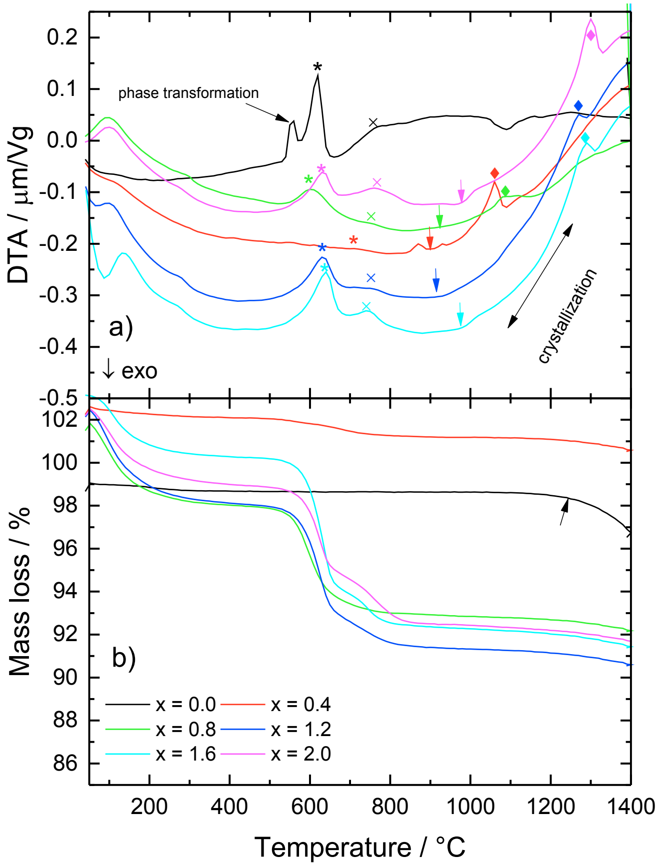

Fig. 5.25: Thermal analysis showing a) DTA and b) TG curves of $Na_{1+x}Zr_xSi_xPO_{(9x+6)/2}$.

Table 5.5: The temperatures of various thermodynamic events obtained from DTA/TG curves.

x	T_m ($NaNO_3$)	$T_{decomposition}$ ($NaNO_3$)	$T_{partial\ melting}$	T_{onset} (crystallization)	T_m (NASICON)
			^0C		
0	620	760	-	-	-
0.4	-	730	870 & 930	900	1060
0.8	600	750	-	920	1190
1.2	630	750	-	910	1270
1.6	640	750	-	970	1290
2.0	640	760	-	980	1300

5.2.6. Dilatometry

Dilatometry measurements were performed to identify the optimal sintering temperature of all the compositions. The results are shown in Fig. 5.26. All compositions were sintered at temperatures where shrinkage was 10 % ($T_{10\%}$) and 20 % ($T_{20\%}$) for one hour in air. These temperatures were obtained where the dilatometry curve intersects with the 10 % and 20 % shrinkage line respectively and are enlisted in Table 5.6.

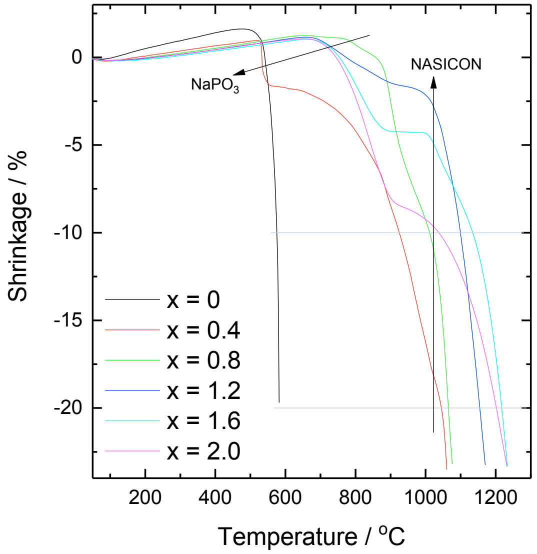

Fig. 5.26: Dilatometry of $Na_{1+x}Zr_xSi_xPO_{(9x+6)/2}$. Horizontal lines indicate $T_{10\%}$ and $T_{20\%}$.

For the composition where x = 0, a sharp shrinkage indicates melting, which was also supported by the heat treatments and thermal analysis at ~ 600 ºC. For the compositions $0.4 \leq x \leq 2.0$ a multiple stage shrinkage behavior is observed, confirming the composite nature of these compositions. Various phases in these composites are shrinking at different temperatures. The first shrinkage step indicates melting of $NaPO_3$, which was earlier seen from the XRD investigation. This phase forms a glass and is present in very small quantities that might be the reason why it remained undetected in the XRD investigation. The final shrinkage step occurs at temperatures > 1000 ºC, which corresponds to the shrinkage of the NASICON phase.

Table 5.6: List of $T_{20\%}$ and $T_{20\%}$ of $Na_{1+x}Zr_xSi_xPO_{(9x+6)/2}$.

x	**$T_{10\ \%}$ (ºC)**	**$T_{20\ \%}$ (ºC)**
0	576	581
0.4	925	1045
0.8	1010	1065
1.2	1100	1155
1.6	1135	1215
2.0	1040	1200

5.2.7. Microstructure

The cross-section of pellets after sintering at $T_{10\%}$ and $T_{20\%}$ by dilatometry are shown in Fig. 5.27 and Fig. 5.28, respectively. Sintering at higher temperature leads to higher density. Specimens sintered at 10 % shrinkage show minimal densification except when x = 0.8. However, all microstructures of $Na_{1+x}Zr_xSi_xPO_{(9x+6)/2}$ ($0 \leq x \leq 2$) sintered at 20 % shrinkage have similar porosity. Therefore impedance measurements on specimens with such comparable microstructures are reliable.

The specimen with x = 0.8 shows substantial densification even at 10 % shrinkage and the microstructure shows the presence of two phases. An EDX analysis revealed that dark grey phase contained no Si, more P and less Zr than the light grey phase. Quantitative analysis on the samples was not possible due to the electron beam sensitivity of these materials.

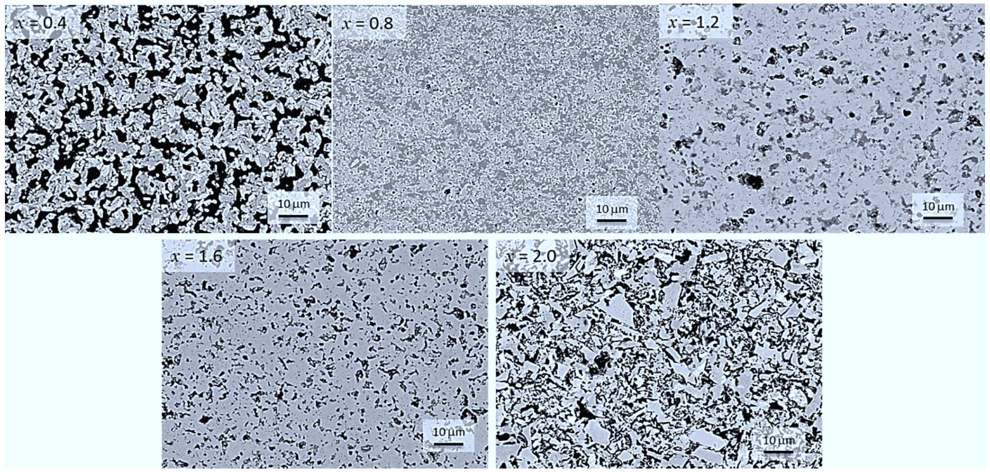

Fig. 5.27: Microstructure of $Na_{1+x}Zr_xSi_xPO_{(9x+6)/2}$ after sintering at temperature indicating the 10 % shrinkage. The EDX analysis revealed that dark grey phase contained no Si, more P and less Zr than the light grey phase.

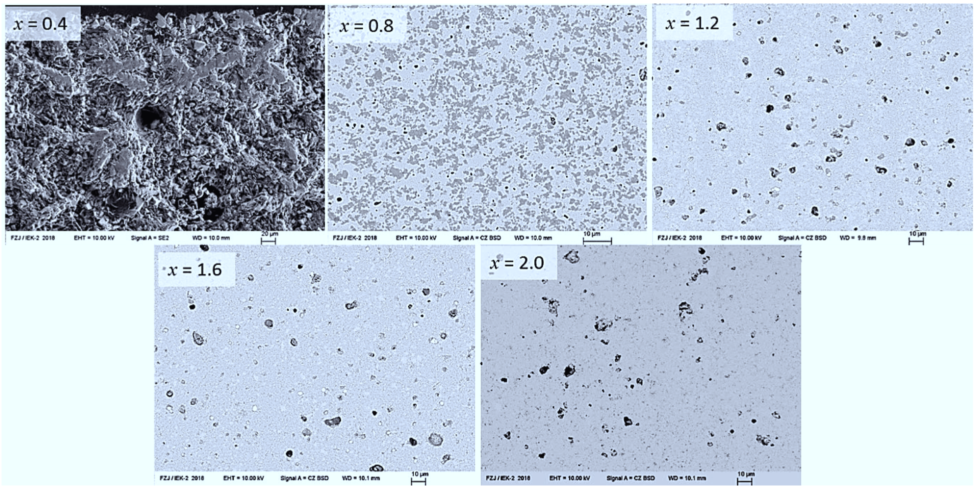

Fig. 5.28: Microstructure of $Na_{1+x}Zr_xSi_xPO_{(9x+6)/2}$ after sintering at temperature indicating the 20 % shrinkage. The sample $x = 0.4$ was unstable with polishing medium. (Images at different resolutions in Annex I)

5.2.8. Electrical Conductivity

The electrical conductivity results after sintering at both $T_{10\%}$ and $T_{20\%}$ are shown Fig. 5.29. The ionic conductivity of $NaPO_3$ glass is very low i.e., 0.007 mS cm^{-1} even at 200 ºC, as already reported in [233-236]. Among compositions 0.4 ≤ x ≤ 2.0, the conductivity is highest when x = 1.6. This is true for both sintering temperatures. In case of x = 0.4 and 0.8 sintered at 10 % shrinkage, a strong deviation from straigh line is observed. The deviation typically occurs at temperatures lower than 60 °C, where the adsorbed water within the pores of the material make them succeptible for proton conductivity [238, 243]. Because the composition with x = 0.4 is highly porous after sintering at 10 % shrinkage (see microstructure in Fig. 5.27), the water molecules get adsorbed at pore surfaces. Consequently, the proton conducting phenomenon is only observed at low temperatures where water is not evaporated. At temperutre > 60 °C, the adsorbed water gets desorbed and evaporated thus fades the influence of proton conduction. Hence, the true Arrhenius behavior of x = 0.4 is depicted by the grey line only in the temperature range of 60 – 100 °C.

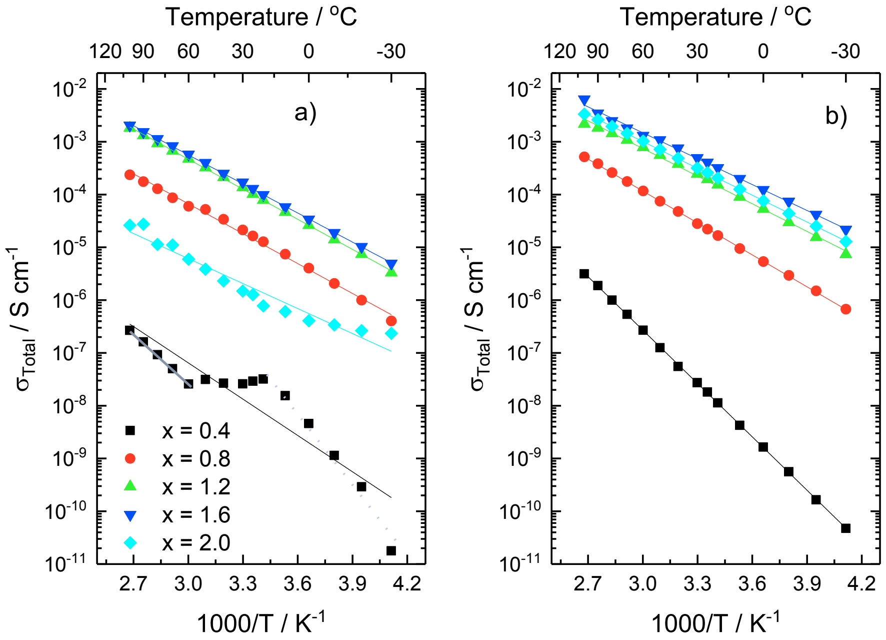

Fig. 5.29: Arrhenius plot of Na$_{1+x}$Zr$_x$Si$_x$PO$_{(9x+6)/2}$ from -30 °C to 100 °C after sintering at T$_{10\%}$ and T$_{20\%}$ in air.

The phenomen of proton conductivity is further confirmed by the E$_a$ comparison shown in Fig. 5.30a, where the correct E$_a$ of x = 0.4 is only indicated by the slope of solid grey line in the temperature range of 60 – 100 °C. Because the adsorbed water gets desorbed at temperatures ≥ 60 °C, therefore it also annihilates the proton conduction phenomenon. This phenomenon is reported to occur at temperatures as low as 25 °C [244, 245]. It is confirmed by a similar values of the activation energies of porous (0.63 eV) and dense samples (0.66 eV) of $x = 0.4$, sintered at $T_{10\%}$ and $T_{20\%}$ respectively (Fig. 5.30).

For other compositions when $0.8 \leq x \leq 2.0$, the E_a data indicate a decreasing trend when x was raised. The E_a values of these compositions are within the range 0.29 – 0.40 eV, which is similar to the literature values of NASICON structure [184, 185]. This reconfirms that the Na^+ ion conduction is mainly occuring throught the NASICON structure.

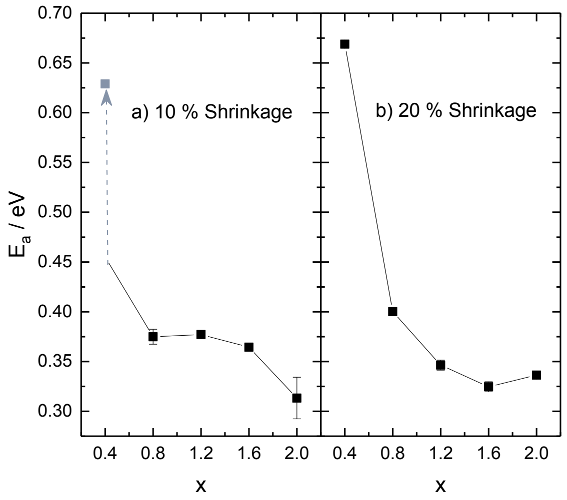

Fig. 5.30: $E_{a,\,Total}$ of $Na_{1+x}Zr_xSi_xPO_{(9x+6)/2}$ obtained from the slope of Arrhenius plot shown in Fig. 5.29. The grey value in a) represents the E_a only in the temperature range of 60 – 100 °C.

Conductivity at 25 °C increases with increasing x in $Na_{1+x}Zr_xSi_xPO_{(6x+6)/2}$. The results are not surprising since charge carrier concentration (Na content) is increased with x, as long as NASICON is considered, which facilitates sodium conduction in the structure. The highest conductivity was observed when $x = 1.6$ that was sintered at $T_{20\%}$. It exists as $Na_3Zr_2Si_2PO_{12}$ with ZrO_2 as secondary phase after 900 °C, nevertheless the conductivities of compositions with $1.2 \leq x \leq 2.0$ are in a similar range.

It is important to mention here that the relative density calculations after different heat treatments was not posible because the theoretical density of these stoichiometries was unknown. However, it is possible to get a visual overview of the densities of these ceramics from their microstructure. Furthermore, XRD results confirmed that more than one phases are present after the heat treatments, which categorizes these materials as composites and obtaining the theoretical density was rather unnecessary. Therefore, focus was first devoted to achieve a high conductive composition processed at low temperatures and then to perform deeper investigation of theoretical density on selected compositions.

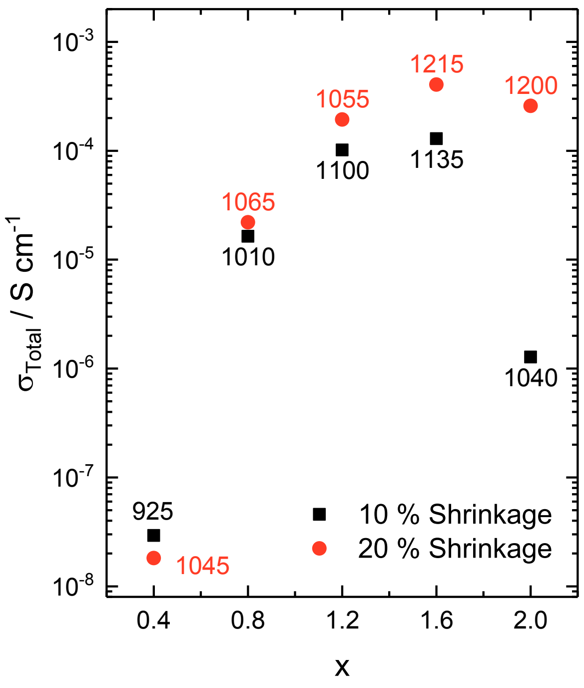

Figure 5.31: σ_{Total} as a function of x in $Na_{1+x}Zr_xSi_xPO_{(9x+6)/2}$ at 25 °C. Their respective sintering temperatures in °C are also given.

With the objective of producing the Na^+ ion conducting materials with low processing temperatures, this study has indeed opened new doors. Since the processing temperature was being reduced by changing the glassy phase content in the material therefore it was expected that the reduction in the sintering temperature would come with a compromise in the conductivity. The highest conducting NASICON has a conductivity of $4 \cdot 10^{-3}$ S cm^{-1} and a processing temperature of 1280 °C for 5 h [93] and the original NASICON with composition NZSiP gives a high conductivity of $8 \cdot 10^{-4}$ S cm^{-1} when sintered at 1250 °C for 10 h (section 4.2). Other studies reported the conductivity of original NZSiP as low as $9.2 \cdot 10^{-5}$ S cm^{-1}. Here a material was produced with conductivity in the range of 10^{-4} S cm^{-1} and a reduction of the sintering temperature by 200 °C.

To fabricate an all-solid-state battery, it is a common understanding that the processing temperature of the electrolyte must be reduced below 1000 °C so that electrolyte and cathode can be sintered together [246, 247]. In this case, sintering at 925 °C ($x = 0.4$) would give conductivity of $2.9 \cdot 10^{-8}$ S cm^{-1}, which might be too low for battery operation. However, in case of $x = 0.8$, a reasonable conductivity of $1.6 \cdot 10^{-5}$ S cm^{-1} can be obtained after sintering at 1010 °C. Nevertheless, to achieve materials with conductivity in the 10^{-4} S cm^{-1} range, the minimum temperature that can be reached among these compositions is 1100 ºC. For a successful application in an all-solid state battery, more work is nevertheless required to enhance the conductivity further and minimize the sintering temperature below 1000 ºC.

This study not only reduced significantly the processing temperature as compared to the original NASICON composition, but also opens a new prospect of exploring the quaternary phase diagram of Na_2O – SiO_2 – ZrO_2 – P_2O_5. For example, in this study we have chosen the $Na_2O \cdot P2O_5$ ($NaPO_3$) as the end member. A similar study could also be performed towards the $Na_2O \cdot SiO_2$ ($Na_2Si_2O_5$) direction.

Table 5.7: Table summarizing the conductivities at 25 ºC of $Na_{1+x}Zr_xSi_xPO_{(9x+6)/2}$ at reduced processing temperatures

x	10 % shrinkage		20 % shrinkage	
	Temperature / ºC	σ_{Total} / S cm^{-1}	Temperature / ºC	σ_{Total} / S cm^{-1}
0.0	576	-	581	-
0.4	925	$2.9 \cdot 10^{-8}$	1045	$1.8 \cdot 10^{-8}$
0.8	1010	$1.6 \cdot 10^{-5}$	1065	$2.2 \cdot 10^{-5}$
1.2	1100	$1.0 \cdot 10^{-4}$	1055	$1.9 \cdot 10^{-4}$
1.6	1135	$1.3 \cdot 10^{-4}$	1215	$4.0 \cdot 10^{-4}$
2.0	1040	$1.3 \cdot 10^{-4}$	1200	$2.6 \cdot 10^{-4}$

Chapter 6: Summary and conclusions

In this PhD work, the focus was to obtain an optimized sodium ion conducting material for application in an all-solid-state sodium ion battery. Among various available options, NASICON-type material was selected. A detailed study of optimizing the synthesis, processing, design and composition of these materials was performed. A summary of the results of these studies are concluded below.

SA-SSR method has been developed for the synthesis of NASICON-type materials. The method is convenient, low-cost, and has potential for large scale production. The impedance spectroscopy at 25 °C has shown that the total conductivity of an SA-SSR sample is 1×10^{-3} S cm^{-1}, which is one of the highest values of reported results with same composition applying conventional processing methods. For comparison, the total conductivity of a Pechini sample in this study is 8×10^{-4} S cm^{-1} at 25 °C. The reason of higher total conductivity of the SA-SSR samples compared to other preparation methods is explained by the powder characteristics, ceramic microstructure and stoichiometry. The SA-SSR method produces homogeneous water-based cationic mixture. As a result of this mixing at the atomic level and due to the differences (accidental) in the stoichiometry, a low amount of ZrO_2 as secondary phase is obtained for the SA-SSR powders. It also improves sinterability that results in larger grain size of SA-SSR ceramic, and consequently reduces the grain boundary resistance. Therefore, the higher conductivity of ceramics prepared by SA-SSR powder is due to a synergetic effect of aforementioned factors that mainly affects the grain boundary resistance of the ceramics. Since only little work has been devoted to material properties of nonstoichiometric NASICON materials [170], investigations were carried out in order to explore in more detail the impact of silicon deficiency on the ionic conduction of NASICON materials.

The conductivity of NASICON materials is dependent on processing conditions and synthesis. The heat treatment or sintering conditions control the microstructure. Grain and grain boundary resistance can be controlled by tuning the microstructure. Sintering at higher temperature leads to a better densification, whilst prolonging the sintering time leads to grain growth. Higher densification and larger grains result in smaller grain boundary resistance and, as a consequence, high conductance. The recommended sintering conditions are 1250 °C for 10 h in air, starting with a green density of ~ 60 %. The activation energy data show that sodium ion conduction through the bulk is easier than through the grain boundaries. The activation energy of grain boundary conductivity is higher at a sintering temperature of 1250 °C than at 1200 °C. However, the influence of grain boundary conductivity is so low with respect to the total conductivity that it is unnoticeable in the Arrhenius plots. Grain boundary complexion is affected by both sintering time and temperature. A systematic study of more sintering time and temperature would allow develop a time-temperature-transition diagram, which would allow obtaining a predictable microstructure by implementing the knowledge of grain boundary complexions.

The processing conditions of NASICON are nevertheless very harsh especially if they are sintered in the form of thin sheets e.g. as cast tapes. These materials undergo severe Na loss due to the evaporation of sodium oxide and results in a complete decomposition of the NASICON at the surface. Therefore NASICON material prepared with excess of Na with compositions $Na_{3+x}Zr_2Si_2PO_{12}$ with $0 \leq x \leq 0.4$ and exposed them to the sintering conditions of NASICON to study the Na loss. The Na loss occurs after the material is exposed to 1250 °C for more than 3 h, and in order to achieve the accurate stoichiometric NASICON composition one must start with Na excess of 0.2 moles i.e., $Na_{3.2}Zr_2Si_2PO_{12}$. This composition not only becomes stoichiometric in terms of Na content after sintering but also gives the highest bulk conductivity of $1.6 \cdot 10^{-3}$ S cm^{-1}. With this study, we also confirmed a reduction in E_a with the increase of Na charge carriers in the range of 3.0 – 3.4 moles per formula unit [93, 188, 189].

A novel NASICON solid solution $Na_{1+2x+y}Al_xY_xZr_{2-2x}(SiO_4)_y(PO_4)_{3-y}$ NAYZP$_x$ (y = 0) and NAYZSiP$_x$ (y = 2) was reported, which was designed based on the guidelines highlighted by Guin and Tietz [91] for producing a high conductive NASICONs. These guidelines were verified earlier by a high conductivity of 0.8 mS cm^{-1} in the series NSSiP$_x$ [188] and 4 mS cm^{-1} in the series NSZSiP$_x$ [93]. In our case, despite fulfilling all the three guidelines in NAYZSiP$_x$ system, i.e. mean arithmetic cationic radii ~ 0.72 Å, increasing Na content with x and monoclinic distortion in the structure, the electrical performance of NASICON materials is diminishing by increasing the Al/Y substitution. In contrast to other two series reported previously, the ionic conductivity of NAYZSiP$_x$ decreases with increasing (Al/Y) content. In addition, the width of the solid solution is also limited to x = 0.3, i.e. when the Na content per formula unit is 3.6. The study reveals that even if steric interactions are kept almost constant using the same mean effective radii (~ 0.72 Å), the increasing dissimilarity of the cations involved in all three series, from Sc-Sc in NSSiP$_x$, and Sc-Zr in NSZSiP$_x$ to (Al/Y)-Zr in NAYZSiP$_x$, evidence a significant impact on ionic conductivity. Therefore, the atomic orbitals of transition metal cations in the polyanionic sub-lattice also appear to have a strong influence on the transport properties of the Na^+ ions. NAYZP$_x$ crystallizes in the rhombohedral NASICON structure and reaches its solubility limit when $x = 0.3$. For $x > 0.3$, $AlPO_4$ and YPO_4 dominate amongst the XRD reflections. This is due to de-mixing of the substituents from the NASICON structure and subsequently unfavorable site occupancy, especially for Al^{3+} ions due to their small ionic radius chosen for the octahedral lattice site. NAYZSiP$_x$ crystallizes in the monoclinic modification when $0 \leq x \leq 0.1$, and in the rhombohedral form for x > 0.1. It exhibited a similar microstructure but an increasing ZrO_2 content with increasing x. The crystallographic unit cell of NAYZP$_x$ expands uniformly in a and c directions with increasing x, whereas NAYZSiP$_x$ expands in the a direction and shrinks in the c direction. The coefficient of thermal expansion of NAYZSiP$_x$ obtained from HT-XRD increased when x was raised from $4.1 \cdot 10^{-6}$ K^{-1} to $8.1 \cdot 10^{-6}$ K^{-1}.

Finally, in order to realize an all-solid-state battery, an attempt was made to design and produce an electrolyte material with a low processing temperature of, preferably, < 1000 °C. To achieve that, the quaternary phase diagram of $Na_2O – SiO_2 – ZrO_2 – P_2O_5$ was explored and a series of compositions was designed with one end at the $Na_2O \cdot P_2O_5$ edge and the other one at original NASICON located at the center. The compositions can be generalized with the formula $Na_{1+x}Zr_xSi_xPO_{(9x+6)/2}$, where x varied between $0 \le x \le 2.0$. The best composition in terms of reduced sintering temperature with a reasonable ionic conductivity was when $x = 1.2$, it has a conductivity of $1 \cdot 10^{-4}$ S cm^{-1} after sintering at 1100 ºC. Even though this investigation could not reach its objective of preparing a highly conductive electrolyte with processing temperature < 1000 ºC, it has however opened new prospects of further exploring the quaternary phase diagram of $Na_2O - SiO_2 - ZrO_2 - P_2O_5$. For example, one could also perform a similar study towards the $Na_2O \cdot SiO_2$ ($Na_2Si_2O_5$) edge.

References

1. Larcher, D. and J.M. Tarascon, *Towards greener and more sustainable batteries for electrical energy storage.* Nature Chemistry, 2015. **7**(1): p. 19-29.
2. Nayak, P.K., L. Yang, W. Brehm, and P. Adelhelm, *From Lithium-Ion to Sodium-Ion Batteries: Advantages, Challenges, and Surprises.* Angewandte Chemie International Edition, 2018. **57**(1): p. 102-120.
3. Mahmoudzadeh Andwari, A., A. Pesiridis, S. Rajoo, R. Martinez-Botas, and V. Esfahanian, *A review of Battery Electric Vehicle technology and readiness levels.* Renewable and Sustainable Energy Reviews, 2017. **78**: p. 414-430.
4. Blomgren, G.E., *The Development and Future of Lithium Ion Batteries.* Journal of The Electrochemical Society, 2017. **164**(1): p. A5019-A5025.
5. Peters, J., D. Buchholz, S. Passerini, and M. Weil, *Life cycle assessment of sodium-ion batteries.* Energy & Environmental Science, 2016. **9**(5): p. 1744-1751.
6. Wood, D.L., III, J. Li, and C. Daniel, *Prospects for reducing the processing cost of lithium ion batteries.* Journal of Power Sources, 2014. **275**: p. 234-242.
7. Muller, R., *Miners eye Europe's largest lithium deposit in Czech Republic*. 2017, Reuters.
8. A. Thielmann, A.S., M.Wietschel, *Gesamt-Roadmap Energiespeicher für die Elektromobilität 2030.* Fraunhofer-InstituteISI, Karlsruhe, 2015.
9. Palomares, V., P. Serras, I. Villaluenga, K.B. Hueso, J. Carretero-González, and T. Rojo, *Na-ion batteries, recent advances and present challenges to become low cost energy storage systems.* Energy & Environmental Science, 2012. **5**(3): p. 5884-5901.
10. Ellis, B.L. and L.F. Nazar, *Sodium and sodium-ion energy storage batteries.* Current Opinion in Solid State and Materials Science, 2012. **16**(4): p. 168-177.
11. Kummer, J.T. and N. Weber, *Battery having a Molten Alkali Metal Anode and Molten Sulfur Cathode*. 1968.
12. Kundu, D., E. Talaie, V. Duffort, and L.F. Nazar, *The Emerging Chemistry of Sodium Ion Batteries for Electrochemical Energy Storage.* Angewandte Chemie International Edition, 2015. **54**: p. 3431-3448.
13. Oshima, T. and M. Kajita, *Development of Sodium-Sulfur Batteries.* International Journal of Applied Ceramic Technology, 2004(3): p. 269-276.
14. Kato, T., *NAS Battery Fire Incident and Response*, in *NGK News*. 2011: NGK INSULATORS, LTD.
15. Sudworth, J.L., *The sodium/nickel chloride (ZEBRA) battery.* Journal of Power Sources, 2001. **100**: p. 149-163.
16. Böhm, H. and G. Beyermann, *ZEBRA Batteries, enhanced power by doping.* Journal of Power Sources, 1999. **84**: p. 270-274.
17. Galloway, R.C. and S. Haslam, *The ZEBRA electrc vehicle battery: power and energy improvements.* Journal of Power Sources, 1999. **80**: p. 164-170.
18. Javadi, T. and A. Petric, *Thermodynamic Analysis of Reaction Products Observed in ZEBRA Cell Cathodes.* Journal of the Electrochemical Society, 2011. **158**(6): p. 700-704.
19. Coors, W.G., C. Boxley, M. Robins, and A. Eccleston, *Low temperature molten sodium secondary cell with sodium ion conductive electrolyte membrane*. 2012.
20. Barker, J., *Condensed polyanion electrode*, F. Ltd, Editor. 2013.
21. http://www.faradion.co.uk/technology/sodium-ion-technology/ *(March 10, 2018).*

22. Lalère, F., J.B. Leriche, M. Courty, S. Boulineau, V. Viallet, C. Masquelier, and V. Seznec, *An all-solid state NASICON sodium battery operating at 200°C.* Journal of Power Sources, 2014. **247**: p. 975-980.
23. Delaizir, G., V. Viallet, A. Aboulaich, R. Bouchet, L. Tortet, V. Seznec, M. Morcrette, J.-M. Tarascon, P. Rozier, and M. Dollé, *The Stone Age Revisited: Building a Monolithic Inorganic Lithium-Ion Battery.* Advanced Functional Materials, 2012. **22**(10): p. 2140-2147.
24. Hueso, K.B., M. Armand, and T. Rojo, *High temperature sodium batteries: status, challenges and future trends.* Energy & Environmental Science, 2013. **6**(3): p. 734-749.
25. Kim, J.J., K. Yoon, I. Park, and K. Kang, *Progress in the Development of Sodium-Ion Solid Electrolytes.* Small Methods, 2017. **1**(10).
26. Coors, W.G., J.H. Gordon, and S.G. Menzer, *Electrochemical cell comprising ionically conductive membrane and porous multiphase electrode*. (2010), US Patent No. 2010/0297537 A1.
27. Susman, S., L. Boehm, K.J. Volin, and C.J. Delbecq, *A new method for the preparation of fast-conducting, reactive glass systems.* Solid State Ionics, 1981. **5**(C): p. 667-669.
28. Hooper, A., *A study of the electrical properties of single-crystal and polycrystalline β-alumina using complex plane analysis.* Journal of Physics D: Applied Physics, 1977. **10**(11): p. 1487-1496.
29. Bohnke, O., S. Ronchetti, and D. Mazza, *Conductivity measurements on nasicon and nasicon-modified materials.* Solid State Ionics, 1999. **122**(1–4): p. 127-136.
30. Jansen, M. and U. Henseler, *Synthesis, structure determination, and ionic conductivity of sodium tetrathiophosphate.* Journal of Solid State Chemistry, 1992. **99**(1): p. 110-119.
31. Yao, W. and S.W. Martin, *Ionic conductivity of glasses in the* $MI + M_2S + (0.1Ga_2S_3 + 0.9GeS_2)$ *system (M = Li, Na, K and Cs).* Solid State Ionics, 2008. **178**(33-34): p. 1777-1784.
32. Ribes, M., B. Barrau, and J.L. Souquet, *Sulfide glasses: Glass forming region, structure and ionic conduction of glasses in* Na_2S□XS_2 *(X□Si; Ge),* Na_2S□P_2S_5 *and* Li_2S□GeS_2 *systems.* Journal of Non-Crystalline Solids, 1980. **38-39**(PART 1): p. 271-276.
33. Coors, W.G., J.H. Gordon, and S.G. Menzer, *Electrochemical cell comprising ionically conductive membrane and porous multiphase electrode*, in *US Patent No. 2010/0297537 A1*. 2010.
34. Bohnke, O., S. Ronchetti, and D. Mazza, *Conductivity measurements on nasicon and nasicon-modified materials.* Solid State Ionics, 1999. **122**: p. 127-136.
35. Hayashi, A., K. Noi, A. Sakuda, and M. Tatsumisago, *Superionic glass-ceramic electrolytes for room-temperature rechargeable sodium batteries.* Nature Communications, 2012. **3**: p. 1-5.
36. Ni'mah, Y.L., M.-Y. Cheng, J.H. Cheng, J. Rick, and B.-J. Hwang, *Solid-state polymer nanocomposite electrolyte of* $TiO_2/PEO/NaClO_4$ *for sodium ion batteries.* Journal of Power Sources, 2015. **278**: p. 375-381.
37. Zhu, X., R. Zhao, W. Deng, X. Ai, H. Yang, and Y. Cao, *An All-solid-state and All-organic Sodium-ion Battery based on Redox-active Polymers and Plastic Crystal Electrolyte.* Electrochimica Acta, 2015. **178**: p. 55-59.
38. Kim, J.-K., Y.J. Lim, H. Kim, G.-B. Cho, and Y. Kim, *A hybrid solid electrolyte for flexible solid-state sodium batteries.* Energy & Environmental Science, 2015. **8**: p. 3589-3596.

39. Tietz, F., J. Koepke, and W. Urland, *Analytical investigations of β-Al_2O_3 and β''-Al_2O_3 crystals.* Journal of Crystal Growth, 1992. **118**(3): p. 314-318.

40. Briant, J.L. and G.C. Farrington, *Ionic conductivity in Na^+, K^+, and Ag^+ β''-alumina.* Journal of Solid State Chemistry, 1980. **33**(3): p. 385-390.

41. Youngblood, G.E., G.R. Miller, and R.S. Gordon, *Relative Effects of Phase Conversion and Grain Size on Sodium Ion Conduction in Polycrystalline, Lithia-Stabilized β-Alumina.* Journal of the American Ceramic Society, 1978. **61**(1-2): p. 86-87.

42. Sudworth, J.L., *The sodium sulfur battery / J.L. Sudworth and A.R. Tilley*, ed. A.R. Tilley. 1985, London ; New York: Chapman & Hall.

43. Baffier, N., J.C. Badot, and P. Colomban, *Conductivity of ion rich β and β'' alumina: Sodium and potassium compounds.* Materials Research Bulletin, 1981. **16**(3): p. 259-265.

44. Virkar, A.V., G.R. Miller, and R.S. Gordon, *Resistivity-Microstructure Relations in Lithia-Stabilized Polycrystalline β”-Alumina.* Journal of the American Ceramic Society, 1978. **61**(5-6): p. 250-252.

45. Ray, A.K. and E.C. Subbarao, *Synthesis of sodium β and β'' alumina.* Materials Research Bulletin, 1975. **10**(6): p. 583-590.

46. Wei, X., Y. Cao, L. Lu, H. Yang, and X. Shen, *Synthesis and characterization of titanium doped sodium beta"-alumina.* Journal of Alloys and Compounds, 2011. **509**(21): p. 6222-6226.

47. Schaefer, G.W. and W. Weppner, *Preparation of polycrystalline divalent beta alumina ceramics by ion exchange from K- and Na-beta"-alumina polycrystals.* Mechanical and corrosion properties. Series A, Key engineering materials, 1991. **59-60**: p. 145-154.

48. Morgan, P.E.D., *Low temperature synthetic studies of beta-aluminas.* Materials Research Bulletin, 1976. **11**(2): p. 233-241.

49. Sartori, S., A. Martucci, A. Muffato, and M. Guglielmi, *Sol-gel synthesis of Na^+ beta-Al_2O_3 powders.* Journal of the European Ceramic Society, 2004. **24**(6): p. 911-914.

50. Zaharescu, M., C. Pârlog, V. Stancovschi, D. Crişan, A. Brăileanu, and T. Surdeanu, *The influence of the powders synthesis method on the microstructure of lanthanum-stabilized β-alumina ceramics.* Solid State Ionics, 1985. **15**(1): p. 55-60.

51. Yamaguchi, S., K. Terabe, Y. Iguchi, and A. Imai, *Formation and crystallization of beta-alumina from precursor prepared by sol-gel method using metal alkoxides.* Solid State Ionics, 1987. **25**(2-3): p. 171-176.

52. Jayaraman, V., T. Gnanasekaran, and G. Periaswami, *Low-temperature synthesis of β-aluminas by a sol-gel technique.* Materials Letters, 1997. **30**(2-3): p. 157-162.

53. Yoldas, B.E. and D.P. Partlow, *Formation of continuous beta alumina films and coatings at low temperatures.* American Ceramic Society Bulletin, 1980. **59**(6): p. 640-642.

54. Pekarsky, A. and P.S. Nicholson, *Relative stability of spray-frozen/freeze-dried beta double prime -Al_2O_3 powders.* Materials Research Bulletin, 1980. **15**(10): p. 1517-1524.

55. Wang, Z., X. Li, and Z. Feng, *The effect of CTAB on the citrate Sol-gel process for the synthesis of sodium beta-alumina Nano-powders.* Bulletin of the Korean Chemical Society, 2011. **32**(4): p. 1310-1314.

56. Hodge, J.D., *Powder processing and crystallization of beta and beta double prime aluminas.* American Ceramic Society Bulletin, 1983. **62**(2): p. 244-248.

57. Takahashi, T. and K. Kuwabara, *β-Al_2O_3 synthesis from m-Al_2O_3.* Journal of Applied Electrochemistry, 1980. **10**(3): p. 291-297.

58. Sutorik, A.C., S.S. Neo, D.R. Treadwell, and R.M. Laine, *Synthesis of ultrafine β"-alumina powders via flame spray pyrolysis of polymeric precursors.* Journal of the American Ceramic Society, 1998. **81**(6): p. 1477-1486.

59. Lin, J., Z. Wen, X. Wang, S. Song, and Y. Liu, *Mechanochemical synthesis of Na-β/β"-Al_2O_3.* Journal of Solid State Electrochemistry, 2010. **14**(10): p. 1821-1827.

60. Park, H.C., Y.B. Lee, S.G. Lee, C.H. Lee, J.K. Kim, S.S. Hong, and S.S. Park, *Synthesis of beta-alumina powders by microwave heating from solution-derived precipitates.* Ceramics International, 2005. **31**(2): p. 293-296.

61. Armstrong, R.D., T. Dickinson, and P.M. Willis, *The A.C. impedance of single crystal sodium β-alumina.* Journal of Electroanalytical Chemistry and Interfacial Electrochemistry, 1976. **67**(1): p. 121-122.

62. Fielder, W.L., H.E. Kautz, J.S. Fordyce, and J. Singer, *Conductivity of Boules of Single-Crystal Sodium Beta-Alumina.* Journal of The Electrochemical Society, 1975. **122**(4): p. 528-530.

63. Yung-Fang Yu, Y. and J.T. Kummer, *Ion exchange properties of and rates of ionic diffusion in beta-alumina.* Journal of Inorganic and Nuclear Chemistry, 1967. **29**(9): p. 2453-2475.

64. Whittingham, M.S. and R.A. Huggins, *Measurement of Sodium Ion Transport in Beta Alumina Using Reversible Solid Electrodes.* The Journal of Chemical Physics, 1971. **54**(1): p. 414-416.

65. Engstrom, H., J.B. Bates, and J.C. Wang, *Non-Debye capacitance in single-crystal sodium beta-alumina.* Solid State Communications, 1980. **35**(7): p. 543-546.

66. Engstrom, H., J.B. Bates, W.E. Brundage, and J.C. Wang, *Ionic conductivity of sodium beta"-alumina.* Solid State Ionics, 1981. **2**(4): p. 265-276.

67. Bates, J.B., H. Engstrom, J.C. Wang, B.C. Larson, N.J. Dudney, and W.E. Brundage, *Composition, ion-ion correlations and conductivity of beta"-alumina.* Solid State Ionics, 1981. **5**: p. 159-162.

68. Whalen, T.J., G.J. Tennenhouse, and C. Meyer, *Relation of Properties to Microstructure in β"-Alumina Ceramic.* Journal of the American Ceramic Society, 1974. **57**(11): p. 497-498.

69. Virkar, A.V., J.F. Jue, and K.Z. Fung, *Alkali-metal-β- and β"-alumina and gallate polycrystalline ceramics and fabrication by a vapor phase method*. 2000, Google Patents.

70. Parthasarathy, P., N. Weber, and A.V. Virkar. *High temperature sodium - Zinc chloride batteries with sodium beta" - alumina solid electrolyte (BASE)*. in *ECS Transactions*. 2007.

71. Lu, X., J.P. Lemmon, V. Sprenkle, and Z. Yang, *Sodium-beta alumina batteries: Status and challenges.* JOM, 2010. **62**(9): p. 31-36.

72. Heavens, S.N., *Strength improvement in beta" alumina by incorporation of zirconia.* Journal of Materials Science, 1988. **23**(10): p. 3515-3518.

73. Green, D.J., *Transformation toughening and grain size control in β"-Al_2O_3/ZrO_2 composites.* Journal of Materials Science, 1985. **20**(7): p. 2639-2646.

74. Binner, J.G.P. and R. Stevens, *Improvement in the mechanical properties of polycrystalline beta-alumina via the use of zirconia particles containing stabilizing oxide additions.* Journal of Materials Science, 1985. **20**(9): p. 3119-3124.

75. Anantharamulu, N., K. Koteswara Rao, G. Rambabu, B. Vijaya Kumar, V. Radha, and M. Vithal, *A wide-ranging review on Nasicon type materials.* Journal of Materials Science, 2011. **46**(9): p. 2821-2837.

76. Mohan, V.M., V. Raja, P.B. Bhargav, A.K. Sharma, and V.V.R.N. Rao, *Structural, electrical and optical properties of pure and NaLaF4 doped PEO polymer electrolyte films.* Journal of Polymer Research, 2007. **14**(4): p. 283-290.

77. Gohel, K. and D.K. Kanchan, *Ionic transport studies in PVDF-HFP-PMMA-(PC+DEC)-*$LiClO_4$ *gel polymer electrolyte.* AIP Conference Proceedings, 2017. **1832**(1): p. 140047.

78. Kim, J.-K., Y.J. Lim, H. Kim, G.-B. Cho, and Y. Kim, *A hybrid solid electrolyte for flexible solid-state sodium batteries.* Energy & Environmental Science, 2015. **8**(12): p. 3589-3596.

79. Zhu, Y.S., L.L. Li, C.Y. Li, L. Zhou, and Y.P. Wu, $Na_{1+x}Al_xGe_{2-x}P3O_{12}$ *(x=0.5) glass-ceramic as a solid ionic conductor for sodium ion.* Solid State Ionics, 2016. **289**: p. 113-117.

80. Tsuji, F., N. Tanibata, A. Sakuda, A. Hayashi, and M. Tatsumisago, *Preparation of Sodium Ion Conductive* $Na_{10}GeP_2S_{12}$ *Glass-ceramic Electrolytes.* Chemistry Letters, 2018. **47**(1): p. 13-15.

81. Foraison, D. and J.L. Souquet, *Electrochemical Study of Sodium Conductive Glass-Sodium Amalgam Interface.* Electrochimica Acta, 1978. **23**(5): p. 457-461.

82. Bloom, I. and M.C. Hash, *Ceramic Glass Electrolytes for Sodium-Ion-Conducting Applications.* Journal of the Electrochemical Society, 1992. **139**(4): p. 1115-1118.

83. Sobha, K.C. and K.J. Rao, *ac conductivity and transport studies in phosphate glasses with NASICON-type chemistry.* Solid State Ionics, 1995. **81**(1–2): p. 145-156.

84. Berbano, S.S., I. Seo, C.M. Bischoff, K.E. Schuller, and S.W. Martin, *Formation and structure of* $Na_2S+P_2S_5$ *amorphous materials prepared by melt-quenching and mechanical milling.* Journal of Non-Crystalline Solids, 2012. **358**(1): p. 93-98.

85. Hayashi, A., K. Noi, A. Sakuda, and M. Tatsumisago, *Superionic glass-ceramic electrolytes for room-temperature rechargeable sodium batteries.* Nature Communications, 2012. **3**.

86. Hong, H.Y.P., *Crystal structures and crystal chemistry in the system Na1+xZr2SixP3-xO12.* Materials Research Bulletin, 1976. **11**(2): p. 173-182.

87. Goodenough, J.B., H.Y.P. Hong, and J.A. Kafalas, *Fast* Na^+*-ion transport in skeleton structures.* Materials Research Bulletin, 1976. **11**(2): p. 203-220.

88. Catti, M., S. Stramare, and R. Ibberson, *Lithium location in NASICON-type Li+ conductors by neutron diffraction. I. Triclinic α'-LiZr2(PO4)3.* Solid State Ionics, 1999. **123**(1): p. 173-180.

89. Catti, M. and S. Stramare, *Lithium location in NASICON-type* Li^+ *conductors by neutron diffraction: II. Rhombohedral* α-$LiZr_2(PO_4)_3$ *at* $T = 423$ *K.* Solid State Ionics, 2000. **136-137**: p. 489-494.

90. Iglesias, J.E., J. Sanz, A. Martínez-Juárez, and J.M. Rojo, *Low-Temperature Triclinic Distortion in NASICON-Type LiSn2(PO4)3.* Journal of Solid State Chemistry, 1997. **130**(2): p. 322-326.

91. Guin, M. and F. Tietz, *Survey of the transport properties of sodium superionic conductor materials for use in sodium batteries.* Journal of Power Sources, 2015. **273**: p. 1056-1064.

92. Palomares, V., P. Serras, I. Villaluenga, K.B. Hueso, J. Carretero-González, and T. Rojo, *Na-ion batteries, recent advances and present challenges to become low cost energy storage systems.* Energy and Environmental Science, 2012. **5**(3): p. 5884-5901.

93. Ma, Q., M. Guin, S. Naqash, C.L. Tsai, F. Tietz, and O. Guillon, *Scandium-Substituted* $Na_3Zr_2(SiO_4)_2(PO_4)$ *Prepared by a Solution Assisted Solid-State Reaction*

Method as Sodium-Ion Conductors. Chemistry of Materials, 2016. **28**(13): p. 4821-4828.

94. http://www.ionotec.com/ *(January 12, 2016).*
95. Ignaszak, A., P. Pasierb, R. Gajerski, and S. Komornicki, *Synthesis and properties of Nasicon-type materials.* Thermochimica Acta, 2005. **426**(1–2): p. 7-14.
96. Yadav, P. and M.C. Bhatnagar, *Preparation, structure and conductivity of Sn modified NASICON material.* Journal of Electroceramics, 2013. **30**(3): p. 145-151.
97. Aatiq, A., *Synthesis and structural characterization of* $ASnFe(PO_4)_3$ *(A=* Na_2*,Ca,Cd) phosphates with the Nasicon type structure.* Powder Diffraction, 2004. **19**(3): p. 272-279.
98. Yadav, P. and M.C. Bhatnagar, *Structural studies of NASICON material of different compositions by sol-gel method.* Ceramics International, 2012. **38**(2): p. 1731-1735.
99. Aonot, H., K. Nishimura, N. Yamamoto, Y. Itagaki, and Y. Sadaoka, *Preparation of NASICON using sol-gel method and reactivity with alkali carbonate for potentiometric* CO_2 *gas sensor.* Sensor Letters, 2008. **6**(6): p. 979-982.
100. Ejehi, F., S.P.H. Marashi, M.R. Ghaani, and D.F. Haghshenas, *The synthesis of NaSICON-type ZrNb(PO 4) 3 structure by the use of Pechini method.* Ceramics International, 2012. **38**(8): p. 6857-6863.
101. Barre, M., M.P. Crosnier-Lopez, F. Le Berre, J. Emery, E. Suard, and J.L. Fourquet, *Room temperature crystal structure of* $La_{1/3}Zr_2(PO_4)_3$*, a NASICON-type compound.* Chemistry of Materials, 2005. **17**(26): p. 6605-6610.
102. Kotobuki, M., M. Koishi, and Y. Kato, *Preparation of* $Li_{1.5}Al_{0.5}Ti_{1.5}(PO_4)_3$ *solid electrolyte via a co-precipitation method.* Ionics, 2013. **19**(12): p. 1945-1948.
103. Shalini, S., P. Sandhyarani, Y.S. Rao, D. Chakravarty, and R. Subasri, *Wet chemical synthesis and characterization of* Na^+*-conducting sodium dysprosium silicates.* Ceramics International, 2012. **38**(1): p. 295-300.
104. Morimoto, H., M. Hirukawa, A. Matsumoto, T. Kurahayashi, N. Ito, and S.I. Tobishima, *Lithium ion conductivities of NASICON-type* $Li_{1+x}Al_xTi_{2-x}(PO_4)_3$ *solid electrolytes prepared from amorphous powder using a mechanochemical method.* Electrochemistry, 2014. **82**(10): p. 870-874.
105. Vijaya Kumar, B., R. Velchuri, G. Prasad, and M. Vithal, *Preparation, characterization, spectral and conductivity studies of* $Na_3MgZr(PO_4)_3$ *and* $Na_{0.1}(H_3O)_{2.9}MgZr(PO_4)_3$*.* Ceramics International, 2009. **35**(7): p. 2719-2725.
106. Orlova, A.I., A.K. Koryttseva, A.E. Kanunov, V.N. Chuvil'deev, A.V. Moskvicheva, N.V. Sakharov, M.S. Boldin, and A.V. Nokhrin, *Fabrication of* $NaZr_2(PO_4)_3$*-type ceramic materials by spark plasma sintering.* Inorganic Materials, 2012. **48**(3): p. 313-317.
107. Ignaszak, A., P. Pasierb, R. Gajerski, and S. Komornicki, *Synthesis and properties of Nasicon-type materials*.
108. Yamazoe, N., *Toward innovations of gas sensor technology.* Sensors and Actuators B: Chemical, 2005. **108**(1–2): p. 2-14.
109. Baliteau, S., A.L. Sauvet, C. Lopez, and P. Fabry, *Characterization of a NASICON based potentiometric* CO_2 *sensor.* Journal of the European Ceramic Society, 2005. **25**(12 SPEC. ISS.): p. 2965-2968.
110. Obata, K. and S. Matsushima, *Relationship between aging time and EMF change of potentiometric* CO_2 *device using* $Na_{1+x}Zr_2Si_xP_{3-x}O_{12}$ *(0 < x < 3).* Sensors and Actuators, B: Chemical, 2009. **139**(2): p. 435-439.
111. Cretin, M., H. Khireddine, and P. Fabry, *NASICON structure for alkaline ion recognition.* Sensors and Actuators, B: Chemical, 1997. **43**(1-3): p. 224-229.

112. Rodrigo, J.L. and J. Alamo, *Phase transition in NaSn2(PO4)3 and thermal expansion of NaMIV 2 (PO43; MIV = Ti, Sn, Zr.* Materials Research Bulletin, 1991. **26**(6): p. 475-480.
113. Winand, J.M., A. Rulmont, and P. Tarte, *Nouvelles solutions solides LI(MIV)$_{2-x}$(NIV)$_x$(PO$_4$)$_3$ (L = Li,Na M,N = Ge,Sn,Ti,Zr,Hf) synthèse et étude par diffraction x et conductivité ionique.* Journal of Solid State Chemistry, 1991. **93**(2): p. 341-349.
114. Aono, H. and E. Sugimoto, *Ionic conductivity and sinterability of NASICON-type ceramics: The systems NaM2(PO4)3 + yNa2O (M = Ge, Ti, Hf, and Zr).* Journal of the American Ceramic Society, 1996. **79**(10): p. 2786-2788.
115. Cava, R.J., E.M. Vogel, and D.W. Johnson, *Effect of Homovalent Framework Cation Substitutions on the Sodium Ion Conductivity in $Na_3Zr_2Si_2PO_{12}$.* Journal of the American Ceramic Society, 1982. **65**(9): p. c157-c159.
116. Vogel, E.M., R.J. Cava, and E. Rietman, *Na+ ion conductivity and crystallographic cell characterization in the Hf-nasicon system Na1+xHf2SixP3-xO12.* Solid State Ionics, 1984. **14**(1): p. 1-6.
117. Aono, H. and E. Sugimoto, *Ionic conductivity and sinterability of NASICON-type ceramics: The systems $NaM_2(PO_4)_{3+y}Na_2O$ (M = Ge, Ti, Hf, and Zr).* Journal of the American Ceramic Society, 1996. **79**(10): p. 2786-2788.
118. Kuriyama, N., T. Sakai, H. Miyamura, and H. Ishikawa, *Solid-state metal hydride batteries using tetramethylammonium hydroxide pentahydrate.* Solid State Ionics, 1992. **53–56, Part 1**(0): p. 688-693.
119. Dashjav, E. and F. Tietz, *Neutron diffraction analysis of NASICON-type $Li_{1+x}Al_xTi_{2-X}P_3O_{12}$.* Zeitschrift fur Anorganische und Allgemeine Chemie, 2014. **640**(15): p. 3070-3073.
120. Vogel, E.M., R.J. Cava, and E. Rietman, *Na^+ ion conductivity and crystallographic cell characterization in the Hf-nasicon system $Na_{1+x}Hf_2Si_xP_{3-x}O_{12}$.* Solid State Ionics, 1984. **14**(1): p. 1-6.
121. Losilla, E.R., M.A.G. Aranda, S. Bruque, M.A. París, J. Sanz, and A.R. West, *Understanding Na Mobility in NASICON Materials: A Rietveld, 23Na and 31P MAS NMR, and Impedance Study.* Chemistry of Materials, 1998. **10**(2): p. 665-673.
122. Naqash, S., Q. Ma, F. Tietz, and O. Guillon, *$Na_3Zr_2(SiO_4)_2(PO_4)$ prepared by a solution-assisted solid state reaction.* Solid State Ionics, 2017. **302**: p. 83-91.
123. Cowley, J.M., *Diffraction physics*. 1975.
124. Fultz, B. and J. Howe, *Transmission electron microscopy and diffractometry of materials*. 2008, Berlin: Springer.
125. Altomare, A., C. Giacovazzo, and A. Moliterni, *Chapter 7: Indexing and Space Group Determination*, in *Powder Diffraction : Theory and Practice*. 2008, Cambridge UK: Royal Society of Chemistry.
126. Petricek, V., M. Dusek, and L. Palatinus, *Crystallographic computing system JANA2006: General features.* Zeitschrift für Kristallographie, 2014. **229**(5): p. 345-352.
127. Rietveld, H.M., *A profile refinement method for nuclear and magnetic structures.* Journal of Applied Crystallography, 1969. **2**: p. 65-71.
128. Rietveld, H.M., *Line profiles of neutron powder-diffraction peaks for structure refinement.* Acta Crystallographica, 1967. **22**: p. 151-152.
129. Young, R.A., P.E. Mackie, and R.B.V. Dreele, *Application of Pattern-Fitting Structure-Refinement Method to X-Ray Powder Diffractometer Patterns.* Journal of Applied Crystallography, 1977. **10**: p. 262-269S.
130. Dreele, R.B.V., *Chapter 9: Rietveld Refinement*, in *Powder Diffraction: Theroy and Practice*. 2008, Cambridge UK: Royal Society of Chemistry.

131. Young, R.A., *The Rietveld Method* 1993, International Union of Crystallography Oxford University Press.
132. https://www.malvernpanalytical.com/en/products/technology/light-scattering/laser-diffraction *(April 15, 2018)*.
133. Mudroch, A., *Manual of Physico-Chemical Analysis of Aquatic Sediments*. 1997: Lewis Publishers.
134. Barsoukov, E. and J.R. Macdonald, *Impedance Spectroscopy Theory, Experiment and Applications* 2nd. edition. 2005: Wiley-Interscience.
135. Orazem, M.E. and B. Tribollet, *Electrochemical Impedance Spectroscopy*. 2008: John Wiley & Sons.
136. Ahmed, R. and K. Reifsnider, *Study of Influence of Electrode Geometry on Impedance Spectroscopy.* International Journal of Electrochemical Science, 2011. **6**: p. 1159-1174.
137. Orazem, M.E. and B. Tribollet, *Electrochemical Impedance Spectroscopy*. 2011: Wiley.
138. Irvine, J.T.S., D.C. Sinclair, and A.R. West, *Electroceramics: Characterization by Impedance Spectroscopy.* Advanced Materials, 1990. **2**(3): p. 132-138.
139. Reed, S.J.B., *Chapter 4: Scanning electron microscopy* in *Electron Microprobe Analysis and Scanning Electron Microscopy in Geology* 2006: Cambridge University Press.
140. *Standard Test Methods for Determining Average Grain Size*, in *ASTM Standard E112 - 2010*. 2010, ASTM International, West Conshohocken, PA.
141. Laye, P.G., *Chapter 3:Differential Thermal Analysis and Differential Scanning Calorimetry* in *Principles of Thermal Analysis and Calorimetry*, P. Haines, Editor. 2002: Cambridge, UK : Royal Society of Chemistry.
142. Maca, K., V. Pouchy, and R. Boccaccini, *Sintering Densification Curve – a Practical Approach for its Construction from Dilatometric Shrinkage Data* Science of Sinering, 2008. **40**: p. 117-122.
143. Takahashi, T., K. Kuwabara, and M. Shibata, *Conductivities of* Na^+ *ion conductors based on NASICON.* Solid State Ionics, 1980. **1**(3–4): p. 163-175.
144. Essoumhi, A., C. Favotto, M. Mansori, and P. Satre, *Synthesis and characterization of a NaSICON series with general formula* $Na_{2.8}Zr_{2-y}Si_{1.8-4y}P_{1.2+4y}O_{12}$ *(*$0 \leq y \leq 0.45$*).* Journal of Solid State Chemistry, 2004. **177**(12): p. 4475-4481.
145. Martucci, A., S. Sartori, M. Guglielmi, M.L. Di Vona, S. Licoccia, and E. Traversa, *NMR and XRD study of the influence of the P precursor in sol-gel synthesis of NASICON powders and films.* Journal of the European Ceramic Society, 2002. **22**(12): p. 1995-2000.
146. Wang, B., X.S. Liang, F.M. Liu, T.G. Zhong, C. Zhao, G.Y. Lu, and B.F. Quan, *Synthesis and characterization of NASICON nanoparticles by sol-gel method.* Chemical Research in Chinese Universities, 2009. **25**(1): p. 13-16.
147. Zhang, S., B. Quan, Z. Zhao, B. Zhao, Y. He, and W. Chen, *Preparation and characterization of NASICON with a new sol-gel process.* Materials Letters, 2004. **58**(1-2): p. 226-229.
148. Zhang, Z.Z., S.Q. Shi, Y.S. Hu, and L.Q. Chen, *Sol-gel synthesis and conductivity properties of sodium ion solid state electrolytes* $Na_3Zr_2Si_2PO_{12}$*.* Wuji Cailiao Xuebao/Journal of Inorganic Materials, 2013. **28**(11): p. 1255-1260.
149. Pechini, M.P., *Method of preparing lead and alkaline earth titanates and niobates and coating method using the same to form a capacitor*. 1967, US Patent No. 3,330,697.

150. Ejehi, F., S.P.H. Marashi, M.R. Ghaani, and D.F. Haghshenas, *The synthesis of NaSICON-type $ZrNb(PO_4)_3$ structure by the use of Pechini method.* Ceramics International, 2012. **38**(8): p. 6857-6863.
151. Gordon, R.S., G.R. Miller, B.J. McEntire, E.D. Beck, and J.R. Rasmussen, *Fabrication and characterization of Nasicon electrolytes.* Solid State Ionics, 1981. **3**: p. 243-248.
152. Quon, D.H.H., T.A. Wheat, and W. Nesbitt, *Synthesis, characterization and fabrication of $Na_{1+x}Zr_2Si_xP_{3-x}O_{12}$.* Materials Research Bulletin, 1980. **15**(11): p. 1533-1539.
153. Kreuer, K.D., H. Kohler, U. Warhus, and H. Schulz, *NASICON solid electrolytes part III: Sodium conductivity enhancement along domain and grain boundaries.* Materials Research Bulletin, 1986. **21**(2): p. 149-159.
154. Boilot, J.P., J.P. Salanié, G. Desplanches, and D. Le Potier, *Phase transformation in $Na_{1+x}Si_xZr_2P_{3-x}O_{12}$ compounds.* Materials Research Bulletin, 1979. **14**(11): p. 1469-1477.
155. Clearfield, A., M.A. Subramanian, W. Wang, and P. Jerus, *The use of hydrothermal procedures to synthesize NASICON and some comments on the stoichiometry of NASICON phases.* Solid State Ionics, 1983. **9**: p. 895-902.
156. Clearfield, A., P. Jerus, and R.N. Cotman, *Proceedings of the International Conference on Fast Ionic Transport in SolidsHydrothermal and solid state synthesis of sodium zirconium silicophosphates.* Solid State Ionics, 1981. **5**: p. 301-304.
157. Li, Y., Y. Ling, X. Zou, and X. Bai, *Hydrothermal synthesis and characterization of crystal $NaZr_2(PO_4)_3$.* Xiyou Jinshu Cailiao Yu Gongcheng/Rare Metal Materials and Engineering, 2005. **34**(SUPPL. 1 PART 2): p. 871.
158. Di Vona, M.L., E. Traversa, and S. Licoccia, *Nonhydrolytic Synthesis of NASICON of Composition $Na_3Zr_2Si_2PO_{12}$: A Spectroscopic Study.* Chemistry of Materials, 2001. **13**(1): p. 141-144.
159. Fuentes, R.O., F.M. Figueiredo, M.R. Soares, and F.M.B. Marques, *Submicrometric NASICON ceramics with improved electrical conductivity obtained from mechanically activated precursors.* Journal of the European Ceramic Society, 2005. **25**(4): p. 455-462.
160. Dhas, N.A. and K.C. Patil, *Combustion synthesis and properties of the NASICON family of materials.* Journal of Materials Chemistry, 1995. **5**(9): p. 1463-1468.
161. Segal, D., *Chemical synthesis of ceramic materials.* Journal of Materials Chemistry, 1997. **7**(8): p. 1297-1305.
162. Hayashi, K., K. Shima, and F. Sugiyama, *A mixed aqueous/aprotic sodium/air cell using a NASICON ceramic separator.* Journal of the Electrochemical Society, 2013. **160**(9): p. A1467-A1472.
163. C. J. Brinker and G.W. Scherer, *Sol-Gel Science: the physics and chemistry of sol-gel processing*. 1st Edition (1990) 2-17: Academic Press Inc. .
164. Shimizu, Y., Y. Azuma, and S. Michishita, *Sol-gel synthesis of NASICON discs from aqueous solution.* Journal of Materials Chemistry, 1997. **7**(8): p. 1487-1490.
165. Lee, J.S., C.M. Chang, Y.I. Lee, J.H. Lee, and S.H. Hong, *Spark Plasma Sintering (SPS) of NASICON Ceramics.* Journal of the American Ceramic Society, 2004. **87**(2): p. 305-307.
166. Hong, H.Y.P., *Crystal structures and crystal chemistry in the system $Na_{1+x}Zr_2Si_xP_{3-x}O_{12}$.* Materials Research Bulletin, 1976. **11**(2): p. 173-182.
167. Wang, D., Y. Guo, K. Liang, and K. Tao, *Crystal structure of zirconia by Rietveld refinement.* Science in China Series A: Mathematics, 1999. **42**(1): p. 80.

168. Cherin, P., W.C. Hamilton, and B. Post, *Position and thermal parameters of oxygen atoms in sodium nitrate.* Acta Crystallographica, 1967. **23**(3): p. 455-460.
169. Nikolova, R.P., K. Fujiwara, N. Nakayama, and V. Kostov-Kytin, *Crystal structure of a new small-pore zirconosilicate* $Na_2ZrSi_2O_7{\cdot}H_2O$ *and its relation to stoichiometrically and topologically similar compounds.* Solid State Sciences, 2009. **11**(2): p. 382-388.
170. von Alpen, U., M.F. Bell, and H.H. Höfer, *Compositional dependence of the electrochemical and structural parameters in the Nasicon system* ($Na_{1+x}Si_xZr_2P_{3-x}O_{12}$). Solid State Ionics, 1981. **3-4**(C): p. 215-218.
171. Wu, Z. and M. Liu, *Modelling of ambipolar transport properties of composite mixed ionic-electronic conductors.* Solid State Ionics, 1996. **93**(1–2): p. 65-84.
172. Skarmoutsos, D., P. Nikolopoulos, F. Tietz, and I.C. Vinke, *Physical characterization of* $Y_{0.25}Zr_{0.60}Ti_{0.15}O_{2-x}$ *and its performance as a* $Ni/Y_{0.25}Zr_{0.60}Ti_{0.15}O_{2-x}$ *anode cermet in an SOFC.* Solid State Ionics, 2004. **170**(3): p. 153-158.
173. Hayashi, A., K. Noi, A. Sakuda, and M. Tatsumisago, *Superionic glass-ceramic electrolytes for room-temperature rechargeable sodium batteries.* Nature Communications, 2012. **3**: p. 856-860.
174. Foster, M.D., O.D. Friedrichs, R.G. Bell, F.A.A. Paz, and J. Klinowski, *Chemical evaluation of hypothetical uninodal zeolites.* Journal of the American Chemical Society, 2004. **126**(31): p. 9769-9775.
175. Kang, S.-J.L., *9 - Abnormal Grain Growth*, in *Sintering*. 2005, Butterworth-Heinemann: Oxford. p. 117-135.
176. Cantwell, P.R., M. Tang, S.J. Dillon, J. Luo, G.S. Rohrer, and M.P. Harmer, *Grain boundary complexions.* Acta Materialia, 2014. **62**(Supplement C): p. 1-48.
177. Cantwell, P.R., S. Ma, S.A. Bojarski, G.S. Rohrer, and M.P. Harmer, *Expanding time–temperature-transformation (TTT) diagrams to interfaces: A new approach for grain boundary engineering.* Acta Materialia, 2016. **106**(Supplement C): p. 78-86.
178. Haile, S.M., G. Staneff, and K.H. Ryu, *Non-stoichiometry, grain boundary transport and chemical stability of proton conducting perovskites.* Journal of Materials Science, 2001. **36**(5): p. 1149-1160.
179. Haile, S.M., D.L. West, and J. Campbell, *The role of microstructure and processing on the proton conducting properties of gadolinium-doped barium cerate.* Journal of Materials Research, 2011. **13**(6): p. 1576-1595.
180. Bonanos, N., B.C.H. Steele, and E.P. Butler, *Impedance Spectroscopy*. 1988: Wiley and Sons, New York, USA.
181. McLachlan, D.S., M. Blaszkiewicz, and R.E. Newnham, *Electrical Resistivity of Composites.* Journal of the American Ceramic Society, 1990. **73**(8): p. 2187-2203.
182. Uvarov, N.F., *Composite solid electrolytes: recent advances and design strategies.* Journal of Solid State Electrochemistry, 2011. **15**(2): p. 367-389.
183. Nan, C.-W. and D.M. Smith, *A.c. electrical properties of composite solid electrolytes.* Materials Science and Engineering: B, 1991. **10**(2): p. 99-106.
184. Khireddine, H., P. Fabry, A. Caneiro, and B. Bochu, *Optimization of NASICON composition for* Na^+ *recognition.* Sensors and Actuators B-Chemical, 1997. **40**(2-3): p. 223-230.
185. Ahmad, A., T.A. Wheat, A.K. Kuriakose, J.D. Canaday, and A.G. McDonald, *Dependence of the properties of Nasicons on their composition and processing.* Solid State Ionics, 1987. **24**(1): p. 89-97.
186. Fuentes, R.O., F.M. Figueiredo, F.M.B. Marques, and J.I. Franco, *Influence of microstructure on the electrical properties of NASICON materials.* Solid State Ionics, 2001. **140**(1-2): p. 173-179.

187. Krok, F., *Influence of sintering conditions on chemical composition of NASICON.* Solid State Ionics, 1987. **24**(1): p. 21-28.
188. Guin, M., F. Tietz, and O. Guillon, *New promising NASICON material as solid electrolyte for sodium-ion batteries: Correlation between composition, crystal structure and ionic conductivity of* $Na_{3+x}Sc_2Si_xP_{3-x}O_{12}$. Solid State Ionics, 2016. **293**: p. 18-26.
189. Guin, M., *Chemical and physical properties of sodium ionic conductors for solid-state batteries*, in *Der Fakultät für Georessourcen und Materialtechnik*. 2016, Rheinisch - Westfälischen Technischen Hochschule (RWTH) Aachen: Jülich.
190. Mazaheri, M., A. Simchi, and F. Golestani-Fard, *Densification and grain growth of nanocrystalline 3Y-TZP during two-step sintering.* Journal of the European Ceramic Society, 2008. **28**(15): p. 2933-2939.
191. Chen, I.W. and X.H. Wang, *Sintering dense nanocrystalline ceramics without final-stage grain growth.* Nature, 2000. **404**(6774): p. 168-171.
192. Feng, P., M. Niu, C. Gao, S. Peng, and C. Shuai, *A novel two-step sintering for nano-hydroxyapatite scaffolds for bone tissue engineering.* 2014. **4**: p. 5599.
193. Lee, M.J., H.J. Jung, H.J. Eom, S. Maskey, H.K. Kim, and C.U. Ro, *Hygroscopic behavior of individual* $NaNO_3$ *particles.* Atmos. Chem. Phys. Discuss., 2011. **2011**: p. 23203-23229.
194. Park, H., K. Jung, M. Nezafati, C.-S. Kim, and B. Kang, *Sodium Ion Diffusion in Nasicon (*$Na_3Zr_2Si_2PO_{12}$*) Solid Electrolytes: Effects of Excess Sodium.* ACS Applied Materials & Interfaces, 2016. **8**(41): p. 27814-27824.
195. E. T. Turkdogan, W.R.M., *Phase Equilibrium Investigation of the* Na_2O-P_2O_5-SiO_2 *Ternary System.* Journal of Iron Steel Institute, London, 1952. **172**: p. 1-15.
196. Kang, H.-B. and N.-H. Cho, *Phase formation, sintering behavior, and electrical characteristics of NASICON compounds.* Journal of Materials Science, 1999. **34**(20): p. 5005-5013.
197. Kuriakose, A.K., T.A. Wheat, A. Ahmad, and J. Dirocco, *Synthesis, Sintering, and Microstructure of Nasicons.* Journal of the American Ceramic Society, 1984. **67**(3): p. 179-183.
198. Lee, S.M., S.T. Lee, D.H. Lee, S.H. Lee, S.S. Han, and S.K. Lim, *Effect of particle size on the density and ionic conductivity of* $Na_3Zr_2Si_2PO_{12}$ *NASICON.* Journal of Ceramic Processing Research, 2015. **16**(1): p. 49-53.
199. Fuentes, R.O., F.M.B. Marques, and J.I. Franco, *Synthesis and properties of nasicon prepared from different zirconia-based precursors.* Boletín de la Sociedad Española de Cerámica y Vidrio 1999. **38**(6): p. 631.
200. Kreuer, K.-D., H. Kohler, and J. Maier, *Sodium Ion Conductors With Nasicon Framework Structure*, in *High Conductivity Solid Ionic Conductors*. 2013, World Scientific. p. 242-279.
201. K.D. Kreuer, H.K., J. Maier, *High Conductivity Ionic Conductors: Recent Trends and Application*. ed. T ed. World Scientific Publishing Co. 1989. 242-279.
202. Becker, P.C., T. Hayhurst, G. Shalimoff, J.G. Conway, N. Edelstein, L.A. Boatner, and M.M. Abraham, *Crystal field analysis of* Tm^{3+} *and* Yb^{3+} *in* YPO_4 *and* $LuPO_4$*.* The Journal of Chemical Physics, 1984. **81**(7): p. 2872-2878.
203. Graetsch, H.A., *Thermal expansion and thermally induced variations of the crystal structure of* $AlPO_4$ *low cristobalite.* Neues Jahrbuch für Mineralogie - Monatshefte, 2003. **2003**(7): p. 289-301.
204. Zimina, G.V., I.N. Smirnova, S.I. Kudryashova, F.M. Spiridonov, and I.F. Poletaev, *X-Ray-Diffraction Study Of The* Na_3PO_4-YPO_4 *System.* Zhurnal Neorganicheskoi Khimii, 1990. **35**(8): p. 2134-2136.

205. Zimina, G.V., I.N. Smironova, S.I. Kudryashova, F.M. Spiridonov, and I.F. Poletaev, *An X-ray diffraction study of the Na_3PO_4-YPO_4 system.* Russian Journal of Inorganic Chemistry, 1990. **35**(8): p. 1216-1218.

206. Milligan, W.O., D.F. Mullica, G.W. Beall, and L.A. Boatner, *Structural investigations of YPO_4, $ScPO_4$, and $LuPO_4$.* Inorganica Chimica Acta, 1982. **60**: p. 39-43.

207. Kanzaki, M., X. Xue, S. Reibstein, E. Berryman, and S. Namgung, *Structures of two new high-pressure forms of $AlPO_4$ by X-ray powder diffraction and NMR spectroscopy.* Acta Crystallogr B, 2011. **67**(Pt 1): p. 30-40.

208. Srikanth, V., E.C. Subbarao, D.K. Agrawal, C.-Y. Huang, and R. Roy, *Thermal Expansion Anisotropy and Acoustic Emission of $NaZr_2P_3O_{12}$ Family Ceramics.* Journal of the American Ceramic Society, 1991. **74**(2): p. 365-368.

209. Yamai, I. and T. Ota, *Grain Size-Microcracking Relation for $NaZr_2(PO_4)_3$ Family Ceramics.* Journal of the American Ceramic Society, 1993. **76**(2): p. 487-491.

210. Pet'kov, V.I., E.A. Asabina, and I.A. Shchelokov, *Thermal expansion of NASICON materials.* Inorganic Materials, 2013. **49**(5): p. 502-506.

211. Woodcock, D.A., P. Lightfoot, and C. Ritter, *Mechanism of low thermal expansion in the cation-ordered Nasicon structure.* Chemical Communications, 1998(1): p. 107-108.

212. Smirnova, O.A., R.O. Fuentes, F. Figueiredo, V.V. Kharton, and F.M.B. Marques, *Stability and thermal expansion of Na^+-conducting ceramics.* Journal of Electroceramics, 2003. **11**(3): p. 179-189.

213. Oota, T. and I. Yamai, *Thermal Expansion Behavior of $NaZr_2(PO_4)_3$Type Compounds.* Journal of the American Ceramic Society, 1986. **69**(1): p. 1-6.

214. Kaus, M., M. Guin, M. Yavuz, M. Knapp, F. Tietz, O. Guillon, H. Ehrenberg, and S. Indris, *Fast Na^+ Ion Conduction in NASICON-Type $Na_{3.4}Sc_2(SiO_4)_{0.4}(PO_4)_{2.6}$ Observed by 23Na NMR Relaxometry.* The Journal of Physical Chemistry C, 2017. **121**(3): p. 1449-1454.

215. Huang, C.-Y., D.K. Agrawal, and H.A. McKinstry, *Thermal expansion behaviour of $M'Ti_2P_3O_{12}$ (M'=Li, Na, K, Cs) and $M''Ti_4P_6O_{24}$ (M''=Mg, Ca, Sr, Ba) compounds.* Journal of Materials Science, 1995. **30**(13): p. 3509-3514.

216. Lenain, G.E., H.A. McKinstry, S.Y. Limaye, and A. Woodward, *Low thermal expansion of alkali-zirconium phosphates.* Materials Research Bulletin, 1984. **19**(11): p. 1451-1456.

217. A. Woodcock, D. and P. Lightfoot, *Comparison of the structural behaviour of the low thermal expansion NZP phases $MTi_2(PO4)_3$ (M = Li, Na, K).* Journal of Materials Chemistry, 1999. **9**(11): p. 2907-2911.

218. Srikanth, V., E.C. Subbarao, D.K. Agrawal, C.-Y. Huang, R. Roy, and G.V. Rao, *Thermal Expansion Anisotropy and Acoustic Emission of $NaZr_2P_3O_{12}$ Family Ceramics.* Journal of the American Ceramic Society, 1991. **74**(2): p. 365-368.

219. Colomban, P. and E. Mouchon, *Phase transition in, thermal history and expansion of NASICON, solid solution and lithium derivative ceramics and of SiC (mullite) fibers-NASICON composites.* Solid state ionics, 1994. **73**(3-4): p. 209-220.

220. Boilot, J.P., G. Collin, and P. Colomban, *Crystal-structure of the true nasicon - $Na_3Zr_2Si_2PO_{12}$.* Materials Research Bulletin, 1987. **22**(5): p. 669-676.

221. Tran Qui, D., J.J. Capponi, J.C. Joubert, and R.D. Shannon, *Crystal structure and ionic conductivity in $Na_4Zr_2Si_3O_{12}$.* Journal of Solid State Chemistry, 1981. **39**(2): p. 219-229.

222. Baur, W.H., J.R. Dygas, D.H. Whitmore, and J. Faber, *Neutron Powder Diffraction Study and Ionic-Conductivity Of $Na_2Zr2SiP_2O_{12}$ and $Na_3ZrSi_2PO_{12}$.* Solid State Ionics, 1986. **18-9**: p. 935-943.

223. Winand, J.M., A. Rulmont, and P. Tarte, *Ionic-conductivity of the* $Na_{1+X}M_{-X}^{(111)}Zr_{2-X}(PO_4)_3$ *systems (M = AL, GA, CR, FE, SC, IN, Y, YB).* Journal of Materials Science, 1990. **25**(9): p. 4008-4013.
224. Q. Ma, S. Naqash, F.Tietz, and O.Guillon, *High-conductivity of substituted* $Na_3Zr_2(SiO_4)_2(PO_4)$ *as the solid-state electrolyte materials for Na-batteries and method for their production*. (2015), German patent application: 102015013155.9.
225. Noguchi, Y., E. Kobayashi, L.S. Plashnitsa, S. Okada, and J.-i. Yamaki, *Fabrication and performances of all solid-state symmetric sodium battery based on NASICON-related compounds.* Electrochimica Acta, 2013. **101**: p. 59-65.
226. Traversa, E., L. Montanaro, H. Aono, and Y. Sadaoka, *Synthesis of NASICON with new compositions for electrochemical carbon dioxide sensors.* Journal of Electroceramics, 2000. **5**(3): p. 261-272.
227. Zhou, M. and A. Ahmad, *Synthesis, processing and characterization of nasicon solid electrolytes for* CO_2 *sensing applications.* Sensors and Actuators, B: Chemical, 2007. **122**(2): p. 419-426.
228. Fabry, P., C. Montero-Ocampo, and M. Armand, *Polymer electrolyte as internal ionic bridge for ion solid-state sensors.* Sensors and Actuators, 1988. **15**(1): p. 1-9.
229. Leonhard, V., H. Erdmann, and M. Ilgenstein, *NASICON electrode for detecting sodium ions.* Sensors and Actuators: B. Chemical, 1994. **19**(1-3): p. 329-332.
230. Tietz, F., *Phase relations of NASICON materials in the quaternary phase diagram.* AIMS Material Science, 2017. **4**(6): p. 1305-1318.
231. Traversa, E., L. Montanaro, H. Aono, and Y. Sadaoka, *Synthesis of NASICON with New Compositions for Electrochemical Carbon Dioxide Sensors*.* Journal of Electroceramics, 2000. **5**(3): p. 261-272.
232. Noi, K., K. Suzuki, N. Tanibata, A. Hayashi, and M. Tatsumisago, *Liquid-phase sintering of highly Na+ ion conducting Na3Zr2Si2PO12 ceramics using Na3BO3 additive.* Journal of the American Ceramic Society, 2018. **101**(3): p. 1255-1265.
233. Rousselot, C., E. El Rhess, J.P. Malugani, R. Mercier, M.F. Mercier, and A. Kishioka, *Correlations between structure and conductivity in* $NaPO_3$*-*TiO_2 *glasses.* Solid State Ionics, 1992. **58**(1): p. 71-76.
234. Langar, A., N. Sdiri, H. Elhouichet, and M. Ferid, *Conductivity and dielectric behavior of* $NaPO_3$*–ZnO–*V_2O_5 *glasses.* Journal of Alloys and Compounds, 2014. **590**: p. 380-387.
235. Sokolov, I.A., I.V. Murin, V.E. Kriyt, and A.A. Pronkin, *Structure and electric properties of* Na_2SO_4*-*$NaPO_3$ *glasses.* Russian Journal of Electrochemistry, 2011. **47**(4): p. 410-415.
236. Sokolov, I.A., I.V. Murin, V.E. Kriyt, and A.A. Pronkin, *Structure and electrical conductivity of glasses in the* Na_2O*-*Na_2SO_4*-*P_2O_5 *system.* Glass Physics and Chemistry, 2011. **37**(4): p. 351.
237. Susman, S., C.J. Delbecq, J.A. McMillan, and M.F. Roche, *NASIGLAS: A new vitreous electrolyte.* Solid State Ionics, 1983. **9-10**: p. 667-673.
238. Braga, M.H., J.A. Ferreira, A.J. Murchison, and J.B. Goodenough, *Electric Dipoles and Ionic Conductivity in a Na+ Glass Electrolyte.* Journal of The Electrochemical Society, 2017. **164**(2): p. A207-A213.
239. Milne, S.J., J.A. Gard, and A.R. West, *Synthesis of* $Na_5ZrP_3O_{12}$ *and unit cell data.* Journal of Materials Science Letters, 1983. **2**(11): p. 680-680.
240. McAdam, A., Jost, K. H. & Beagley, B., *Refinement of the structure of sodium Kurrol salt* $(NaPO_3)_x$*, type A.* Acta Crystallographica Section B, 1968. **24**: p. 1621-1622.
241. Leung, K.Y.C., C., *The structure of* $Na_4P_2O_7$ *at 295 K.* Canadian Journal of Chemistry, 1990. **50**: p. p2519-p2526.

242. Yuvaraj, S., L. Fan-Yuan, C. Tsong-Huei, and Y. Chuin-Tih, *Thermal Decomposition of Metal Nitrates in Air and Hydrogen Environments.* The Journal of Physical Chemistry B, 2003. **107**(4): p. 1044-1047.
243. Kreuer, K.-D., *Proton Conductivity: Materials and Applications.* Chemistry of Materials, 1996. **8**(3): p. 610-641.
244. Horike, S., D. Umeyama, and S. Kitagawa, *Ion Conductivity and Transport by Porous Coordination Polymers and Metal–Organic Frameworks.* Accounts of Chemical Research, 2013. **46**(11): p. 2376-2384.
245. Yaroslavtsev, A.B., *Solid electrolytes: main prospects of research and development.* Russian Chemical Reviews, 2016. **85**(11): p. 1255-1276.
246. Atsushi, I., O. Takuya, K. Eiji, K. Ayuko, and O. Shigeto, *A Single-Phase, All-Solid-State Sodium Battery Using* $Na_{3-x}V_{2-x}Zr_x(PO_4)_3$ *as the Cathode, Anode, and Electrolyte.* Advanced Materials Interfaces, 2017. **4**(5): p. 1600942.
247. Song, W., X. Ji, C. Pan, Y. Zhu, Q. Chen, and C.E. Banks, *A* $Na_3V_2(PO_4)_3$ *cathode material for use in hybrid lithium ion batteries.* Physical Chemistry Chemical Physics, 2013. **15**(34): p. 14357-14363.

List of Tables

List of Figures

Annexes 1

The microstructure of $Na_{1+x}Zr_xSi_xPO_{(1+x+4x+4x+5)/2}$, when $x = 0.4$, 0.8, 1.2, 1.6 and 2.0 sintered at $T_{20\ \%}$ at three different magnifications. In case of $x = 0.4$, the sample was unstable against polishing media therefore, higher resolution image is not shown. Each horizontal line represents images for one composition.

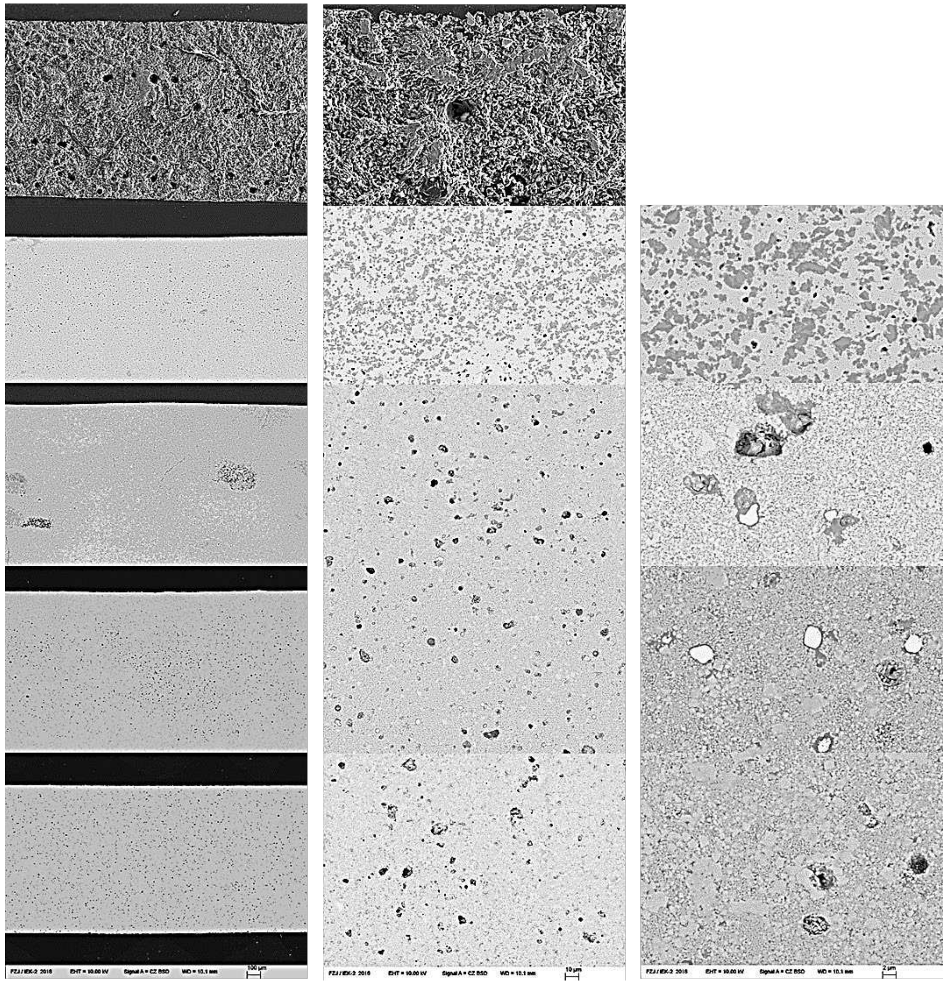

Acknowledgements

This PhD. thesis owes gratitude towards several people without whom it would not have been possible to complete this on time. Their continuous support and help has indeed contributed over the past three years.

I would like to thank Prof. Dr. Olivier Guillon, the Director of IEK-1, for agreeing to supervise me. During the last three years he was constantly available for fruitful discussions and productive meetings. His prompt feedback on my submissions has indeed made it possible to complete this work within time.

I would also like to extend my biggest gratitude to Dr. Frank Tietz, the group leader of Functional Materials at IEK-1, for accepting my application for doctoral research 2014 and giving me the opportunity to work under his esteemed supervision in one of world's state-of-the-art institute. Frank also gave an uninterrupted support throughout my work through in-depth discussions about new ideas, openness to new pathways and out of the box thinking for overcoming problems. Besides, his friendliness and laughter has contributed massively in motivating me to implement new ideas. I got inspired and admire him of his friendly yet deeply scientific attitude.

I also would like to thank Dr. Qianli Ma (Ma) for his help in various technical aspects. Ma remained open to solve whatever I threw at him. His scientific and technical knowhow is exceptional and he played an important role in various scientific contributions in this thesis.

I would like to thank also Dr. Enkhtsetseg Dashjav (Enkhe) for her friendly and always-pleasant attitude. Enkhe taught me Rietveld analysis using the computer software in lengthy hours and did not hesitate to repeat everything again when I asked. Her support in both professional and personal matters has greatly helped me to focus on my work.

I also would like to thank Dr. Marie Guin who was the only person working with sodium batteries at IEK-1 when I started. She helped me get started. Thank you again for getting me started and off course all the fun talks that kept me motivated in boring hours.

I would also like to thank my entire group members, Volker Bader for performing hundreds of thermal treatments throughout my work, and times to come, Marie-Theres Gerhards and Sylke Pristat for the thermal analysis and their friendliness and support, Michaela Andreas and Jochen Ripphahn for their technical support.

I would also like to thank Dr. Doris Sebold for performing doing the SEM images, her expertise in the field of SEM is exceptional and she always remained open to my requests and always gave me results quickly.

I worked in close collaboration with colleagues from the battery group at IEK-1:, Prof. Dina Fattakhova, Sven Uhlenbruck, Martin Finsterbusch, Sandra Lobe, Chi-Long Tsai, Anna Windmüller, Frank Vondalen and Christian Dellen. I learnt a lot from each of them.

So many other people have contributed to this work, thank you to Mark Kappertz for helping on the preparation of SEM specimen, and Doris Sebold for making the SEM pictures. Thank you to Egbert Wessel and Daniel Grüner for doing SEM and EDX analysis on my samples. Thank you also to the colleagues from ZEA-3, and especially Volker Nischwitz for the ICP-OES.

I would also like to thank my wife Saba Mansha, who stayed affirmed in tough and rough times and gave me the confidence and support I needed. Later, she gifted me with a cute daughter Anaya Naqash two days after my birthday. Anaya kept smiling at me no matter what the situation was. Big thanks to both of them. I also would like to thank my parents, even though they are 8000 km apart but they kept helping me in whatever way they possibly could.

During the last three years, I believe, I could not have been as productive had I not participated in a rather vital part of my life: Cricket. I played for two clubs during this time; first in Köln CC Ligamannschaft and then in Blue Stars Cricket Club e. V Bonn. Both these clubs helped me in getting selected for the state team North Rhine-Westphalia and finally in the German National team. Cricket in Germany has indeed provided me enough opportunity to travel and make new friends. Cricket in Germany is on a rise, I won’t be surprised to see Germany playing the cricket world cup within next 10 years.

Band / Volume 437
Characterization of High Temperature Polymer Electrolyte Fuel Cells
Y. Rahim (2018), iii, 162 pp
ISBN: 978-3-95806-359-4

Band / Volume 438
Lattice Boltzmann Simulation in Components of Polymer Electrolyte Fuel Cell
J. Yu (2018), ii, 173 pp
ISBN: 978-3-95806-360-0

Band / Volume 439
Quantitative Luminescence Imaging of Solar Cells
V. Huhn (2018), 155 pp
ISBN: 978-3-95806-363-1

Band / Volume 440
Characterization of Phosphoric Acid Doped Polybenzimidazole Membranes
Y. Lin (2018), II, IV, 140 pp
ISBN: 978-3-95806-364-8

Band / Volume 441
Degradation Study of SOC Stacks with Impedance Spectroscopy
Y. Yan (2018), 135 pp
ISBN: 978-3-95806-367-9

Band / Volume 442
Future Grid Load of the Residential Building Sector
L. Kotzur (2018), xxi, 213 pp
ISBN: 978-3-95806-370-9

Band / Volume 443
Yttriumoxid-Dünnschichten als Tritium-Permeationsbarriere
J. Engels (2018), 252 pp
ISBN: 978-3-95806-371-6

Band / Volume 444
Inverse conditioning of a high resolution integrated terrestrial model at the hillslope scale: the role of input data quality and model structural errors
S. Gebler (2018), xxii, 160 pp
ISBN: 978-3-95806-372-3

Band / Volume 445
Cathode Stability and Processing in Inert Substrate-Supported Solid Oxide Fuel Cells
E. Matte (2018), viii, 178 pp
ISBN: 978-3-95806-373-0

Band / Volume 446
Aging and Degradation Behavior of Electrode Materials in Solid Oxide Fuel Cells (SOFCs)
X. Yin (2018), x, 103 pp
ISBN: 978-3-95806-374-7

Band / Volume 447
TRENDS 2017
Transition to Renewable Energy Devices and Systems
D. Stolten, R. Peters (Eds.) (2018), 206 pp
ISBN: 978-3-95806-376-1

Band / Volume 448
3D simulation of impurity transport in a fusion edge plasma using a massively parallel Monte-Carlo code
J. Romazanov (2018), xvi, 149 pp
ISBN: 978-3-95806-377-8

Band / Volume 449
Projektbericht Adelheid – aus dem Labor heraus in die Lüfte
D. Stolten, R. Peters (Eds.) (2018), xxi, 321 pp
ISBN: 978-3-95806-378-5

Band / Volume 450
Microstructure and Thermomechanical Properties of $SrTi_{1-x}Fe_xO_{3-\delta}$ Oxygen Transport Membranes and Supports
R. Oliveira Silva (2019), vi, 148 pp
ISBN: 978-3-95806-381-5

Band / Volume 451
Sodium Ion Conducting Ceramics for Sodium Ion Batteries
S. Naqash (2019), vii, 134 pp
ISBN: 978-3-95806-382-2

Weitere ***Schriften des Verlags im Forschungszentrum Jülich*** unter
http://wwwzb1.fz-juelich.de/verlagextern1/index.asp

Energie & Umwelt / Energy & Environment
Band / Volume 451
ISBN 978-3-95806-382-2

Mitglied der Helmholtz-Gemeinschaft

JÜLICH
Forschungszentrum